UC Berkeley
Research Reports

Title

Development and Implementation of a Vehicle-Centered Fault Diagnostic and Management System for the Extended PATH-AHS Architecture: Part I

Permalink

https://escholarship.org/uc/item/6nh6r02x

Authors

Yi, Jingang
Suryanarayanan, Shashikanth
Howell, Adam
et al.

Publication Date

2002-11-01

Development and Implementation of a Vehicle-Centered Fault Diagnostic and Management System for the Extended PATH-AHS Architecture: Part I

**Jingang Yi, Shashikanth Suryanarayanan,
Adam Howell, Roberto Horowitz, Masayoshi Tomizuka,
Karl Hedrick, Luis Alvarez**
University of California, Berkeley

The contents of this report reflect the views of the authors who are responsible for the facts and the accuracy of the data presented herein. The contents do not necessarily reflect the official views or policies of the State of California. This report does not constitute a standard, specification, or regulation.

Final Report for MOU 373

November 2002

CALIFORNIA PARTNERS FOR ADVANCED TRANSIT AND HIGHWAYS

Development and Implementation of a Vehicle-Centered Fault Diagnostic and Management System for the Extended PATH-AHS Architecture: Part I

Jingang Yi, Shashikanth Suryanarayanan, Adam Howell,
Roberto Horowitz, Masayoshi Tomizuka, Karl Hedrick

Department of Mechanical Engineering
University of California at Berkeley, USA

Luis Alvarez

Instituto de Ingeniería
Universidad Nacional Autónoma de México, México

August 6, 2002

ABSTRACT

The purpose of this project is to extend and integrate existing results on fault diagnostics and fault management for passenger vehicles used in automated highway systems (AHS). These results have been combined to form a fault diagnostic and management system for the longitudinal and lateral control systems of the automated vehicles which has a hierarchical framework that complements the established PATH control system. Furthermore, the fault diagnostic module effectively monitors the sensors and actuators required for longitudinal and lateral control, while the fault handling module corrects for any detected faults via controller reconfiguration and degraded modes of operation. "Soft" faults such as tire/road conditions variations have also been investigated in this project. Based on a dynamic friction tire/road model, an emergency braking control law has been developed. Simulation and limited experimental results are provided to validate the design and development.

KEYWORDS

Fault diagnostics, fault handling, automated highway systems (AHS), fault observers/filters, LuGre friction model, tire/road friction estimation

ACKNOWLEDGMENT

Executive Summary

Since the NAHSC [1] demonstration in 1997, PATH and Caltrans have been focusing increasingly on Automated Highway System (AHS) deployment related issues such as safety and reliability. Fault accommodation and handling is a key safety related issue. This report presents an integrated approach to the design of a vehicle centered fault tolerant system for the PATH AHS architecture. The bulk of the research presented in this report was done as part of PATH-Caltrans MOU 373.

The research documented in this report primarily focuses on fault management in the regulation layer of the PATH AHS architecture. The regulation layer consists of the lateral and longitudinal control laws that interact directly with the sensors and actuators on-board the PATH vehicles. In addition, this report presents the coordination layer fault management issue of emergency braking control. Fault management in the longitudinal control system was addressed in a mostly ad-hoc manner during preparations for Demo 97. Basic fault detection and diagnosis for the lateral control system components was addressed prior to Demo 97. The research effort documented in this report was aimed at developing on these starts made towards the development of a comprehensive failure management system for the PATH AHS.

Since the lateral and longitudinal dynamics of the vehicles are vastly different in their behavior, different approaches have been adopted for fault management systems of each of these subsystems. Fault tolerance in the lateral control subsystem is realized mainly through the use of fault tolerant lateral control laws (refer Chapter 3) whereas a "classical" approach for fault tolerant control design was used for the longitudinal control system (refer Chapter 4). "Soft" faults detection and handling, particularly the tire/road interactions and emergency braking maneuvers, have also been investigated (refer Chapter 5).

One of the major contributions of this research is the successful design and implementation of a comprehensive failure management system for the regulation layer of the PATH AHS architecture. In this report, fault tolerant lateral control laws, failure detection filters for the lateral and longitudinal control subsystems have been developed and tested in the simulation and also in limited experiments both at low and high speeds on the Buick LeSabre vehicles at PATH. In the project Task Order 4207, we will demonstrate extensively experimental verification of these control laws. These failure **management** modules safeguard the vehicles against certain failures (chosen based on experience and physical construction of the vehicle) that may occur during operation. The design methodologies and results of this effort in conjunction with the results of MOU 384/TO 4204 (Vehicle Lateral Control under Fault in the Front/Rear Sensors) are aimed for use in the development of fault tolerant lateral and longitudinal control systems (TO 4205, TO 4206) for heavy vehicles to be used in Demo 2003.

Another major contribution of this research is the introducing a dynamic friction model to the

---

[1]National Highway Systems Consortium.

tire/road interactions and then building connections between friction model parameters and physical factors. We explore the use of a *LuGre* dynamic friction model (Canudas de Wit et al., 1995) of tire/road interactions. An emergency braking controller is designed using the wheel angular velocity and longitudinal acceleration information. Analytically it is shown that the observer and the adaptive controller are asymptotically stable. It is shown that underestimation of maximum friction coefficient and slip can be achieved. This is a very desirable feature for the deployment of AHS or ITS, where it is of primary importance to ensure safe operation. For the purpose of safety, the information provided by the on-line tire/road identification scheme in this project may be very useful for on-line safe spacing calculations in vehicles running under AHS or intelligent cruise control algorithms. The information can also be used by the roadside infrastructure to adjust on-ramp metering control.

Contents

List of Figures

List of Tables

Chapter 1

Introduction

Over the last ten years, PATH's Advanced Vehicle Control System effort has made impressive strides in the modeling, control design and implementation of several vehicle control laws. Since the 1997 NAHSC [1] demonstration on the I-15 lanes in San Diego, PATH's research focus has shifted towards deployment related issues encountered in Automated Highway Systems (AHS) development such as safety and reliability.

To satisfy requirements of safety, the AHS should be designed such that the automated vehicles function safely under nominal operating conditions as well as under "abnormal"or faulty conditions that arise during highway operation. The nominal operating environment assumes the faultless operation of the system components and benign environmental conditions. The abnormal operating conditions are caused by faults. For the purposes of this report, a fault is defined as: *an abnormal that affects system performance adversely*. We classify the faults as Lygeros et al. (2000) and Godbole et al. (2000):

1. Hard Faults: these include failures or faults in one of the control system components, such as mechanical failures in the vehicles, failures in sensing, communication, control and actuation both on the vehicle and the roadside.

2. Soft Faults: these include adverse environmental conditions, such as rain, fog, snow, etc. and the loss of performance due to gradual wear of AHS components.

In the past, AHS design has addressed accommodating these two classes of operating conditions either by switching between two general modes of operation: normal mode, which gives optimal performance under nominal conditions, and several degraded modes, which ensure safety and attempt to minimize performance degradation under abnormal conditions.

Several prior and on-going research efforts (Demo 97 preparations, MOU 384, MOUs 288/312, etc.) at PATH have dedicated a great deal of effort towards the design of a robust controllers for both modes of operation. Normal mode control laws at the regulation, coordination and link layer have been developed and tested in simulations and experiments. Fault detection algorithms for the onboard sensor and actuator critical to automated control have been developed and tested in simulations and experiments (Garg, 1995; Chung et al., 1996; Chung et al., 1997; Patwardhan, 1994; Agogino et al., 1997; Rajamani et al., 1997; Rajamani et al., 2001; Yi et al., 2001). At the same time, fault handling schemes using new maneuvers and control laws have been designed for degraded modes of

---

[1]National Highway System Consortium.

operation to ensure that the safety of the AHS is maintained and the performance loss is minimized in abnormal situations (Lygeros et al., 2000; Godbole et al., 2000; Chen et al., 1997; Yi et al., 2001). In addition, these fault handling schemes have been successfully tested in the SmartPATH and SmartAHS simulation program (Carbaugh et al., 1997; Yi et al., 2001).

The goal of this project is to extend and improve these developments in the areas of fault diagnostics and fault handling with the existing control hierarchy (Varaiya, 1993) to produce a complete fault tolerant AHS control system that can be implemented on the vehicles and the roadway. The project concentrates on the design of a fault tolerant AHS control system that can detect and handle both hard and soft faults in the lateral and longitudinal control systems. However, acts of nature, such as earthquakes, floods, etc. and obstacles on the road are not considered in order to limit the scope of the project. In other words, the project intends to develop and implement subsystems that fit into the the overall structure of a fault tolerant AHS control system as shown schematically in Fig. 1.1. The project primarily focuses on development related to the regulation layer namely the lateral and longitudinal control subsystems.
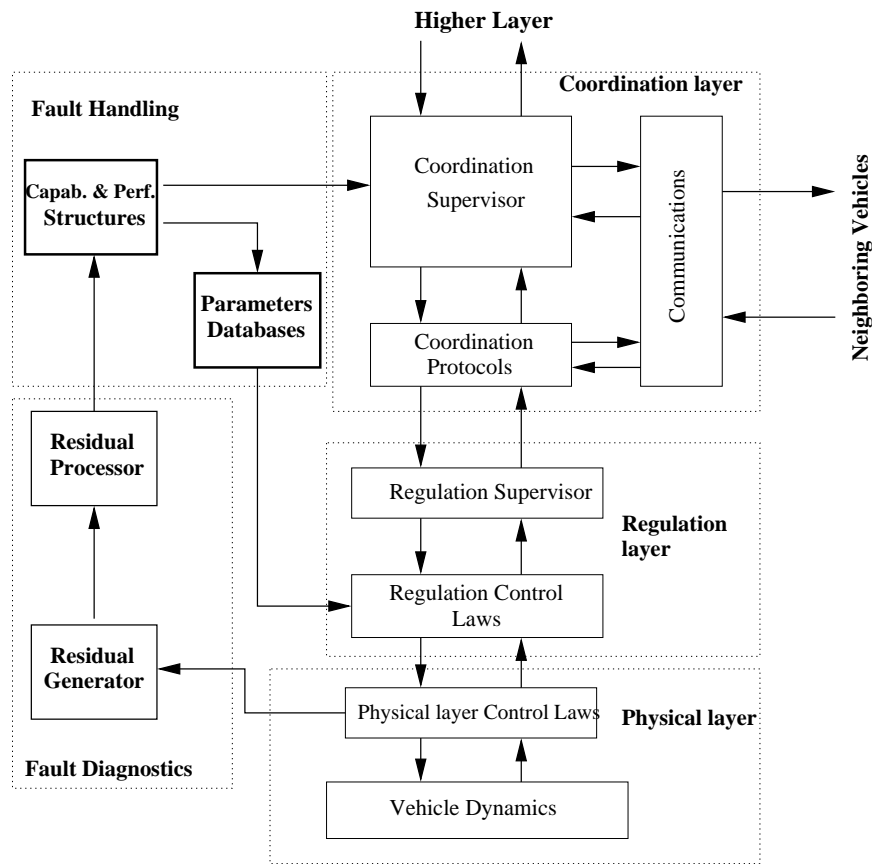
Figure 1.1: Extended hierarchical fault tolerant AHS controller

1.1   Fault Tolerant System Design

In this section, we propose the overarching design framework that has governed our approach towards the development of a comprehensive failure management and handling system for the regula-
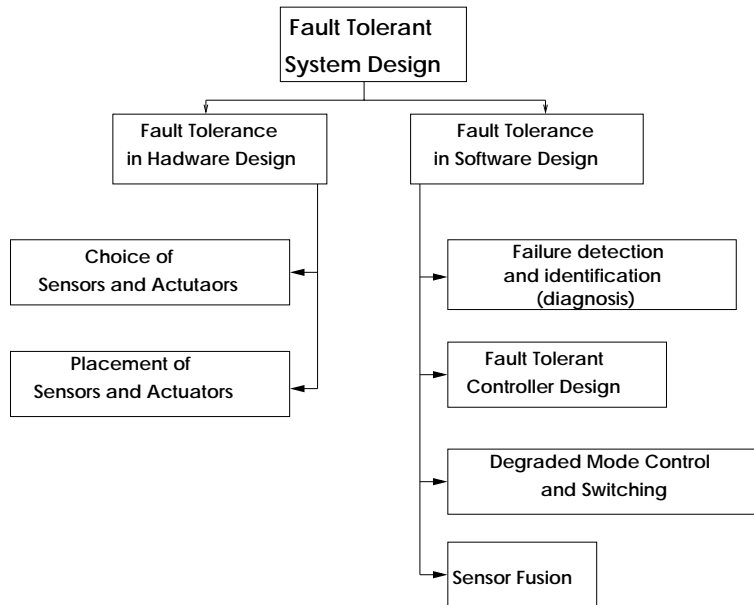
Figure 1.2: Fault Tolerant Design Framework

tion layer of the PATH AHS. In doing so, we shall also highlight this research effort is linked to past and on-going research at PATH.

Fig. 1.2 depicts the fault tolerant system design framework. The fault tolerant design framework attempts to incorporate fault tolerance **apriori** into system design. The framework is based on the argument that important design decisions (such as those shown in Fig. 1.2) made during the design process of an automated system have a direct bearing on the fault tolerance of the resulting automated system. Therefore, each design decision needs to be judiciously made based on, amongst other considerations, the issue of fault tolerance of the resulting system.

We now mention where relevant past/present research activity at PATH fit in into this overall design framework.

- Demo 97: Longitudinal and lateral control design, rudimentary failure detection and diagnosis issues associated with the radar

- MOU 289, MOU 313, MOU 385: Lateral control design for heavy vehicles

- MOU 292, MOU 314, MOU 372: Longitudinal control design for heavy vehicles

- MOU 288, MOU 312, **MOU 373, TO 4207**: failure detection and diagnosis systems for the longitudinal control system, fault tolerant control schemes for the lateral control system, soft fault handling: tire-road friction estimation and emergency braking control.

- MOU 383, TO 4208: Development of integrated meso/micro-scale traffic simulation software for testing fault detection and handling in AHS.

- MOU 384, TO 4204: Degraded mode control schemes for lane-keeping control under failure of the front/rear magnetometers

- TO 4205, TO 4206: Sensor placement and integration of all prior research aimed at a fault tolerant design framework for lateral and longitudinal control subsystems to be implemented on buses

- TO 4209: Testing and evaluation of robust fault detection and identification for a fault tolerant automated highway system (AHS).

1.2 Organization of Report

Chapter 2 deals with the preliminaries and background required to appreciate the research that this report documents. Chapter 3 deals with the motivation, synthesis and experimental evaluation of fault tolerant lateral controllers. Chapter 4 deals with the design and experimental evaluation of the detection and diagnosis system for the longitudinal control components. Chapter 5 deals with handling of soft faults in the coordination layer. Specifically, it deals with tire-road friction estimation and its application to emergency braking control.

For the lateral control system, a new approach to failure management (in its components) has been adopted. This deals with the design of fault **tolerant** controllers which are insensitive to certain faults that may occur during operation of the vehicles. In other words, implementation of fault tolerant controllers guarantee that even in the event of certain failures in the components of the lateral control system, the vehicle can be steered satisfactorily **without switching to degraded modes** of operation. This design methodology has been adopted for the lateral control system because of the sensitive nature of the lateral control dynamics which necessitate "quick" steering action. Chapter 3 deals with a detailed description of this methodology.

For the longitudinal control system, a classical approach to fault tolerant control design was taken because of the proven performance and robustness of the existing nominal controller. Fault tolerance of the controller is provided by the addition of the fault diagnostic system and fault management system as shown in Fig. 1.3. The fault diagnostic system monitors the condition of the vehicle via sensor measurement and command inputs, and communicates the current status to the fault management system. The fault management system uses this information, as well as the current mode of operation and other control objectives, to decide what corrective action should be taken when a fault has been declared. This framework is ideal for the longitudinal control system because it allows for modular design of each system and added fault tolerance while remaining essentially transparent to the nominal control system.

The fault diagnostic system developed in this project relies on a mathematical model of the controlled vehicle to provide analytical redundancy for the sensors and actuators used in the longitudinal control system. This model-based fault diagnostic system is composed of two main stages: the *residual generator* and the *residual processor*. The residual generator uses current knowledge about the state of the system to create a set of signals, called *residuals*, which are sensitive to the occurrence of faults. These residuals are a designer-defined set of comparisons between the various types of information known about the system, such as sensor measurements, command inputs, as well as state and output estimates based on a model of the system (Beard, 1971; Willsky, 1976). The choice of which types of information to use and the specific residuals formed depend on both the system model, as well as the type of faults to be detected. For the purposes of this project, an additive fault model is used to represent time-varying biases in the sensors and actuators (org., n.d.). Based on

4
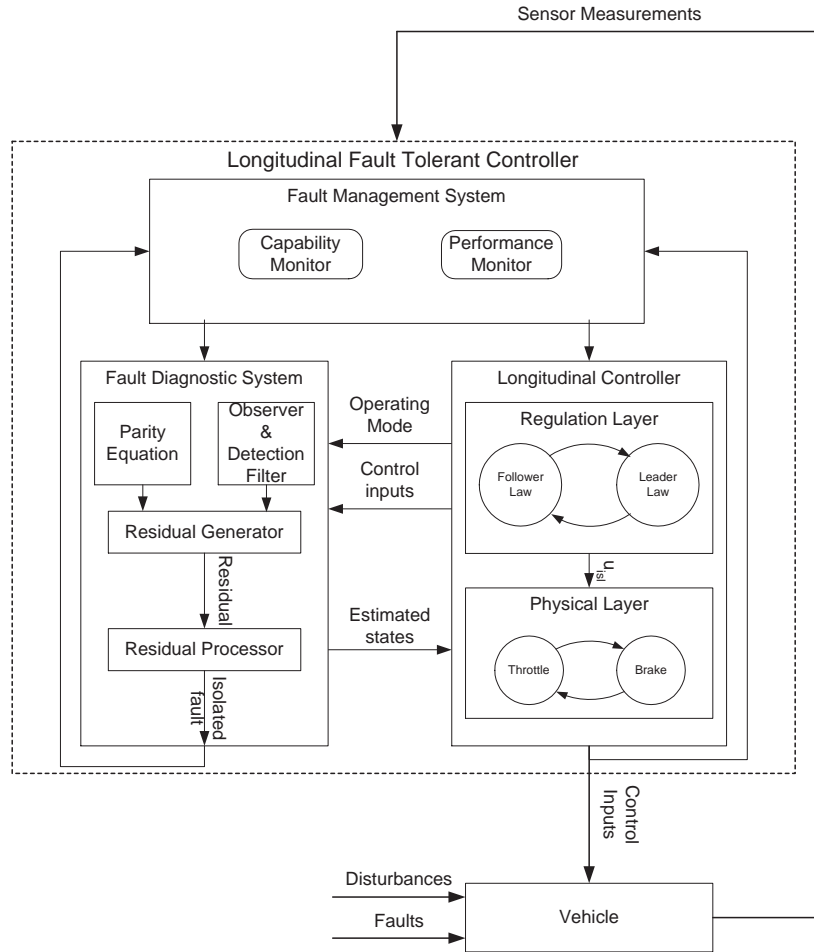
Figure 1.3: Fault Tolerant Longitudinal Control System

this fault model, the residual generator uses a combination of parity equations (Gertler, 1988) and state observers (Frank, 1990) to form the residual vector. The second stage of the diagnostic system processes the residual vector to determine when a fault has occurred and to identify the faulty component based on the vector's characteristics. This processing is generally a complex task that can incorporate a variety of disciplines including change detection (Basseville and Nikiforov, 1993), pattern recognition (Bow, 1992), and reasoning (Ross, 1995). The residual processor for this project uses least squares estimation and decision logic to detect, identify, and estimate the fault magnitude. A more detailed description of the fault diagnostic system and each of it's subsystems will be presented in Chapter 4.

In Chapter 5, tire/road interaction forces and moments are first introduced. We then review the literature on tire/road friction estimation and identification. In particular, we discuss empirical and physical models in detail. We give a description of the friction models used in this project. In this first part of this chapter, we investigate a tire/road friction estimation scheme using a LuGre dynamic friction model. This model was recently proposed and it captures dynamic properties of the friction characteristics. Compared with the pseudo-static tire/road friction model developed in MOU 312, the LuGre dynamic friction model is easy to identify and use for simulation and control purposes. we

initially assume that the vehicle longitudinal velocity is known and an adaptive emergency braking control law is designed for various tire/road conditions. We then relax this assumption with the use of an observer-based controller design that uses only wheel angular velocity information. Analytical and simulation results show that the proposed scheme can estimate the tire/road friction and achieve emergency braking near the maximum deceleration capability of the vehicle, even though the estimated velocity and relative velocity do not converge to their true values quickly. In the second part of the chapter, we enhance the design by assuming that the vehicle acceleration is measurable as well as the wheel angular velocity, in order to overcome the drawback of slow convergence of estimated vehicle velocity and relative velocity. A generalized LuGre dynamic friction model is employed with an assumption that several model parameters are unknown. An adaptation law for the tire/road friction parameters is proposed and an emergency braking control law is designed. A stability proof is presented, and quick convergence of the estimated parameters as well as the estimates of vehicle velocity and relative velocity is guaranteed by appropriate choice of observer and parameter adaptation gains.

Chapter 2

Preliminaries

This chapter will describe the existing AHS framework developed at PATH. It's purpose is to provide a detailed overview of the past research on which the fault tolerant control system is based. First, the hierarchical PATH AHS architecture will be covered in section 2.1. The mathematical modeling and controller design for the lateral and longitudinal motions of the vehicle will be then be developed in sections 2.2 and 2.3, respectively. Finally, section 2.5 will give a description of the experimental test vehicles on which the controllers have been implemented and tested.

2.1   PATH AHS Architecture

The AHS control architecture proposed in (Varaiya, 1993) consists of five hierarchical layers: the network, link, coordination, regulation and physical layers. A schematic of this hierarchy is shown in Fig. 2.1. Each layer provides a different function within the AHS according to it's relative position in the hierarchy, with the higher levels controlling traffic flows and density and the lower levels controlling platoons and individual vehicles.

   The two highest layers of the architecture are concerned with traffic density and flow within the AHS. The **network layer** controls the entire highway system and tries to maximize the throughput of the highway system, while the **link layer** monitors the traffic flow of several sections of highway and broadcasts commands to all vehicles within these sections. The link layer also attempts to maximize the traffic capacity within these sections and deals with incidents on the highways. Both network and link layers are located within a roadside system and interact with the vehicles via communication.

   The three lowest layers of the architecture are concerned with the behavior of platoons and individual vehicles within the AHS. The **coordination layer** receives the commands from the link layer and is responsible for coordinating the maneuvers of vehicles within a platoon through communications with other vehicles. The **regulation layer** converts the maneuver commands into continuous time control signals used to dictate the desired vehicle motion trajectory. Finally, the **physical layer** contains the vehicle sub-system controllers for the physical hardware of each vehicle such as the control of the brakes, throttle and steering. These lower layers of control are contained within the on-board control system of each automated vehicle.

   Within the regulation and physical layers, there is a further division into the control of the lateral and longitudinal dynamics of the vehicle. The following two sections will present an overview of the existing lateral and longitudinal control systems developed for the PATH AHS architecture.
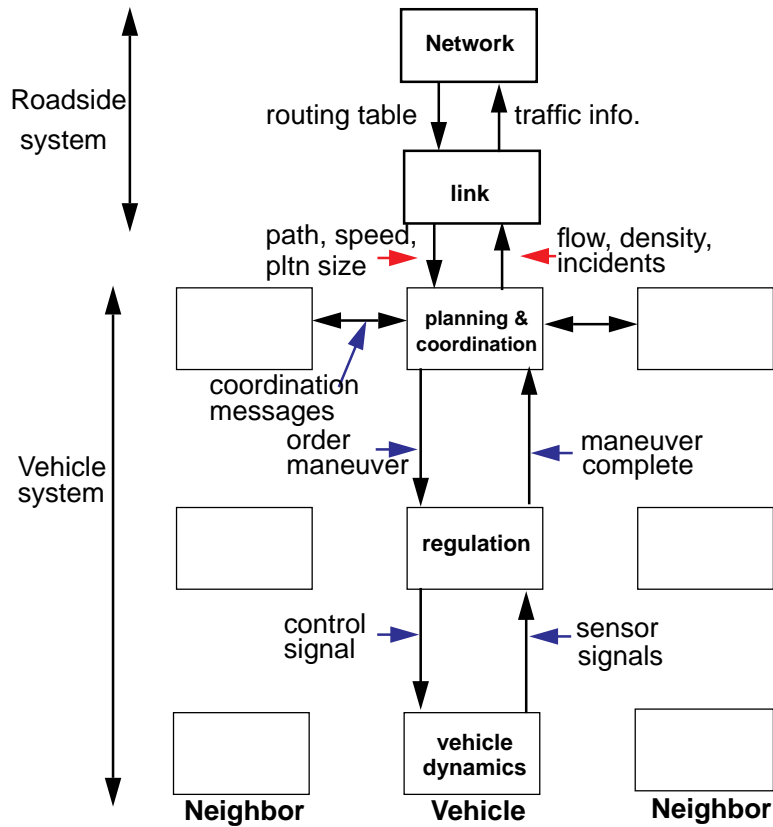
Figure 2.1: PATH AHS Architecture

2.2 Lateral Control at the Physical Layer

In this section, the lateral control system at the physical layer of PATH AHS architecture is described. Specifically, we present the salient features of the lateral dynamics exhibited by front wheel steered vehicles within the context of lane-keeping control. Fig. 2.3 tries to capture the intuition behind this problem. The vehicle can be regarded as an inertia moving forward, while the task of lane-keeping control is to ensure that this inertia follows the road centerline. This can be done by applying the appropriate lateral forces to the inertia. The problem becomes complicated because these lateral forces have to be generated through tire-road interaction (which depend primarily on the slip angle [1]).

2.2.1 Lateral Dynamics

We use the bicycle model for lane-keeping control analysis and design purposes. In deriving the bicycle model, the lateral vehicle motion is modeled as that of a two-wheeled bicycle. (Fig. 2.2 shows a pictorial representation of this reduction). The major assumptions made in deriving this model are:

- Negligible roll and pitch

---

[1]Slip angle is the angle between the orientation of the tire and direction of travel of the CG of the tire
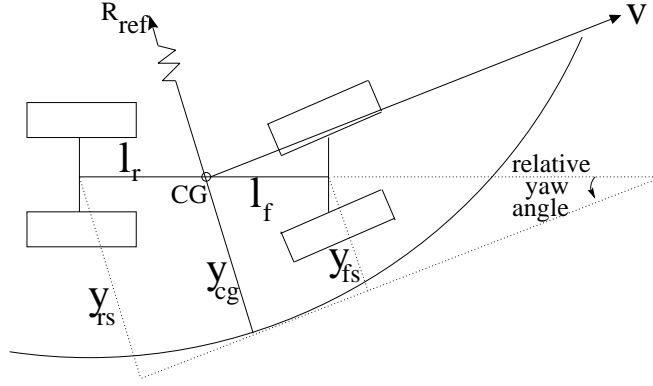
Figure 2.2: Vehicle moving along a reference path

- Small steering angles

- Small relative yaw angles (refer Fig. 2.2)

- Lateral force on tire $\propto$ slip angle

The attractions of the bicycle model are that it is simple and yet captures the most releavant lateral dynamic characteristics. We direct the reader to references (et al, 1978), (P., 1997) for a more detailed description of the bicycle model.

If the vehicle longitundinal velocity is treated as a varying parameter, the bicycle model yields linearized dynamics. The transfer function from the steering input (δ_f) to the lateral accelaration ($\ddot{y}_s$) at the location of the sensor is:

$$\ddot{y}_s = V(s)\delta_f(s) \tag{2.1}$$

where,

$$V(s) = \frac{N(s)}{D(s)}$$

$$N(s) = \mu C_f v \left[(ML_f d_s + I_z)s^2 v + \mu C_r l(v + (d_s + l_r)s)\right]$$
$$D(s) = I_z M v^2 s^2 + \mu v(I_z(C_f + C_r) +$$
$$M(C_f l_f^2 + c_r l_r^2))s + \mu M v^2(C_r l_r - C_f l_f) +$$
$$\mu^2 C_f C_r l^2$$

Table 2.1 describes the parameters used in the bicycle model and their values used for design in this paper.

In the linearized setting, the transfer function $V(s)$ captures the tire-road interaction (refer to Fig. 2.3). A system analysis of the above model is presented by Patwardhan et al, 1997 (et al, 1997). It is observed that the lateral dynamics change significantly with the longitudinal velocity and the distance of the sensor from the CG, d_s (refer Table 2.1). "In general", $V(s)$ exhibits the following properties:

1. Increased phase lag with increase in longitudinal velocity, v

Table 2.1: Parameters used in the Bicycle Model

Param.	Description	Values
M	Mass of the vehicle	1700-2100 kg
I_z	Yaw moment of inertia	≈ 2870 kg m^2
l_f	CG-front axle dist.	0.9 - 1.2 m
l_r	CG-rear axle dsit	1.5 - 1.8 m
C_f	Cor. stiff. - Front tire	≈ 70000 N/rad
C_r	Cor. stiff. - Rear tire	≈ 130000 N/rad
v	Forward vel. of vehicle	0- 35 m/s
d_s	Dist. of sensor from CG	-3 to 10 m
μ	Tire - Road Fric. Coeff	0.5-1.0

2. Increased phase lead for larger d_s

3. Poorly damped zero pairs for smaller d_s

2.2.2   Lane-keeping Controller Design

The above three properties of the lateral dynamics of vehicles govern the design of the lateral controller. It is useful to consider the lateral control system to be comprised of three principal components (Fig. 2.3) which include a double integrator, a force generation mechanism, $V(s)$, and the controller. Robust stability considerations of the closed loop require that the open loop characteristics have sufficient phase margin around the gain cross over frequency. The phase lead required to provide this phase margin around the gain crossover frequency has to be "provided" either by $V(s)$ or by the controller (The Dual-Roles Concept: See Guldner et al, 1997 (et al, 1996)). From the behaviour of $V(s)$ as explained above, it is clear that at higher longitudinal velocities and small values of d_s the controller needs to provide large phase leads to provide sufficient phase margin which is difficult to achieve in practice. Moreover, weakly damped zeros for small d_s and high longitudinal velocities discourage high gain control at high longitudinal velocities. The above two problems illustrate the inherent difficulty and non-trivial nature of vehicle lateral control design at high longitudinal velocities as those encountered on highways.

Large values of d_s are impossible to realize since it is infeasible to place the front set of magnetometers any further the front bumper of the vehicles. PATH engineers developed an ingenious way of working around this problem. They suggested a scheme such that if two independent lateral error measurements are made, then by geometrical extrapolation (under some valid assumptions) one can construct the lateral error at any location ahead of the vehicle. This second measurement is obtained from the magnetometers mounted under the rear bumper. This scheme, used in Demo'97, has proved to be immensely successful. Details of this scheme, referred to as the variable look-ahead scheme, is discussed in Guldner et al (et al, 1996). In summary, for lane-keeping control at high speeds, larger values of d_s lead to better yaw rate damping characteristics and consequently better ride comfort.
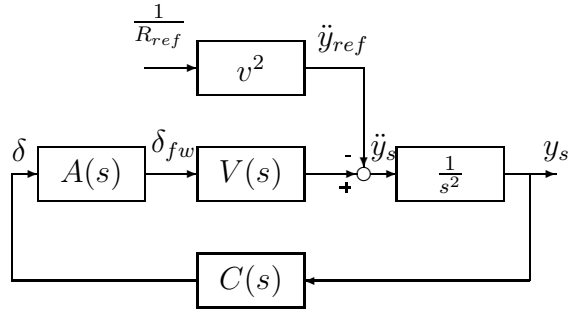
Figure 2.3: Block diagram for control model

$$
\begin{aligned}
A(s) &: \quad Actuator\ Dynamics \\
C(s) &: \quad Controller \\
\delta &: \quad Steering\ angle\ at\ the\ steering\ wheel \\
\delta_{fw} &: \quad Steering\ angle\ at\ the\ front\ wheel \\
R_{ref} &: \quad Radius\ of\ curvature\ of\ road \\
\ddot{y}_{ref} &: \quad Acceleration\ due\ to\ road\ curvature
\end{aligned}
$$

2.3   Longitudinal Control at the Physical Layer

While the lateral controller uses a linear control theory to track the roadway, the longitudinal controller at the physical layer is based on a nonlinear control technique called *sliding mode control*. While the details of this design technique are beyond the scope of this work, the interested reader is referred to (Khalil, 1996; Slotine and Li, 1991) for more information. This controller has been successfully implemented and thoroughly tested on the experimental vehicles at PATH, and thus represents the default physical layer controller which will used for the remainder of this report.

The longitudinal control at the physical layer has several distinct control tasks, so a hierarchical control architecture is used to address each of these in turn. The hierarchical controller is composed of three levels of control as shown in Fig. 2.4.

At the top level, feedback linearization is used to determine the desired engine torque required to track the desired acceleration given by the regulation layer (Swaroop et al., 1996; Gerdes, 1996). The middle level of the longitudinal controller is a switching logic which decides whether acceleration or braking is required based on the current state of the vehicle and the desired torque (Gerdes, 1996). If acceleration is required, the desired torque is subsequently passed on to the throttle controller to determine the throttle actuator command. Similarly, if deceleration is required, the desired torque is subsequently passed on to the brake controller to determine the brake actuator command (Maciuca, 1997). Both of these bottom level controllers use a sliding mode control algorithm known as *dynamic sliding surface control* (Swaroop et al., 1996) to meet the desired torque.

The remaining parts of this section will cover the vehicle model used for the controller design, the key relations describing the resulting three levels of the physical layer controller, how the desired acceleration is chosen by the regulation layer, and the sensor's and actuator's required for the given control system.
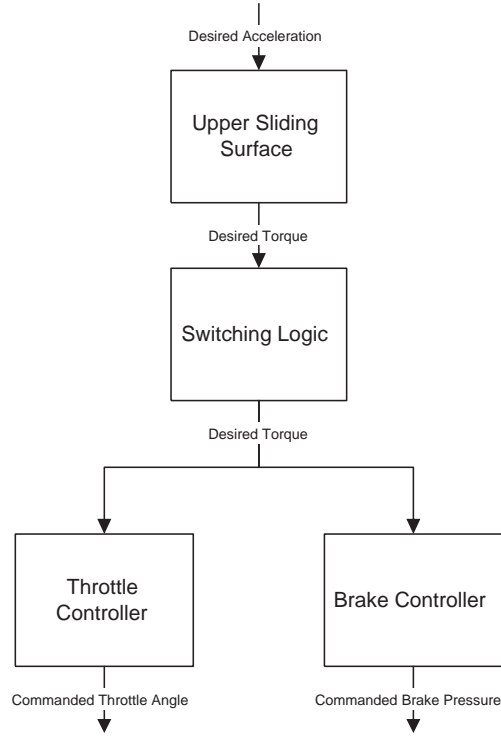
Figure 2.4: Physical layer of the longitudinal control hierarchy

2.3.1 Simplified Vehicle Model for Control

The longitudinal controller was developed using the simplified longitudinal vehicle model described in (Gerdes, 1996; Swaroop et al., 1996). The vehicle model is derived by making the following assumptions:

1. The slip between the tires and the road surface is negligible.

2. The torque converter is locked.

3. The actuator dynamics are fast compared to the vehicle dynamics.

Under these assumptions, the longitudinal velocity of the vehicle $\dot{x}$ is proportionally related to the angular velocity of the engine ω_e through the gear ratio R^* and tire radius h as follows

$$\dot{x} = R^* h \omega_e$$

The dynamics relating engine speed ω_e to the net combustion torque T_{net}, brake torque T_{br}, and aerodynamic losses can be modeled by

$$J_e \dot{\omega}_e = T_{net}(m_a, \omega_e) - c_x R^{*3} h^3 \omega_e^2 - R^*(T_{rr} + T_{br}(P_{wheel}))$$

where J_e is the effective inertia of the vehicle and powertrain, c_x is the aerodynamic coefficient of the vehicle, and T_{rr} is the rolling resistance. Finally, the brake torque is defined as

$$T_{br}(P_{wheel}) = K_b(P_{wheel} - P_{po})$$

12

where K_b and P_{po} are the brake torque constant and pushout pressure, respectively (Maciuca, 1997).

By applying the conservation of mass to the intake manifold, the mass of air in the manifold is defined by

$$\dot{m}_a = MAX\,TC(\alpha)\,PRI(m_a) + \dot{m}_{ao}(\omega_e, m_a)$$

2.3.2 Upper Level of the Physical Layer Controller: Torque Control

The main goal of the physical layer longitudinal controller is to effectively linearize the vehicle dynamics through feedback such that the vehicle dynamics become

$$\ddot{x} = u_{isl}$$

where u_{isl} is the synthetic input, or desired acceleration, given by the regulation layer. This allows the designer to completely specify the dynamic behavior of the vehicle via the choice of the synthetic input. However, notice that direct control of $\ddot{x}$ is not possible since the control inputs (the throttle angle α and the brake pressure P_{wheel}) do not directly affect it. The control objective can only be achieved by controlling the net torque T_{net} and the brake torque T_{br}. In addition, the use of the brakes and throttle should be mutually exclusive to minimize actuator usage and wear and tear on the vehicle. Therefore, considering the net torque and brake torque as new *pseudo-inputs*, the goal above can be achieved by choosing

$$T_{net}(m_a, \omega_e) = \frac{J_e}{R^*h}u_{isl} + c_x R^{*3}h^3\omega_e^2 + R^*(T_{rr} + T_{br}(P_{wheel}))$$

when throttle control is required and

$$T_{br}(P_{wheel}) = \frac{J_e}{R^*h}u_{isl} - T_{net}(m_a, \omega_e) + c_x R^{*3}h^3\omega_e^2 + R^*T_{rr}$$

when the brakes are needed. These terms are not true control inputs, since dynamics exist between the torques and the actual control inputs, namely the throttle angle and brake pressure. Therefore, another level of control is required to attain these desired torques using the true control inputs. However, a methodology for choosing between throttle and brake control will be discussed next.

2.3.3 Middle Level of the Physical Layer Controller: Switching Logic

As mentioned above, the throttle and brake commands should be mutually-exclusive to reduce actuation and system wear (ie. a human driver rarely uses both the throttle and brakes at the same time). However, some type of switching logic is required to decide when each type of control should be used (Gerdes and Hedrick, 1995). Intuitively, the brakes should be used only when the natural braking forces on the vehicle, such as aerodynamic drag, rolling resistance, and engine braking, are not sufficient to achieve the desired synthetic input. Written more mathematically, this idea can be expressed as

$$\begin{aligned}
u_{isl} - a_{res} > \lambda_u &\quad\Rightarrow\quad throttle \\
u_{isl} - a_{res} < \lambda_l &\quad\Rightarrow\quad brake \\
\lambda_l \leq u_{isl} - a_{res} \leq \lambda_u &\quad\Rightarrow\quad wait
\end{aligned}$$

where a hysteresis region has been added to reduce chattering around the switching line $u_{isl} - a_{res} = 0$ (Gerdes and Hedrick, 1995). Also, the residual acceleration a_{res} of the vehicle is

$$a_{res} = \frac{R^*h}{J_e}(T_{engbrk}(m_a, \omega_e) - c_x R^{*3} h^3 \omega_e^2 - R^*(T_{rr} + T_{br}(P_{wheel})))$$

2.3.4   Lower Level of the Physical Layer Controller: Throttle Control

Once the decision has been made to use the throttle, the desired value of the pseudo-input $T_{net}(m_a, \omega_e)$ is clearly defined by

$$T_{net}(\bar{m}_a, \omega_e) = \frac{J_e}{R^*h}u_{isl} + c_x R^{*3} h^3 \omega_e^2 + R^*(T_{rr} + T_{br}(P_{wheel}))$$

where $\bar{m}_a$ is the mass of air in the intake manifold necessary to achieve this desired net torque, which can be determined explicitly by inverting the nonlinearity $T_{net}(\bar{m}_a, \omega_e)$. Now, we will design a dynamic surface controller (Swaroop et al., 1996) to force m_a to track $\bar{m}_a$, which subsequently forces $\ddot{x}$ to track u_{isl}. Let's define the surface S_1 such that

$$S_1 = m_a - m_{a,des}$$

Then choosing the surface dynamics as

$$\dot{S}_1 = -K_1 S$$

and using the manifold dynamics presented in Section 2.3.1 the following relationships for the commanded throttle angle α_c and the desired mass of air $m_{a,des}$ can be determined

$$\alpha_c = TC^{-1}\left(\frac{\dot{m}a_o(m_a, \omega_e) + \dot{m}_{a,des} - K_1 S_1}{MAX\ PRI(m_a)}\right)$$
$$\tau_1 \dot{m}_{a,des} + m_{a,des} = \bar{m}_a$$

A similar derivation will now be performed for the accompanying brake controller.

2.3.5   Lower Level of the Physical Layer Controller: Brake Control

Once the decision has been made to use the brake, the desired value of the pseudo input $T_{br}(P_{w}heel)$ is clearly defined by

$$T_{br}(\bar{P}_{wheel}) = \frac{J_e}{R^*h}u_{isl} - T_{net}(m_a, \omega_e) + c_x R^{*3} h^3 \omega_e^2 + R^* T_{rr}$$

Therefore, the required brake pressure at the wheel $\bar{P}_{wheel}$ are found to be

$$\bar{P}_{wheel} = \frac{1}{K_b}\left(\frac{J_e}{R^*h}u_{isl} - T_{net}(m_a, \omega_e) + c_x R^{*3} h^3 \omega_e^2 + R^* T_{rr} + P_{po}\right)$$

Now, define the surface S_2 to be
$$S_2 = P_{wheel} - P_{wheel,des}$$

and the surface dynamics to satisfy

$$\dot{S}_2 = -K_2 S$$

then the resulting commanded master cylinder pressure P_{mcc} and the desired brake pressure at the wheel $P_{wheel,des}$ is described by

$$P_{mcc} = \begin{pmatrix} P_{wheel} + \Delta_{pb} & \text{if } (\dot{P}_{wheel,des} - K_2 S_2) > 0 \\ P_{wheel} - \Delta_{pb} & \text{otherwise} \end{pmatrix}$$

$$\Delta_{pb} = \frac{(\dot{P}_{wheel,des} - K_2 S_2)^2}{C_q^2}$$

$$\tau_2 \dot{P}_{wheel,des} + P_{wheel,des} = \bar{P}_{wheel}$$

2.4 Longitudinal Control at the Regulation Layer: Synthetic Acceleration

As stated in section 2.3.2, the physical layer controller results in direct specification of the vehicles acceleration via the synthetic input u_{isl}. In the case of the PATH AHS, the synthetic input is then chosen by the regulation layer so that the vehicle performs a specific maneuver specified by the coordination layer, such as merging into a platoon or become the leader of a new platoon. For the purposes of the fault diagnostics, the vehicle is assumed to only perform the "follower" maneuver, that is the vehicle attempts to maintain a given intervehicle spacing.

In addition, the follower control law must ensure that the platoon is *string stable*. String stability guarantees that any spacing error due to the current vehicle is not amplified by the vehicles farther back in the platoon. Swaroop (Swaroop, 1994) demonstrated that for a constant spacing policy, then velocity and acceleration information about the lead and previous vehicles in the platoon are sufficient to provide string stability. For the purposes of this report, we will consider only the follower control law currently used on the experimental test vehicles for the second vehicle in the platoon. This control law is as follows:

$$u_{isl} = a_{prev} - 2\zeta\omega_m\dot{\epsilon} - \omega_m^2\epsilon \tag{2.2}$$

where a_{prev} is the previous vehicles acceleration, $\dot{\epsilon}$ is the relative velocity between the current and previous vehicle, ϵ is the spacing error of the current vehicle, and ζ and ω_m are controller design parameters.

2.5 Experimental Vehicles

The lateral and longitudinal controllers presented in the previous sections have been successfully implemented and tested on a fleet of nine Buick LeSabre by researchers and staff at PATH. These experimental vehicles have been outfitted with additional hardware to provide the capability of automated control. A drawing of the vehicles with the added hardware is shown in Fig. 2.5. Each vehicle uses a ruggedized 166 MHz Pentium running the QNX operating system to run the both the lateral and longitudinal control software. The control software accesses the communications, sensor measurements and actuator commands via a publish/subscribe database which provides the information

every 21 msec. Interaction with the hardware itself is handled by separate software tasks in order to simplify development. The interested reader is referred to (Staff, 1998) for a more detailed description of the hardware and software used in the experimental vehicles. The next two subsections will describe the hardware essential to the operation of the lateral and longitudinal control systems.
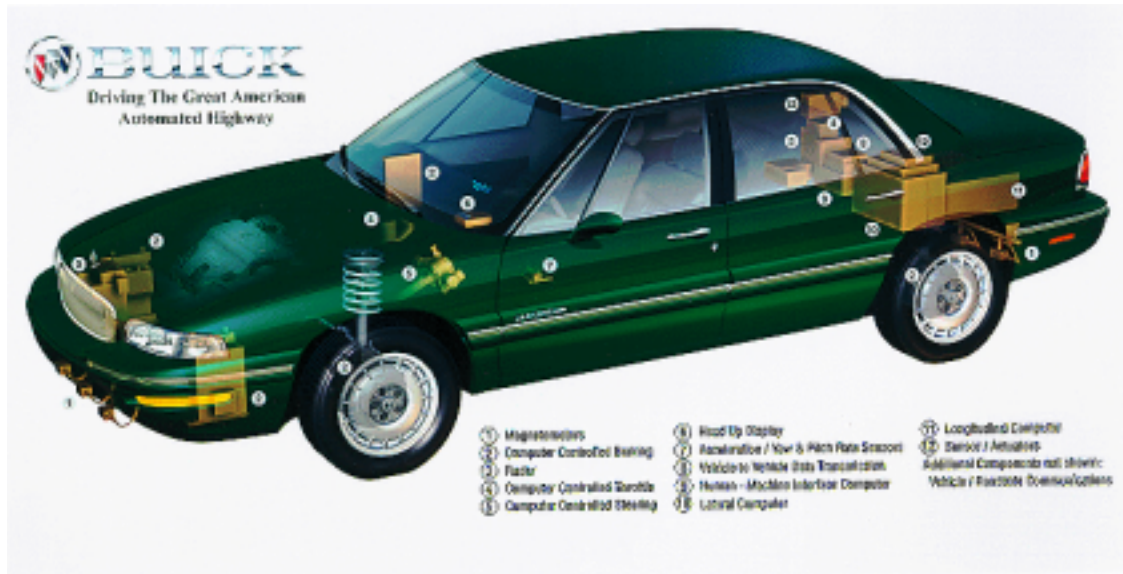
Figure 2.5: Cutaway Drawing of the PATH Experimental Vehicles

2.5.1   Lateral Control Hardware

In this subsection, we describe the lateral control system and it's associated hardware developed as part of PATH's automated highways initiative. Fig. 2.6 shows a schematic of this system. A magnet-magnetometer based system is used to realize lane-keeping. Magnets are laid out along the center of lanes. The lane-keeping control problem then boils down to ensuring that vehicles follow the series of magnets which represent the lane centerline. The vehicles in turn, have a set of sensors (referred to as **magnetometers** in the rest of the paper) that measure the lateral deviation of their location with respect to the magnets (road centerline). The lateral error information is processed by the on-board computer to generate the steering angle required to follow the road centerline. PATH's passenger vehicle hardware architecture consists of two sets of magnetometers mounted under the front and rear bumpers of the vehicle. Each magnetometer set consists of three magnetometers. These magnetometers are used to increase the range of measurement to about 0.5 m. The other sensors show in Fig. 2.6 are used for lane-changing and other purposes.

2.5.2   Longitudinal Control Hardware

Having reviewed the longitudinal controller design in section 2.3, there are seven sensors and two actuators required for the longitudinal controller at the physical layer. In addition, a communication system will be required to receive information about the lead and previous vehicles in the platoon. The following table summarizes the sensors and actuators which are required. In addition, the
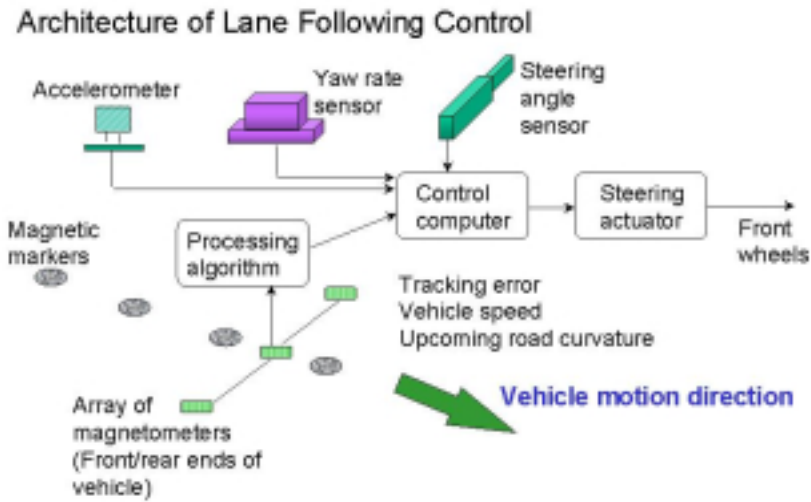
Figure 2.6: Schematic of the lateral control system developed by PATH

standard deviation of normally distributed noise for each of the sensors after filtering is also included in the table, as well as the average time constants for first order actuator dynamics.

Table 2.2: Sensor and Actuator Characteristics

Sensors & Actuators	Typical Variance
Radar	2.5 cm in range,
Accelerometer	0.1 m/sec^2
Wheel Speed Sensor	0.03 m/sec
Throttle Angle Sensor	0.1 degrees
Brake Pressure Sensor	70 KPa
Manifold Pressure Sensor	0.25 KPa
Engine Speed Sensor	1 rpm
Throttle Actuator (Stepper Motor)	0.01 sec
Brake Actuator (Hydraulic System)	0.1 sec

2.6   Conclusions

This chapter presented the underlying heirarchical structure of the PATH AHS architecture, the design of the existing lateral and longitudinal controllers at the physical layer of this hierarchy, and a brief overview of the experimental vehicles used to realize the AHS. These topics should give the reader a good indication of the framework in which the fault tolerant control system must be

incorporated, as well as the experimental test bed in which it will be verified. Furthermore, the vehicle models and control laws developed above will be directly used in the development of fault tolerant control system in the subsequent chapters.

Chapter 3

Design and Testing of Fault Tolerant Lane-keeping Controllers

This chapter documents the design and results of experimental testing of fault tolerant controllers for the **lane-keeping control system** of PATH's passenger vehicles. We would like to clarify, early in this discussion, that by fault tolerant controllers we mean, controllers that are insensitive to certain faults that may occur in the system. In other words, implementation of fault tolerant controllers guarantee that even in the event of certain failures in the components of the lateral control system, the vehicle can be steered satisfactorily **without switching to degraded modes** of operation.

The following questions arise naturally. What are the faults that might typically occur that we would like to make our control system insensitive to? Why do we need fault-insensitive lateral control action? What are possible design techniques that could be used to design these fault tolerant controllers? How effective are these controllers in practice? These questions, and others, are addressed in the sections of this chapter.

3.1   What Are the Failures?

In this section we address the question: What are the faults that we would like to make the lane-keeping control system insensitive to? It is clear, from the outset, that it will not be practically feasible to design control algorithms that are insensitive to **all** possible faults in the lateral control system. Two reasons come to mind. First, it is a practical nightmare to list **all** possible faults that might occur in a system. Second, even if it were possible to list all faults, one can expect that the system dynamics exhibited by each of the faulty states will be so drastically different that one single control algorithm will not fit all these situations. We, therefore, limit our attention to a few faults.

To address the question of what faults we would like the lane-keeping control system to be insensitive to, we need to understand the faults that can typically occur in the lane-keeping control system of the passenger vehicles. For this purpose, we revisit the lateral control system architecture. (For a more detailed discussion, refer Chapter 2). The lateral control system consists of two sets of magnetometers mounted on the front and rear bumpers of the vehicles, one steering actuator mounted on the steering column, a yaw rate gyro and an accelerometer mounted at the vehicle CG

(approximately!), an encoder that measures the motion of the steering actuator (mounted near the steering wheel) and a potentiometer that measures the actual motion of the tire. The components used for lane-keeping control are the two sets of magnetometers, the steering actuator and the inner-loop components. Failure of the steering actuator is a severe problem. In most situations, it would necessitate bringing the affected vehicle to a halt as soon as possible.

In this chapter, we will focus on the failure of the magnetometers. Each set of magnetometers consists of three magnetometers (three magnetometers are used to increase the range of measurement to 0.5 m). Magnetometer failures that will be addressed in this chapter include:

- **Fault 1**: DC bias in the sensor reading: This is regarded as a failure when the bias reaches large magnitudes (of the order of the measurement). Under "normal" operation, from experience we typically see a bias of the order of 2-3 cm.

- **Fault 2**: Hardware failure in the magnetometers: This is detected by a magnetometer monitoring signal built into the magnetometers used in the PATH vehicles (supplied by Applied Physics Systems). In the event that the magnetometer monitor detects a failure, the magenetometer output is set to maximum

- **Fault 3**: Sensor electrical disconnection due to severance of wires, clogging due to snow etc. We shall model this as the magnetometer output returning a zero.

We restrict our attention to these faults since all these failures have been experienced before during experimental testing of various PATH vehicles.

3.2 Motivation for Fault Tolerant Control

Naturally, the first thing to do is to investigate if the "current" lateral control algorithm (used in Demo '97) is capable of handling the faults described above. (See Chapter 2 for details regarding the existing lateral control algorithm). In the interest of brevity, we mention only the results of our study in this direction. The lateral control scheme (described in Chapter 2) used currently can handle significant amounts of bias (fault #1) but cannot handle situations arising out of faults #2 and #3.

As mentioned earlier, we are interested in the design and testing of fault tolerant controllers (controllers that are insensitive to the faults described in the previous section). Another way of handling a faulty situation is to first detect and identify the faulty component and then switch to a degraded mode of action. We choose the former strategy for the following reasons.

1. The lateral dynamics exhibited by passenger vehicles necessitate high bandwidth control action i.e., quick steering action is required to control the vehicle. This means that significant delays in the lateral control loop cannot be tolerated. Experiments have shown that at a cruise speed of 50 mph, a delay of more than 0.3 sec can start to have an influence on the lateral control performance. Any reliable failure detection and identification (FDI) system will have an inherent delay built into it which may cause the vehicle to go unstable during the detection and identification process.

2. Since fault tolerant control strategies guarantee stability, a reliable FDI scheme followed by a suitable reconfiguration strategy can form a layer on top of the fault tolerant framework. (Development of degraded mode lateral control strategies is the focus of MOU 384/TO 4204).

In the next two sections we shall detail the procedures used to design fault tolerant lateral control algorithms for passenger vehicles. Two approaches are presented. The first based on simultaneous stabilization theory and the second based on the concept of an observer based look-ahead. The first scheme can, currently, be used to handle **fault #3**. The second scheme can be used to handle **faults #1, #2 and #3**.

3.3 Fault Tolerant Lane-Keeping Control Based on Simultaneous Stabilization

Every physical system (faulty or non-faulty) demonstrates certain dynamic behavior. It is the job of the controller to generate suitable inputs to the dynamic system in order that the system behaves satisfactorily (in our case the dynamic system is the lateral dynamics of passenger vehicles).

It is natural, therefore, to formulate the effect of a fault as a transition from one dynamic system (or plant) to the other. Fig. 3.1 illustrates this idea. Note that the faulty and non-faulty plants may behave drastically differently. Viewed in this perspective, the problem of designing a fault tolerant controller boils down to the design of a control algorithm that guarantees simultaneous stability (and performance) of the non-faulty plant with each one of the faulty modes.
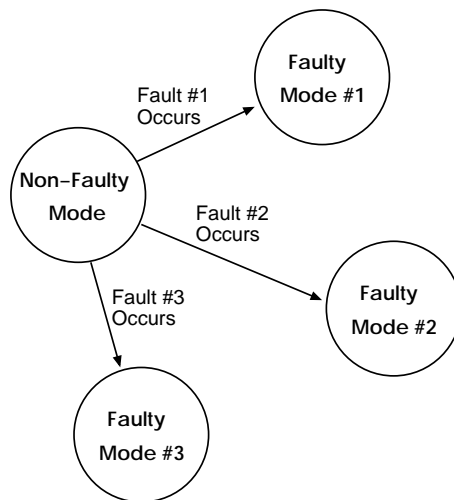
Figure 3.1: Formulation of Effects of Fault as a Finite State Machine

Simultaneous stabilization theory provides a framework to design such control algorithms. In this section, we will first provide a brief background into the history of the theoretical development of this problem. Included in this will be a description of the design technique developed by

Suryanarayanan et al. (et al, 2000). *This design technique will then be applied to make the control algorithm insensitive to magnetometer disconnection failure.*

3.3.1 History of simultaneous stabilization theory

Over the last two decades, the problem of simultaneous stability has received considerable attention. The problem (LTI case) reads as: Given a finite number of LTI plants P_1, P_2, $\cdots$, P_k does there exist a single LTI controller, C, such that each of the feedback interconnections (P_i, C) $(i = 1, 2, \cdots, k)$ is internally stable? Though simply stated, this problem has been found to be extremely difficult to solve for the general case.

The simultaneous stability problem can be interpreted as a robust control problem where the uncertainty in the plant is described in a finite way. Finite descriptions of uncertainty appear naturally in practical situations. For example, the k systems may a represent nominal system and many of its failed modes (E., 1983), a system that has several operating points (J., 1985) or a multivariable system with possible loss of sensors or actuators (A., 1983). We refer the reader to the monograph by J. (1985) for many more illustrative examples of applications of simultaneous stabilization.

The first explicit statement of the problem of finding necessary and sufficient conditions for the existence of a simultaneously stabilizing controller was made by R. and J. (1982). Necessary and sufficient conditions for the existence of a simultaneously stabilizing controller for two plants were developed by M. and N. (1982) (also by R. and J. (1982). However, the problem of finding necessary and sufficient conditions for the existence of simultaneously stabilizing controllers for three or more plants remained unsolved for more than a decade. In a series of papers in the early 90's (V., 1991; et al., 1993; V and M., 1993), Blondel showed that the problem of determining necessary and sufficient conditions for simultaneous stability of three or more plants is undecidable through rational operations on the coefficients of the polynomials in the transfer functions that describe the LTI plants. These papers by Blondel virtually brought the search for (tractable) necessary **and** sufficient conditions for simultaneous stabilizability of three or more plants to a standstill.

Throughout the development of the theory of simultaneous stabilization, few efforts have focused on the practical schemes for the **design** of simultaneously stabilizing controllers. Design schemes developed thus far have been of pedagogical nature. In this manuscript, we present a design technique for simultaneously stabilizing controllers developed by et al (2000) which lends itself nicely to the problem under consideration, namely making the control system insensitive to fault #3. We would like to mention at this point that theory of simultaneous stability allows us to handle more than one fault. However, the **design** technique for such controllers is still under development.

3.3.2 Design of simultaneously stabilizing controllers

In this subsection, we present the mathematics behind the design of simultaneously stabilizing controllers. First, we present the expression of a sufficient condition for simultaneous stability for a strictly proper linear-time invariant plants as an LMI constraint. (In the interest of brevity, we do not include proofs here). We then show that, with the help of this LMI constraint the design of

a simultaneously stabilizing controller (that guarantees satisfactory performance for the non-faulty mode) can be cast as a standard $\mathcal{H}_\infty$ control problem.

Sufficient condition for simultaneous stability as an LMI

NOTATION/PRELIMINARIES

Complex Plane

- **R**, **C** are the sets of real and complex numbers. ∞ is the point at infinity

- $\mathbf{C}_\infty := \mathbf{C} \cup \infty$ is the extended complex plane. $\mathbf{R}_\infty$ is defined similarly

- $\Re(s)$ and $\Im(s)$ are the real and imaginary parts of complex number s

- $\mathbf{C}_+ := \{s \in \mathbf{C} : \Re(s) \geq 0\}$

Sets of Functions

- $\mathcal{R}$(s): set of proper real rational functions in the the variable s

- $\mathcal{S}$(s): set of proper real rational functions with no poles in $\mathbf{C}_+$ (called stable rational functions)

- $\mathcal{U}$(s) $\in \mathcal{S}$(s): set of stable rational functions such that for every $u(s) \in \mathcal{U}$(s), $\frac{1}{u(s)} \in \mathcal{S}$(s)

Definitions

- For $P(s), C(s) \in \mathcal{R}$(s), the feedback interconnection $(P(s), C(s)$ is said to be internally stable if each of $G_1 := \frac{PC}{1+PC}$, $G_2 := \frac{C}{1+PC}$ and $G_3 := \frac{P}{1+PC}$ belong to $\mathcal{S}$(s) interconnection $(P(s), C(s))$ is internally stable

- $P_1(s), P_2(s), \cdots, P_k(s) \in \mathcal{R}$(s) are said to be simultaneously stabilizable if there exists $C(s) \in \mathcal{R}$(s) such that each of the feedback interconnections $(P_i(s), C(s)), (i = 1, 2, \cdots, k)$ is internally stable

Theorem 3.1 (Saeks and Murray, 1982) $P_0 = \frac{N_0}{D_0}$, $P_1 = \frac{N_1}{D_1} \in \mathcal{R}$(s) *are simultaneously stabilizable iff the following three conditions hold.*

1. $D_1 D_0$ *takes constant sign at all zeros of $P_1 - P_0$ on the real axis in* $\mathbf{C}_+$

2. $N_1 N_0$ *takes constant sign at all common poles of P_0 and P_1 on the real axis in* $\mathbf{C}_+$

3. *Two signs obtained above are the same*

Theorem 3.2 (Vidyasagar and Viswanadham, 1982) *Let the coprime factorizations of the two plants, $P_i(s)$ $(i = 0, 1)$ over $\mathcal{S}$(s) be*

$$P_i = N_i D_i^{-1} = \tilde{D}_i^{-1} \tilde{N}_i \quad (i = 0, 1) \tag{3.1}$$

23

Then there exist X_i, Y_i, $\tilde{X}_i$ and $\tilde{Y}_i$ such that

$$\begin{pmatrix} Y_i & X_i \\ -\tilde{N}_i & \tilde{D}_i \end{pmatrix} \begin{pmatrix} D_i & -\tilde{X}_i \\ N_i & \tilde{Y}_i \end{pmatrix} = \begin{pmatrix} I & 0 \\ 0 & I \end{pmatrix} \tag{3.2}$$

$$\begin{pmatrix} D_i & -\tilde{X}_i \\ N_i & \tilde{Y}_i \end{pmatrix} \begin{pmatrix} Y_i & X_i \\ -\tilde{N}_i & \tilde{D}_i \end{pmatrix} = \begin{pmatrix} I & 0 \\ 0 & I \end{pmatrix} \tag{3.3}$$

Define

$$V := Y_0 D_1 + X_0 N_1, \quad W := -\tilde{N}_0 D_1 + \tilde{D}_0 N_1. \tag{3.4}$$

Then the class of all simultaneously stabilizing controllers ($\in \mathcal{R}(s)$) is given by

$$C_{sim} = \left\{ (Y_0 - Q_c \tilde{N}_0)^{-1}(X_0 + Q_c \tilde{D}_0), \ Q_c \in \mathcal{M} \right\} \tag{3.5}$$

where

$$\mathcal{M} = \{Q_c : Q_c \in \mathcal{S}, V + Q_c W \in \mathcal{U}\} \tag{3.6}$$

Lemma 3.1 (Suryanarayanan et al, 2000a) *Let P_0, P_1 be two SISO linear time-invariant systems. Then $\exists N_i, D_i, X_i, Y_i \in \mathcal{S}$ ($i = 0, 1$) such that $P_i = \frac{N_i}{D_i}$ and $X_i N_i + Y_i D_i = 1$.*

Define $V := Y_0 D_1 + X_0 N_1$ and $W := -N_0 D_1 + D_0 N_1$. If P_0 and P_1 are strictly proper, then $\frac{1}{V} \in \mathcal{S}(s)$.

Now define, $R := WV^{-1}$. If $R \in \mathcal{S}(s)$, then P_0 and P_1 are simultaneously stabilizable if $\|Q_c R\|_\infty < 1$.

Proof: : The proof of this lemma derives its basis from theorem 3.2. Refer (et al, 2000) for details. ∎

Design problem formulation

Now consider the problem: Design a controller which optimizes a performance measure during non-faulty operation (P_0) while guaranteeing simultaneous stability of P_0 and P_1. Applying the LMI condition (sufficient) for simultaneous stability, we restate the problem mathematically as:

$$\min_{Q_c} \|W_y(Y_0 - N_0 Q_c) D_0 G_0\|_\infty \text{subject to} \|Q_c R\|_\infty < 1$$

where R, Y_0, N_0, N_0 are as defined in Theorem 3.1, G_0 represents the disturbance dynamics and W_y is a weighting function that weights the controlled output in the appropriate frequency ranges.

For SISO plants, the above problem can be treated as a standard $\mathcal{H}_\infty$ problem. Fig. 3.2) shows why this is so. The augmented plant acts as the "generalized plant" and Q_c as the "stabilizing controller" for the generalized plant. The cost function to be minimized may be interpreted as the $\mathcal{H}_\infty$
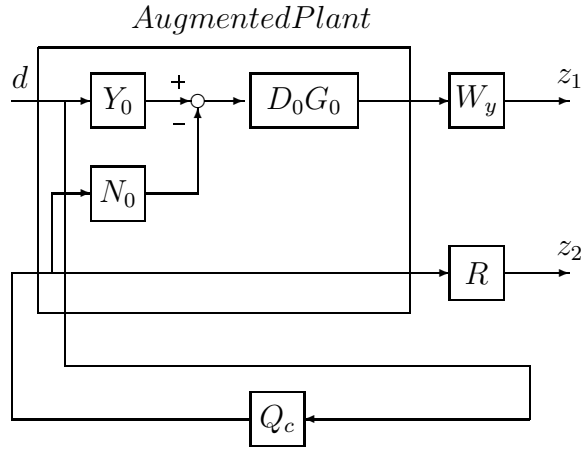
Figure 3.2: Augmented Plant for the design of Q_c

norm from signal d to z_1 and z_2.

In general, $\mathcal{H}_\infty$ control synthesis technique can yield an unstable controller, in this case, Q_c. This leads to the failure in the achievement of the design goals. However, it turns out that in most cases, the stabilizing controller is itself stable.

We now summarize the entire design procedure for the design of simultaneously stabilizing controllers for **two strictly proper plants, P_0 and P_1**.

- Step 1: Decide on co-prime factorizations of P_0 and P_1 which yield stable R

- Step 2: Specify the weighting function W_y

- Step 3: Find the solution $Q_c \in \mathcal{S}$(s) for the above $\mathcal{H}_\infty$ control problem

- Step 4: If $\|Q_c R\|_\infty \geq 1$, then modify W_y (for eg. reduce the gain and/or cutoff frequency) and go to Step 2.

3.3.3 Application to lane-keeping control

In this subsection, we shall demonstrate the application of results from simultaneous stabilization theory and the design technique detailed above to the problem of design of a lane-keeping controller which is insensitive to magnetometer disconnection (fault #3). We wish to mention again that we model magnetometer disconnection as the output of the disconnected magnetometer going to zero and remaining at zero thereafter. We will use the geometric look-ahead scheme for lane-keeping control and use the bicycle model for control design purposes.

The state equation that describes the 4-state bicycle model for front wheel steered passenger vehicles are:

$$\dot{\xi} = A\xi + B\delta + W\rho \tag{3.7}$$
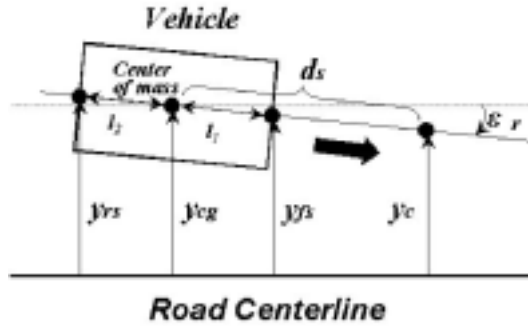
Figure 3.3: Geometric Look-Ahead Scheme

where, $\xi=[y_{cg} \ \dot{y}_{cg} \ \epsilon_r \ \dot{\epsilon}_r]$(refer Fig. 3.3 for variable definitions)

$$
A = \begin{bmatrix} 0 & 0 & 0 & 0 \\ 0 & -\frac{a_{11}}{\dot{x}} & a_{11} & \frac{a_{12}}{\dot{x}} \\ 0 & 0 & 0 & 1 \\ 0 & -\frac{a_{41}}{\dot{x}} & a_{41} & \frac{a_{12}}{\dot{x}} \end{bmatrix} \quad B = \begin{bmatrix} 0 \\ b_{21} \\ 0 \\ b_{41} \end{bmatrix} \quad W = \begin{bmatrix} 0 \\ w_{21} \\ 0 \\ w_{41} \end{bmatrix}
$$

$a_{11} = (\phi_1 + \phi_2)$, $a_{12} = \phi_1(d_s - l_f) + \phi_2(d_s + l_r)$, $a_{41} = \frac{l_f C_f - l_r C_r}{I_z}$

$a_{42} = \frac{l_f C_f(d_s - l_f) + l_r C_r(d_s + l_r)}{I_z}$, $b_{21} = \phi_1$, $b_{41} = \frac{l_f C_f}{I_z}$, $w_{21} = -\frac{l_1^2 C_f + l_2^2 C_r}{I_z}$, $w_{41} = \phi_2 l_r - \phi_1 l_f - \dot{x}^2$

$\phi_1 = C_f \left(\frac{1}{M} + \frac{l_f d_s}{I_z} \right)$, $\phi_2 = C_r \left(\frac{1}{M} - \frac{l_r d_s}{I_z} \right)$

δ is the steering angle and $\rho = \frac{\dot{\epsilon}_d}{\dot{x}}$ is the curvature of the road at the point on the road nearest the center of gravity. Table 3.1 explains the symbols that are used in the above equations.

Table 3.1: Parameters used in the Bicycle Model

Param.	Description	Values
M	Mass of the vehicle	1700-2100 kg
I_z	Yaw moment of inertia	≈ 2870 kg m^2
l_f	CG-front axle dist.	0.9 - 1.2 m
l_r	CG-rear axle dsit	1.5 - 1.8 m
C_f	Cor. stiff. - Front tire	≈ 70000 N/rad
C_r	Cor. stiff. - Rear tire	≈ 130000 N/rad
$v, \dot{x}$	Forward vel. of vehicle	0-35 m/s
d_s	Dist. of sensor from CG	-3 to 10 m

26

The lateral errors measured at the location of the magenetometers are:

$$y_{fs} = C_{fs}x = (1\ 0\ l_f\ 0)x \tag{3.8}$$
$$y_{rs} = C_{rs}x = (1\ 0\ -l_r\ 0)x \tag{3.9}$$

where l_f, l_r are distances of the front and rear magnetometers from the vehicle CG.
For small relative yaw angles, the error at the location of the virtual sensor (which is at a distance d_s from the vehicle CG) is:

$$y_c = C_0 x \approx \frac{\{(l_r + d_s)C_{fs} + (l_f - d_s)C_{rs}\}}{(l_f + l_r)}x \tag{3.10}$$

The above equation changes to:

$$y_c = C_{1f}x = \frac{(l_f - d_s)C_{rs}}{(l_f + l_r)}x \tag{3.11}$$

for the loss of the front magenetometer ($y_{fs} = 0$) and,

$$y_c = C_{1r}x = \frac{(l_r + d_s)C_{fs}}{(l_f + l_r)}x \tag{3.12}$$

for the loss of the rear magnetometer ($y_{rs} = 0$).

Then $P_{nom} = \frac{(l_f - d_s)C_{rs}}{(l_f + l_r)}(sI - A)^{-1}B$, $P_f = \frac{(l_r + d_s)C_{fs}}{(l_f + l_r)}(sI - A)^{-1}B$ and $P_r = \frac{(l_f - d_s)C_{rs}}{(l_f + l_r)}(sI - A)^{-1}B$. The problem is to design a simultaneously stabilizing controller that stabilizes (P_{nom}, P_f) and (P_{nom}, P_r). We now apply Theorem 3.1 to determine conditions for simultaneous stability.

Property 1: Consider the case that we "lose" the front magnetometer. In this case P_{nom} and P_r are simultaneously stabilizable if and only if $d_s \leq l_f$.

Property 2: Consider the case that we "lose" the rear magnetometer. In this case P_{nom} and P_f are simultaneously stabilizable if and only if $d_s \geq -l_r$.

The proof of the two properties is a straight forward application of Theorem 3.1.

The implications of the properties are worth commenting on. The properties say that if we have to make the lane-keeping control system insensitive to sensor disconnection of any of the two magnetometers (and use the geometric look-ahead scheme), then we would need to restrict d_s to $-l_r \leq d_s \leq l_f$. This implies that the largest look-ahead distance we can achieve is only as far as the front magnetometers are in front of the CG (approximately 2m). We had alluded to earlier in chapter 2 that at high speeds, larger d_s values contribute towards better yaw damping characteristics and consequently a more comfortable ride. Therefore, the requirement for fault tolerance poses a limitation on achievable performance. This trade-off is something we should naturally expect.

3.3.4 Controller characteristics and simulation results

The fault tolerant controller was designed based on the scheme described in the previous earlier. (Note: d_s is restricted so that $-l_r \leq d_s \leq l_f$).

The frequency characteristics of the controller and the design parameter Q_c are shown in Fig. 3.4. Also shown is the sufficient condition of simultaneous stability ($\|Q_c R\|_\infty < 1$) being satisfied. Note that the controller has a "lead-lag" nature. Also the failure mode $\approx$ 1Hz is well captured in Q_c's characteristics. d_s value of **1.5m** is used.
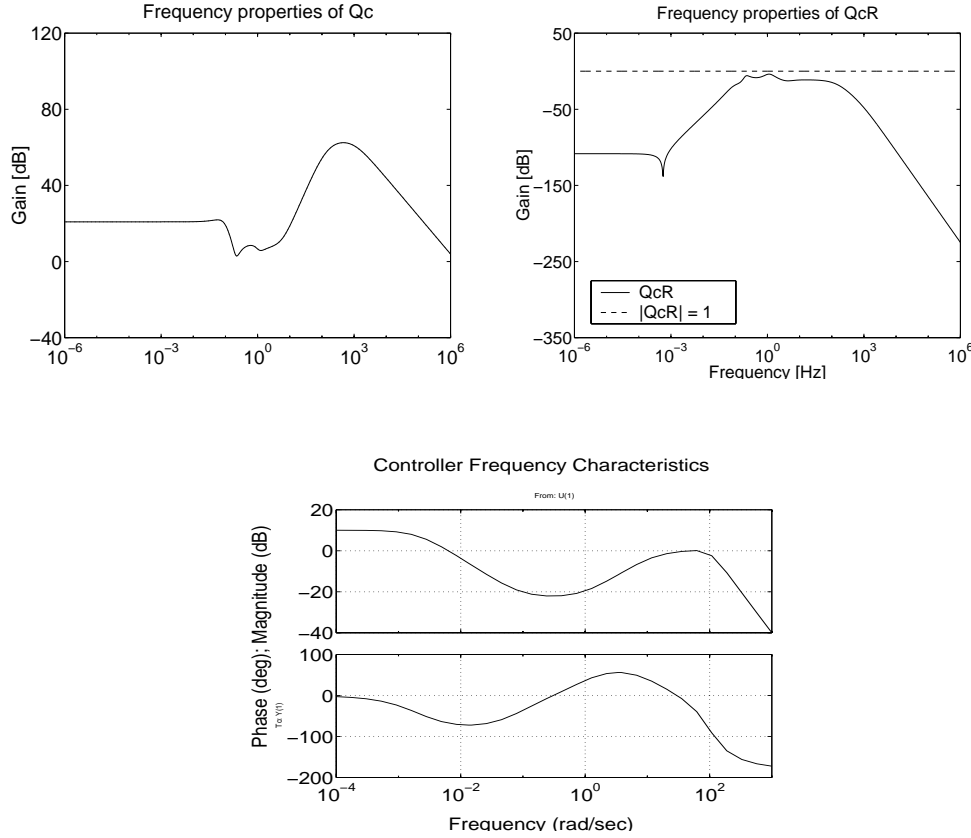
Figure 3.4: Frequency characteristics of designed controller and Q_c, d_s=**1.5m**

Fig. 3.5 and Fig. 3.6 show the results for the cases when the system "loses" the front magnetometer and rear magnetometer respectively. During the event of the fault, the vehicle is on a curve of radius 800m. This is more serious than a fault occurring when the vehicle is on the straight section of the highway. Noise of about 2cm (RMS) (experienced in practice) has been added to the output of each magnetometer.

We observe in Fig. 3.5 that the lateral error is about 0.05m on a curve of radius 800m before the fault occurs (t=15-20s). This is indeed a satisfactory level of performance during non-faulty operation. However, when the fault occurs the maximum lateral error increases to about 20cm(0.2m).

28

Also, stability is maintained because the condition for simultaneous stability is satisfied. The failure of the rear magnetometer (refer Fig. 3.6) does not affect the performance of the system significantly. This is because the loss of the rear magnetometer does not affect the stability of the system for positive look-ahead distances.
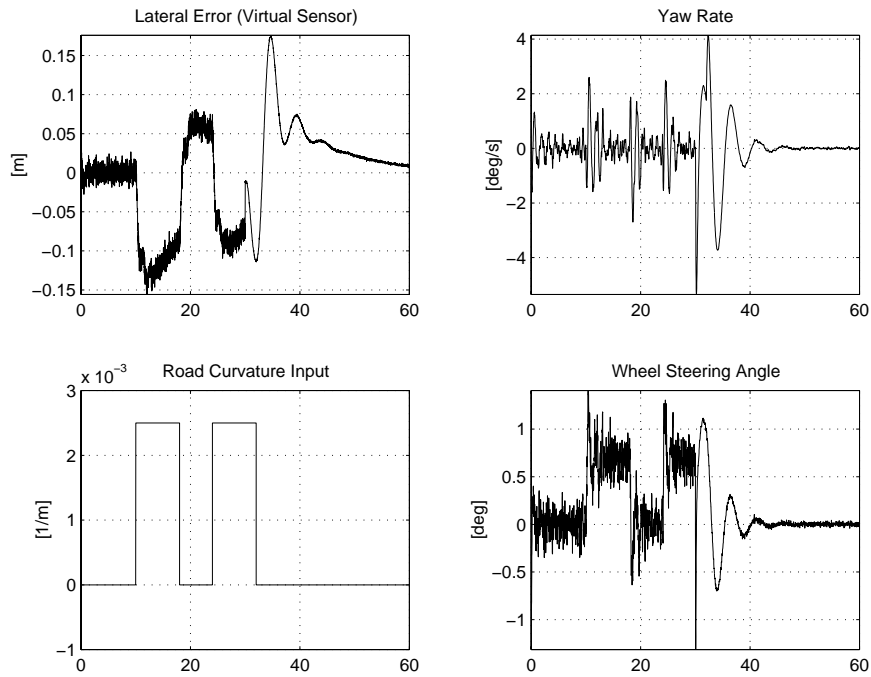
Figure 3.5: Simulation of loss of front magnetometer at t=30s for v=25m/s
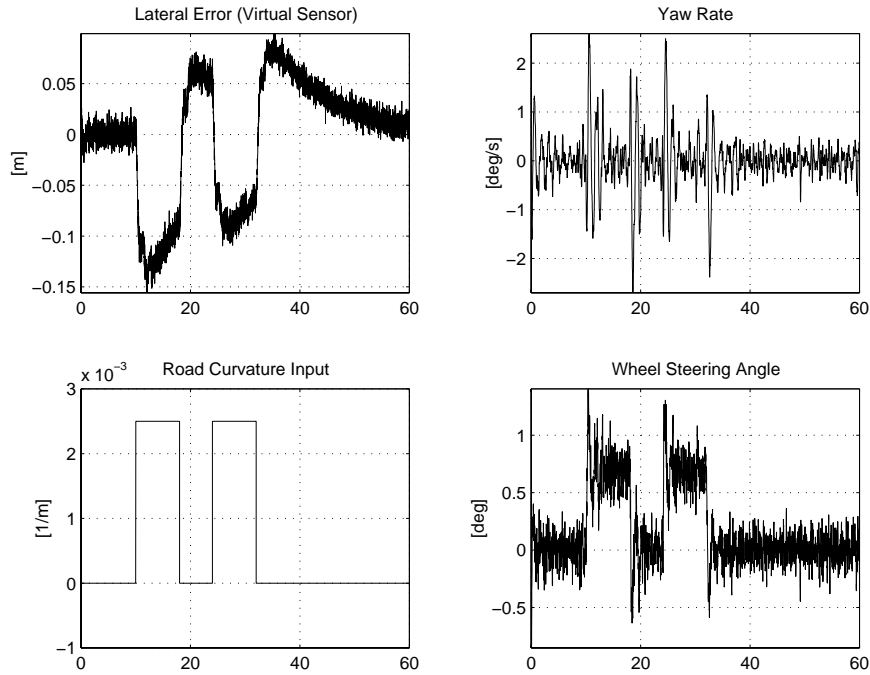
Figure 3.6: Simulation of loss of rear magnetometer at t=30s for v=25m/s

3.4 Observer Based Look-Ahead Scheme for Fault Tolerant Lateral Control

In this section, we will present a lane-keeping control scheme based on the concept of *Observer Based Look-Ahead*. This scheme is proposed to deal with faults # 1, # 2 and # 3 (refer section 3.1).

Chapter 2 discussed the intricacies of the vehicle lane-keeping control problem and included a description of the geometric-look ahead scheme (which formed the basis for the lane-keeping controller implemented in Demo'97). In the previous section, we discussed how we could accommodate fault #3 into the control design process. We obtained a powerful result which states that if the geometric look-ahead scheme is used, the condition for fault tolerance demands that the look-ahead distance has to be limited to about 2m (location of the front set of magnetometers). Smaller look-ahead distances result in reduced damping and therefore increased oscillations. The motivation to develop an observer based look-ahead scheme is to investigate if we can achieve fault tolerance **and** use larger look-ahead distances.

3.4.1 Observer based fault tolerant controller

The dedicated observer based architecture for the fault tolerant control design is shown in Fig. 3.7. In this scheme the controller acts on the estimated error at the virtual sensor rather than the "actual" error as generated by geometric scheme. The dedicated observer based on the front sensor has the
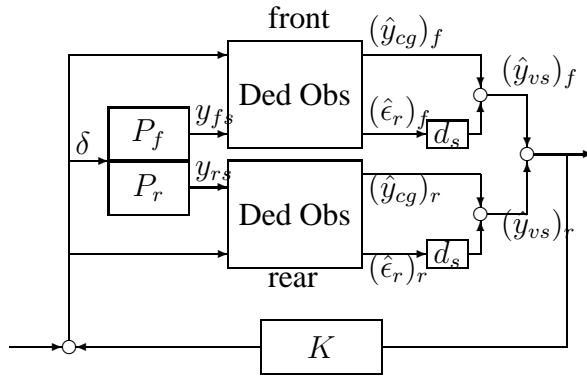
Figure 3.7: Dedicated Observer Based Design Scheme

steering angle, δ, and lateral error at the location of the front sensor, y_{fs}, as inputs. The dedicated observer based on the rear sensor has the steering angle, δ and the lateral error at the location of the rear sensor, y_{rs} as the inputs. Note that each of these observers generates **independent** estimates of the states of the bicycle model which are then combined to generate the estimates of the lateral error at the location of the virtual sensors.

The motivation for such a scheme is now clear. The look-ahead generation algorithm can be made robust to failure of one of the two magnetometers i.e., reliable estimates of the lateral error for large look-ahead distances can be obtained.

Define
$L_f :=$ transfer function from δ to $(\hat{y}_{vs})_f$
$L_r :=$ transfer function from δ to $(\hat{y}_{rs})_r$

Claim: If $L_f \approx L_r =: L$ (say) and there exists a controller K such that,

1. 2LK is stable under unity feedback

2. LK is stable under unity feedback

then, the system is stable both in the non-faulty case and when one of the magnetometers is lost.
An Argument in Favour: Consider the non-faulty case. In this case if $L_f \approx L_r$ is satisfied the open loop transfer function is given by 2LK. Condition (1) guarantees that the closed loop remains stable. In the faulty case, one of the magenetometer outputs is assumed to drop to zero (i.e., y_{fs} or y_{rs} becomes zero). Therefore if $L_f \approx L_r$ is satisfied, the open loop transfer function is given by $(1+\alpha)$LK. α captures the extent to which the faulty loop corrupts the estimation scheme. If α is small and condition 2 is satisfied, we can expect the overall system to still be stable.
Comments:

- The condition $L_f \approx L_r$ can be achieved because of the freedom to choose the observer gains. The condition $L_f \approx L_r$ can be written as:

31

$$G_{1_{yf}}P_f + d_s G_{1_{\delta f}} = G_{1_{yr}}P_r + d_s G_{1_{\delta r}}$$

$G_{1_{yf}}, G_{1_{yr}}, G_{1_{\delta f}}, G_{1_{\delta r}}$ can be chosen suitably by the designer

- The fault model considered here, namely the loss of information from one of the two magnetometers, essentially leads to a change in the open loop gain (from 2LK to LK). Since fault models are never known precisely, it is necessary that the fault tolerant control algorithm be robust to uncertainty in the fault model. The observer based fault tolerant control scheme provides exactly this attractive robustness property. The desired robustness to fault model uncertainty can be achieved by guaranteeing that the closed loop system remains stable for all open loop gains βLK, where β belongs to some chosen range (say [-0.7, 2]) depending on the level of confidence in the fault model.

3.4.2 Simulation results

The observer based fault tolerant control system was designed using the above scheme. In this subsection we present simulation results. We show simulation results only for the case of fault #3. Other situations also yield satisfactory results. (Experimental results pertaining to fault #2 are shown in the next subsection).

Fig. 3.8 and Fig. 3.9 show the results for the cases when the system "loses" the front and rear magnetometers respectively. During the event of the fault, the vehicle is on a curve of radius 800m. This is more serious than a fault occurring when the vehicle is on the straight section of the highway. Noise of about 2cm (RMS) (experienced in practice) has been added to the output of both the sensors.
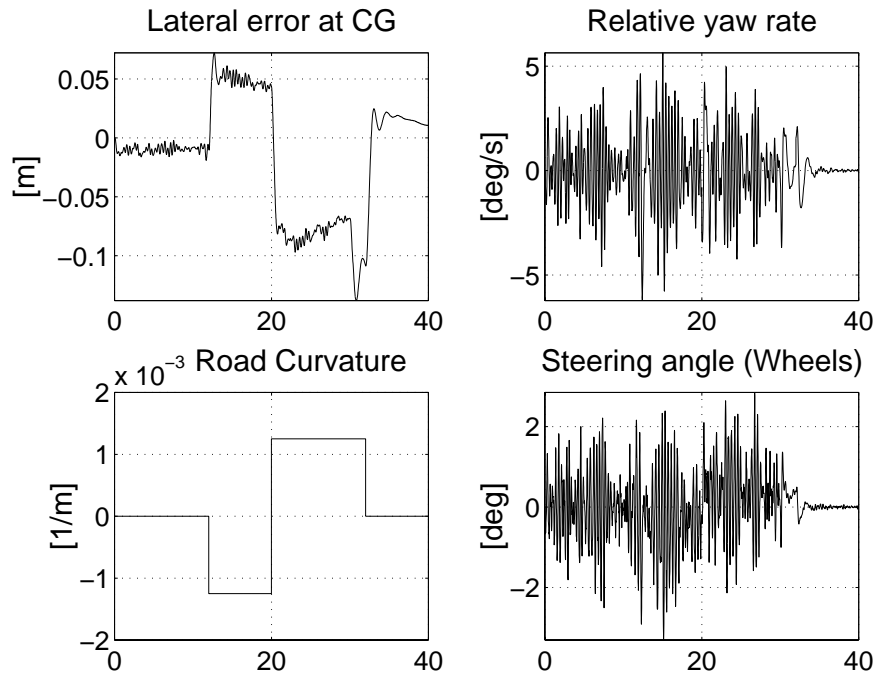
Figure 3.8: Simulation: Front magnetometer at t=30s for v=25m/s, d_s=4m

We observe in Fig. 3.8 and Fig. 3.9 that the lateral error is about 0.05m on a curve of radius 800m before the fault occurs (at t=30s). This is indeed a satisfactory level of performance during non-faulty operation when compared with experimental outputs as documented in et al (1996). However, when the fault occurs, since information is available only from one sensor, the maximum lateral error is less than 20cm(0.2m). Also the steering angle oscillations can be damped in practice by setting a saturation limit on the steering angle rate.
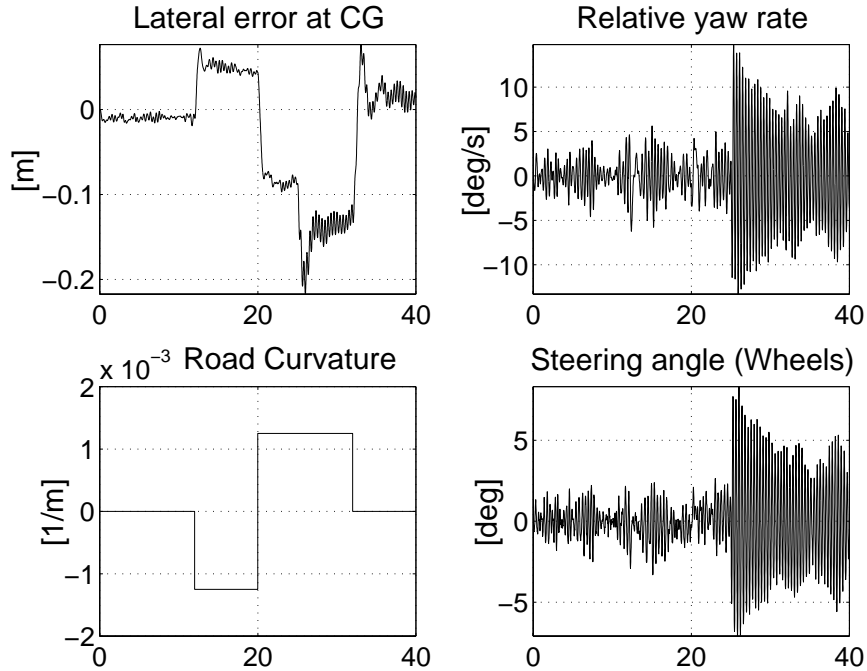
Figure 3.9: Simulation: Rear magnetometer at t=25s for v=25m/s, d_s=4m

Note : A gain scheduling technique can be used to choose the observer gains for different longitudinal velocities to achieve performance levels similar to those shown above.

3.5   Summary and Conclusions

This chapter presented the following:

1. Failures that the lane-keeping control system needs to be made insensitive.

2. Fault tolerant controller design based on simultaneous stabilization: It was shown that the problem of fault tolerant controller design may be formulated as a simultaneous stabilization problem. The design scheme for a simultaneously stabilizing controller that stabilizes the non-faulty plant and **one** faulty mode and which guarantees performance in the non-faulty mode was presented. The extension of this result to accommodate more faulty modes is currently underway.

3. Fault tolerant controller design based on the concept of observer based look-ahead: In the observer based look-ahead scheme, the controller processes an **estimate** of the lateral error at a location d_s ahead of the vehicle CG. The scheme was proposed to accommodate faulty conditions and at the same time maintain the benefits of large look-ahead distances.

We conclude the following from this research initiative.

1. It is possible to design practically realizable lane-keeping controllers that guarantee satisfactory performance even under certain faults that may occur during the operation of the lane-keeping control system.

2. Two schemes can be used to design such controllers.

   (a) Simultaneous stabilization based scheme
   (b) Observer based look-ahead based scheme

   The simultaneous stabilization based scheme is a convex optimization based design technique. It **guarantees** stability under chosen, well-modeled failures. However, the design problem is difficult to solve and may yield conservative controllers. In contrast, the observer based look-ahead scheme is a heuristic technique. No absolute **guarantees** of stability can be made when this scheme is used. Also, the scheme is difficult to implement in practice since the lateral dynamics change substantially for different longitudinal velocities. However, the scheme is very intuitive and yields good experimental results.

3. The realization of a fault tolerant lane-keeping control system must involve investigation into other design decisions such as appropriate placement of the magnetometers. The fault tolerance of the system can be greatly enhanced if the "rear" magnetometer set is placed in front of the rear-axle. This issue is being investigated as part of TO4205 (Fault Tolerant Lateral Control of Transit Buses and Trucks). We suggest that the "final" control system design configuration consist of two sets of magnetometers: one mounted under the front bumper of the vehicles and the other mounted about 2m behind the front set.

In summary, if the sensors are placed in the "correct" locations and the fault tolerant control algorithms are used, we can achieve highly precise and safe lane-keeping control action.

Chapter 4

Fault Diagnostic System for the Longitudinal Control System

This chapter will present the detailed design of the fault diagnostic system for the longitudinal controller using such model-based techniques. First, a brief description of the fault model used in the design will be presented in Section 4.1. Then the residual generator and residual processor will be describe in Sections 4.2 and 4.3, respectively. Finally, experimental results for the complete diagnostic system will be covered in Section 4.4.

4.1 Fault Modeling

Although several types of fault models exist in the literature, this project considers only faults in the system components which can be modeled as additive terms to the residual vector. More technically, let the set of residuals be defined by the vector $r \in \Re^n$. In the case of no faults and an exact model of the monitored system, the vector **r** would be exactly zero. However, the residual vector has nonzero components when sensor noise and modeling uncertainties are considered. This nonzero value of the residual vector under nominal conditions will be denoted $r_{nom} \in \Re^n$. The relationship between these vectors and the faults to be considered can be written in the form

$$r(t) = r_{nom}(t) + F\mu(t) \tag{4.1}$$

where the last term represents the effects of the different faults which the diagnostic system will attempt to detect. Each fault is represented by two parts: the *fault signature* matrix $F \in \Re^{nxp}$, whose columns describe the directional characteristics of the p faults, and the *fault mode* $\mu(t)$, which is a (possibly time-varying) vector describing the fault magnitude at time t. This project will only consider the occurrence of a single fault in the physical layer control components at any given time, thus restricting $\mu(t)$ to have only one nonzero element corresponding to the column of F which models the specific fault.

For the residual processor to correctly identify faults in the monitored system, the effect of each fault on the set of residuals must be unique. If this criteria is met, the faults are said to be *isolatable*. While this criteria theoretically guarantees that the identification of each fault is possible, the isolation of faults is generally not very robust to noise and unmodeled dynamics. A stronger condition can be achieved if the fault signatures $f \in Col(F)$ are linearly independent in the residual

space. Diagnostic systems which satisfy this condition are said to have *structured* or *directional* *residuals* (org., n.d.).

4.2 Residual Generator

The residual generator relies on ten sensors, inter-vehicle communication, and the throttle and brake actuator commands to form a residual vector which is sensitive to faults in all of the vehicle's sensors and actuators. The specific components which are monitored by this system include the magnetometer and the components listed in Table 2.2. Although the magnetometer is not directly used in the longitudinal controller, it must also be monitored because the magnetometer is used in the fault diagnostic system. Diagnosis of faults in the communications system are beyond the scope of this project, however several other PATH projects are addressing this issue ().

In addition to this raw information about the vehicle's condition, several observers have been designed to provide analytical redundancy for the physical components. An interesting characteristic of the hierarchical structure of the longitudinal control system is that the diagnostics can effectively be decoupled between those components involved in the regulation layer and the physical layer control laws. This allows for a compartmentalized design of the diagnostics for each level of control. The remaining parts of this section will discuss the separate residuals that compose the residual vector, as well as the specific state observers used.

4.2.1 Inter-vehicle spacing residuals

If the physical layer is operating correctly, then the use of the dynamic surface controller results in an overall linear vehicle model as seen by the regulation layer. By rearranging terms in the follower control law presented in Chapter 2, the resultant vehicle model is as follows:

$$\ddot{\delta}(t) + 2\zeta\omega_m\dot{\delta}(t) + \omega_m^2\hat{\delta}(t) = \omega_m^2 u(t)$$

where $\delta(t)$ is the current range to the previous vehicle in the platoon, $u(t) = \delta_{des}$ is a known input to the linearized vehicle dynamics, and the constants ζ and ω_m are chosen controller gains. Note that the follower control law uses a simple first order observer is used to estimate the range $\hat{\delta}(t)$ to improve the quality of the range measurement. The observer has the following form;

$$\dot{\hat{\delta}}(t) = \dot{\delta}(t) + k_1(\delta(t) - \hat{\delta}(t))$$

where k_1 is the observer gain chosen to make the error dynamics stable. The observer is included in the linear vehicle model because the time constant of the observer is within the same order of magnitude of the follower control law, and thus has a significant impact on the vehicle dynamics.

By combining the follower control law and the observer dynamics, the SISO system can be rewritten in the following state space form as:

$$\dot{x} = \begin{bmatrix} 0 & 1 & 0 \\ 0 & -2\zeta\omega_m & -\omega_m^2 \\ k_1 & 1 & -k_1 \end{bmatrix} x + \begin{bmatrix} 0 \\ \omega_m^2 \\ 0 \end{bmatrix} u \qquad (4.2)$$

36

where the state is defined as $x = \begin{bmatrix} \delta & \dot{\delta} & \hat{\delta} \end{bmatrix}^T$. In addition, this system is observable from the radar range, accelerometer, magnetometer and wheel speed sensor measurements independently. Therefore, the four possible measurement equations can be written as,

$$y_\delta = \begin{bmatrix} 1 & 0 & 0 \end{bmatrix} x \tag{4.3}$$

$$y_{n_{mag}} = \begin{bmatrix} -1 & 0 & 0 \end{bmatrix} x + (n_{mag,prev} - L) \tag{4.4}$$

$$y_{\omega_w} = \begin{bmatrix} 0 & -1 & 0 \end{bmatrix} x + v_{prev} \tag{4.5}$$

$$y_a = \begin{bmatrix} 0 & 2\zeta\omega_m & \omega_m^2 \end{bmatrix} x + a_{prev} \tag{4.6}$$

where L is the vehicle length, $n_{mag,prev}$, v_{prev} and a_{prev} are known via inter-vehicle communication, and thus can be viewed as additional inputs.

Four *dedicated observers* were constructed to estimate the inter-vehicle range using the linear model described above. A dedicated observer uses only one of the available sensors to estimate the entire state vector. This setup is quite attractive for use in fault diagnostics, because ideally only one of the observer estimates would be affected by a specific fault in the sensors, thus allowing for the diagnosis of multiple faults (org., n.d.). These four observers have the following form,

$$\dot{\hat{x}} = \begin{bmatrix} 0 & 1 & 0 \\ 0 & -2\zeta\omega_m & -\omega_m^2 \\ k_1 & 1 & -k_1 \end{bmatrix} \hat{x} + \begin{bmatrix} 0 \\ \omega_m^2 \\ 0 \end{bmatrix} u + K_i(y_i - C_i\hat{x}) \tag{4.7}$$

$$\hat{\delta}_i = \begin{bmatrix} 1 & 0 & 0 \end{bmatrix} \hat{x} \tag{4.8}$$

where i indicates the specific sensor used for the correction term, i.e. $n_{mag}, \omega_w, \delta$ or a. The observer gain matrices K_I are chosen via a Luenberger design procedure (Brogan, 1991). The range estimates of these four observers are then used to form the first six elements of the residual vector as follows

$$
\begin{aligned}
r_1 &= \hat{\delta}_\delta - \hat{\delta}_{n_{mag}} \\
r_2 &= \hat{\delta}_\delta - \hat{\delta}_{\omega_w} \\
r_3 &= \hat{\delta}_\delta - \hat{\delta}_a \\
r_4 &= \hat{\delta}_{n_{mag}} - \hat{\delta}_{\omega_w} \\
r_5 &= \hat{\delta}_{n_{mag}} - \hat{\delta}_a \\
r_6 &= \hat{\delta}_{\omega_w} - \hat{\delta}_a
\end{aligned}
$$

4.2.2 Command signal residuals

The next three residuals are simple parity equations that compare the commanded throttle, brake pressure, and acceleration to the appropriate sensor measurements. These residuals are written as

$$
\begin{aligned}
r_7 &= a - u_{isl} \\
r_8 &= \alpha - \alpha_c \\
r_9 &= P_{wheel} - P_{mcc}
\end{aligned}
$$

37

4.2.3 Engine dynamics residuals

The last three residuals are used to diagnose faults in the sensors and actuators involved the physical layer control laws based on the nonlinear vehicle model presented in Chapter 2. First, two second order nonlinear observers are proposed to estimate both the engine speed and mass of air from engine speed measurements using the methodology developed in the attached paper (Howell, 2002) and the nonlinear vehicle model used for the longitudinal controller design. Both observers use the engine speed measurement for the correction term, while one observer uses the throttle and brake pressure sensors as inputs and the other uses the actuator commands. The first observer has the form

$$\dot{\hat{\omega}}_e = \frac{1}{J_e}(T_{net}(\hat{\omega}_e, \hat{m}_a) - c_x R^{*3} h^3 \hat{\omega}_e^2 - R^* T_{rr} - R^* T_{br}(P_{wheel})) + K_{s1}(\omega_e - \hat{\omega}_e)$$

$$\dot{\hat{m}}_a = MAX\,TC(\alpha)\,PRI(\hat{m}_a) - \dot{m}_{ao}(\hat{\omega}_e, \hat{m}_a) + K_{s2}(\omega_e - \hat{\omega}_e)$$

while the second observer can be written as

$$\dot{\hat{\omega}}_e = \frac{1}{J_e}(T_{net}(\hat{\omega}_e, \hat{m}_a) - c_x R^{*3} h^3 \hat{\omega}_e^2 - R^* T_{rr} - R^* T_{br}(P_{mcc})) + K_{c1}(\omega_e - \hat{\omega}_e)$$

$$\dot{\hat{m}}_a = MAX\,TC(\alpha_c)\,PRI(\hat{m}_a) - \dot{m}_{ao}(\hat{\omega}_e, \hat{m}_a) + K_{c2}(\omega_e - \hat{\omega}_e)$$

Finally, under the assumption that the torque converter is locked, then the engine speed and wheel speed are linearly related via the current gear ratio as

$$\omega_w = R^* \omega_e$$

This relationship can be used to form a simple parity equation comparing the engine and wheel speed measurements.

The residuals for the two observers and speed parity equation form the last three elements in the residual vector, specified as

$$r_8 = \frac{V_{man}}{R_{air} T_{man}} P_{man} - \hat{m}_a(\omega_e, P_{wheel}, \alpha)$$

$$r_9 = \frac{V_{man}}{R_{air} T_{man}} P_{man} - \hat{m}_a(\omega_e, P_{mcc}, \alpha_c)$$

$$r_{10} = \omega_w - R^* \omega_e$$

It is important to note that although the observer residuals will be nonlinearly related to the sensor measurements and actuator commands, the linear fault model given in Equation 4.1 is still applicable since the residuals can be shown to remain close to a linear system using the same argument as in (Garg, 1995).

4.3 Residual Processor

For the diagnostics of the longitudinal control system, a combination of weighted least squares estimation and thresholding is used to detect and identify faults. A more complex residual processing scheme based on fuzzy logic was previously pursued, however this residual processing technique

was not chosen because it's increased computational complexity made it impractical for real-time implementation (Howell and Hedrick, 1999).

The first part of the residual processor provides a weighted linear least squares estimate of the fault mode vector. Next, each element of the estimate is compared to a threshold, and a fault is declared when one or more thresholds are crossed. Finally, classical logic is used to identify the faulty component based on the thresholds that are crossed. Each of these tasks will now be addressed in more detail.

4.3.1 Estimation of the fault mode vector via weighted least squares estimation

The first task performed by the residual processor is to estimate the magnitude of the fault mode vector using the current value of the residual vector. This estimation of the fault mode is quite useful for both fault diagnosis and fault management. In terms of fault diagnostics, the resulting estimate has a very intuitive relationship with the system dynamics and simplifies the choice of thresholds for fault detection. A fault management system could also potentially benefit from the estimate by choosing different methods of reconfiguration based on both the type of fault and it's magnitude.

Using the fault model described in Equation 4.1, the residual and fault mode vectors are related by the linear matrix equation

$$r(t) - r_{nom} = F\mu(t)$$

where r_{nom} is assumed to be constant with respect to time for simplicity. A weighted least squares solution for $\mu(t)$ can now be performed, where the residual vector is weighted by the matrix $W^{-\frac{1}{2}}$ to reduce scaling problems. The resulting estimate $\mu_{ls}(t)$ can be calculated by the following equation

$$\mu_{ls}(t) = F^\dagger(\mathbf{r}(t) - \mathbf{r}_{nom})$$

where $F^\dagger = (F^T W^{-1} F)^{-1} F^T W^{-1}$ is the weighted pseudo-inverse of F. Notice that $F^\dagger$ and $\mathbf{r}_{nom}$ can be determined a priori, so that only a vector addition and a matrix multiplication are required to calculate the estimate given the residual vector.

4.3.2 Thresholding and decision logic

The final task of the residual processor involves the choice of an appropriate threshold for each element of the fault mode vector, and the identification of the faulty component based on the thresholds exceeded. If the residual generator had structured residuals, then each fault would affect only one element of the fault mode estimate vector. The detection of a fault would then be a simple matter of choosing a threshold for each estimate element, and declaring a fault when one of the thresholds was exceeded. Identification would also be trivial, since the exceeded threshold would determine the component with the fault.

Unfortunately, the residual generator for the longitudinal controller is only isolatable, which makes identification slightly more complicated. The isolatability property only guarantees uniqueness of the fault signatures, however some signatures may be linear combinations of others. The qualitative effects of each fault on the fault mode estimate have been summarized in Table 4.1, where H represents a "high" or a large increase in the estimate element, M represents a "medium"

39

or moderate increase in the estimate element, and L represents a "low" or no increase in the particular estimate element. The table shows that although many of the faults cause several elements to increase, they each have a unique effect on the fault mode vector. Since only single faults are being considered, the each fault can be uniquely identified by the pattern of increased elements. Furthermore, the processing of the residual vector can effectively be decoupled between the sensors monitored using the inter-vehicle spacing and the sensors and actuators monitored via the nonlinear engine dynamics. For simplicity in the remaining sections of the chapter, these two groups will be termed the regulation and physical layer control components, respectively.

Table 4.1: Fault mode vector estimate μ_{l_s} under component faults

Faulty Sensor / Actuator	μ_1	μ_2	μ_3	μ_4	μ_5	μ_6	μ_7	μ_8	μ_9	μ_{10}
radar	H	M	M	M	L	L	L	L	L	L
magnetometer	M	H	M	M	L	L	L	L	L	L
wheel speed sensor	M	M	H	M	M	L	L	L	L	L
accelerometer	M	M	M	H	L	L	L	L	L	L
engine speed sensor	L	L	M	L	H	M	M	M	M	M
manifold pressure sensor	L	L	L	L	M	H	M	M	M	M
throttle angle sensor	L	L	L	L	M	M	H	M	M	M
throttle actuator	L	L	L	L	M	M	M	H	M	M
brake pressure sensor	L	L	L	L	M	M	M	M	H	M
brake actuator	L	L	L	L	M	M	M	M	M	H

4.4 Experimental Results

The fault diagnostic system presented in the previous two sections was implemented in the C programming language as an addition to the longitudinal control software developed for the 1997 NAHSC Demonstration (Staff, 1998). This longitudinal control code has been extensively tested and used by PATH, and provided much of the underlying software structure needed by the diagnostic system, such as access to the publish-subscribe database and the command inputs calculated by the controller.

The fault diagnostic code was tested under two scenarios; low-speed real-time tests on a single car at Richmond Field Station (RFS) and emulation using data from both low and high-speed tests on a platoon of three vehicles on I-15 in San Diego. This section will focus on results using the data from I-15, since the single-vehicle tests at RFS were used primarily to debug and verify the timing latencies of the additional fault diagnostic software.

The experimental tests conducted on I-15 used a platoon of three Buick LeSabre, where the lead vehicle followed a desired velocity profile and the two following vehicles attempted to maintain a constant distance from the preceding vehicle. For the experimental data shown in this report, the cruise speed was set to 60 mph with a desired spacing of 12 meters. To simplify the testing procedure, no additional maneuvers were performed during any of the tests.

To eliminate the need for hardware modifications, the occurrence of faults in the control components were simulated in the longitudinal control software during the experimental runs. For example,

sensor faults were simulated by adding a time-varying bias to the sensor reading before the control calculations were performed. Similarly, actuator faults were simulated by adding a time-varying bias to the actuator command after the control calculations were performed. The remainder of this section will demonstrate the performance of the implemented diagnostic system under both normal and faulty conditions.

4.4.1 Performance under no fault scenario

The performance of the longitudinal controller and diagnostic system when no faults are present is shown in Figs. 4.1 through 4.7. The first two figures demonstrate that the existing longitudinal controller provides excellent velocity and inter-vehicle distance tracking over the entire run. However, it should be noted that even under nominal conditions the controller can only track the desired spacing to within about 1 meter. This is primarily due to the unmodeled gravitational force caused by a steep dip at the end of the I-15 test track, as can be seen in Fig. 4.2 around 250 to 300 seconds. Naturally, this limits the sensitivity of the diagnostic system with respect to faults in the regulation layer control components.
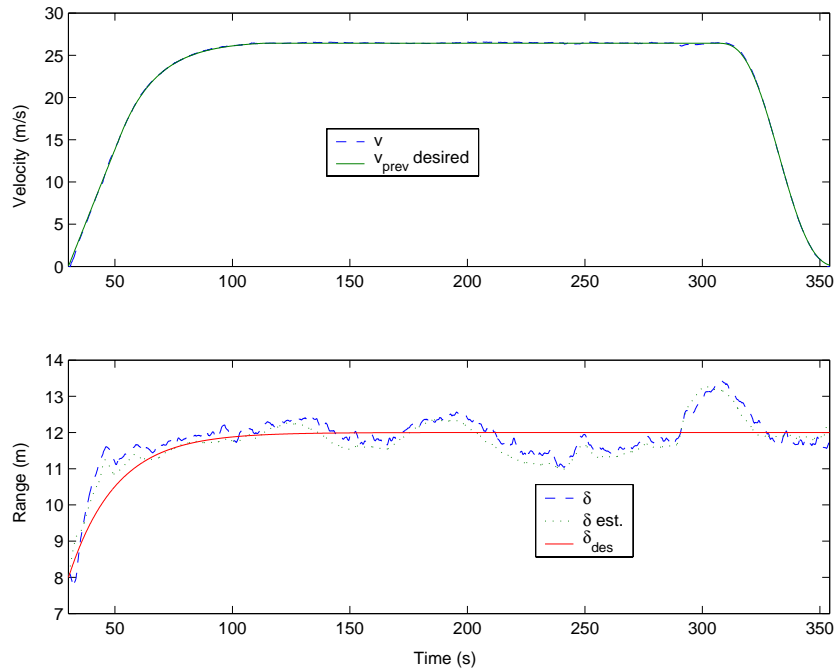
Figure 4.1: Controller performance in tracking velocity (top) and range (bottom)

Next, Figs. 4.3 through 4.5 show the estimation performance of the linear and nonlinear observers used in the residual generator. Obviously, all of the estimates converge to their true values, however the effects of unmodeled dynamics is apparent in both sets of observers. First, the previously mentioned effects of grade noticeable affect the performance of the inter-vehicle range observers from 250 to 300 seconds into the run. To avoid false alarms due to this unmodeled force, the thresholds for the fault estimates of the regulation layer components were limited to detect changes larger than 1.2 meters.
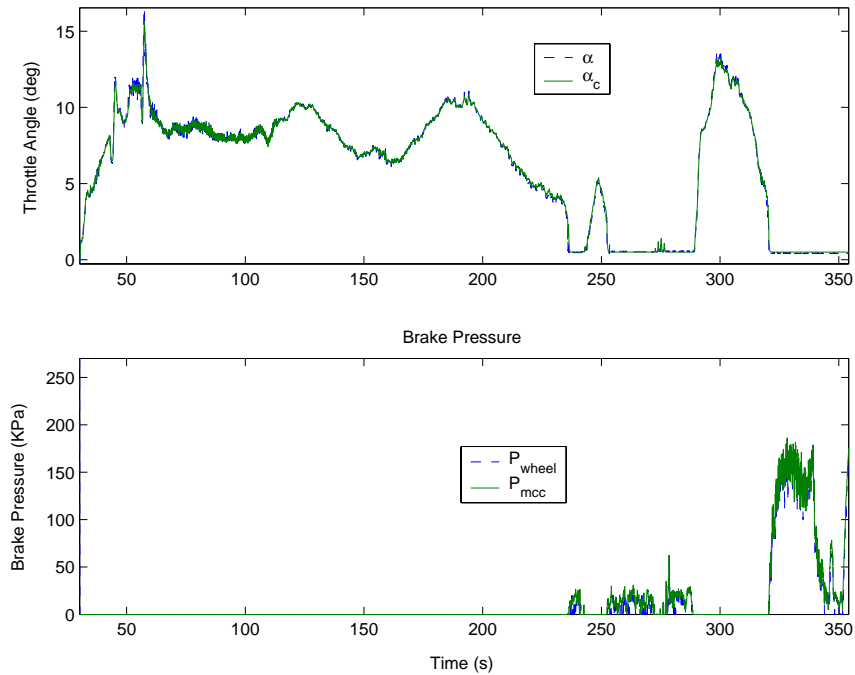
Figure 4.2: Commanded and measured control effort used in a normal run

The diagnostics related to the physical layer components are also limited by unmodeled behavior of the vehicle due to the following four causes:

1. Grade also has an indirect effect upon the engine dynamics as well, in that as the vehicles travel downhill less engine torque is required because of the additional gravitational force. This causes the longitudinal controller to switch to brake control, while the engine's power-train control module (PCM) unlocks the torque converter and forces the engine to idle. Unfortunately, this combination of events effectively decouples the measured vehicle and engine speeds which nullifies the validity of the vehicle model used.

2. The throttle actuator is bypassed when the engine is at idle, and a separate idle air control valve (IAC) is used for control. (Gen, 1997).

3. Discrete changes in operating mode, i.e. gear shifts and switching between throttle and brake control, have a severe impact on both the longitudinal controller and the diagnostic system.

Naturally, the fault diagnostic systems capabilities are limited when the engine is idling or switching between operating modes. When the engine is idling, faults in the physical layer control components can be detected, but they can only be isolated into two groups; those occurring in the brakes or those occurring in the throttle control. To compensate for changes in operating mode, the residual processor is turned off for approximately 5 seconds after the change to allow for the observers to converge to the new state. While these modifications seem very restrictive, these limitations are expected due to the model simplifications, and fault diagnostic system otherwise performs very well as seen in the next two subsections.

Finally, the magnitudes of the fault mode estimates computed by the residual processor for both the regulation physical layer components are shown in Figs. 4.6 and 4.7. These estimates have
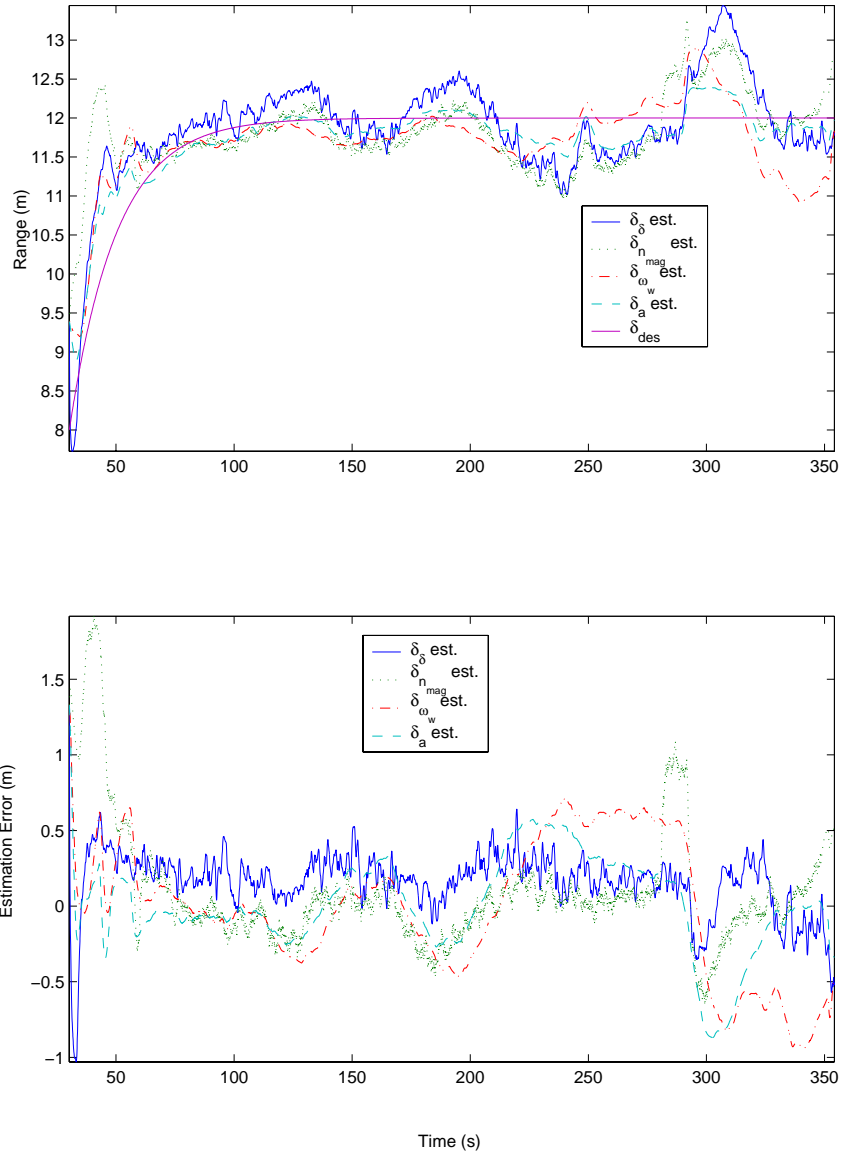
Figure 4.3: Diagnostic system range estimates (top) and estimation errors (bottom) during a normal run
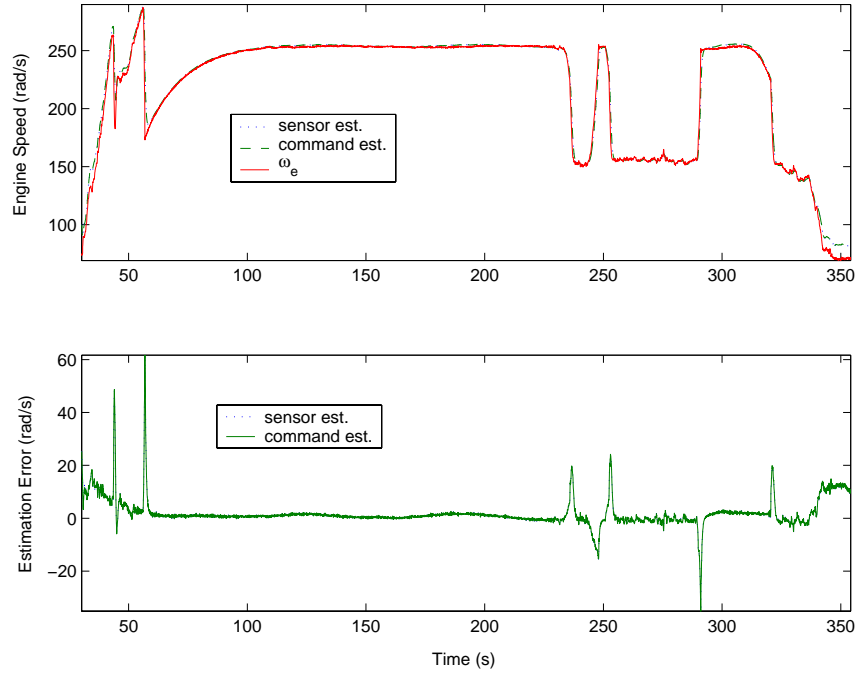
Figure 4.4: Diagnostic system engine speed estimates(top) and estimation errors (bottom) during a normal run
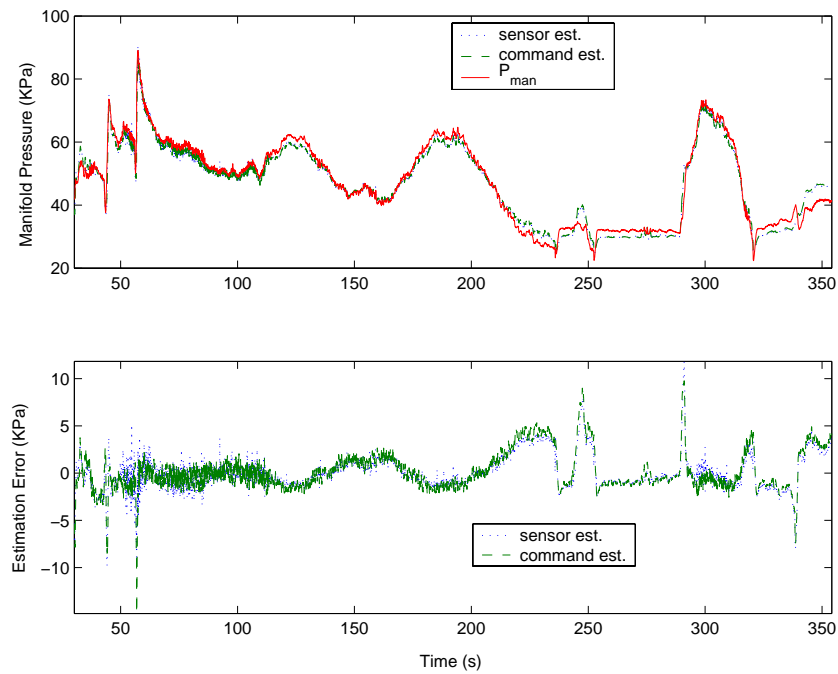
Figure 4.5: Diagnostic system manifold pressure estimates (top) and estimation errors (bottom) during a normal run

been normalized by their thresholds for clarity in comparing their sensitivity to the various faults presented in the next section. From both figures, it can be seen that the estimates remain well below their thresholds, shown by the dashed lines, except for a few points at the beginning of the run. These false alarms occur during the period when the observers are converging to the true values, and are thus ignored by the residual processor. It is also quite noticeable where the residual processor is disabled, i.e. the fault mode estimates are set to zero, due to engine idling and switches in operating mode.
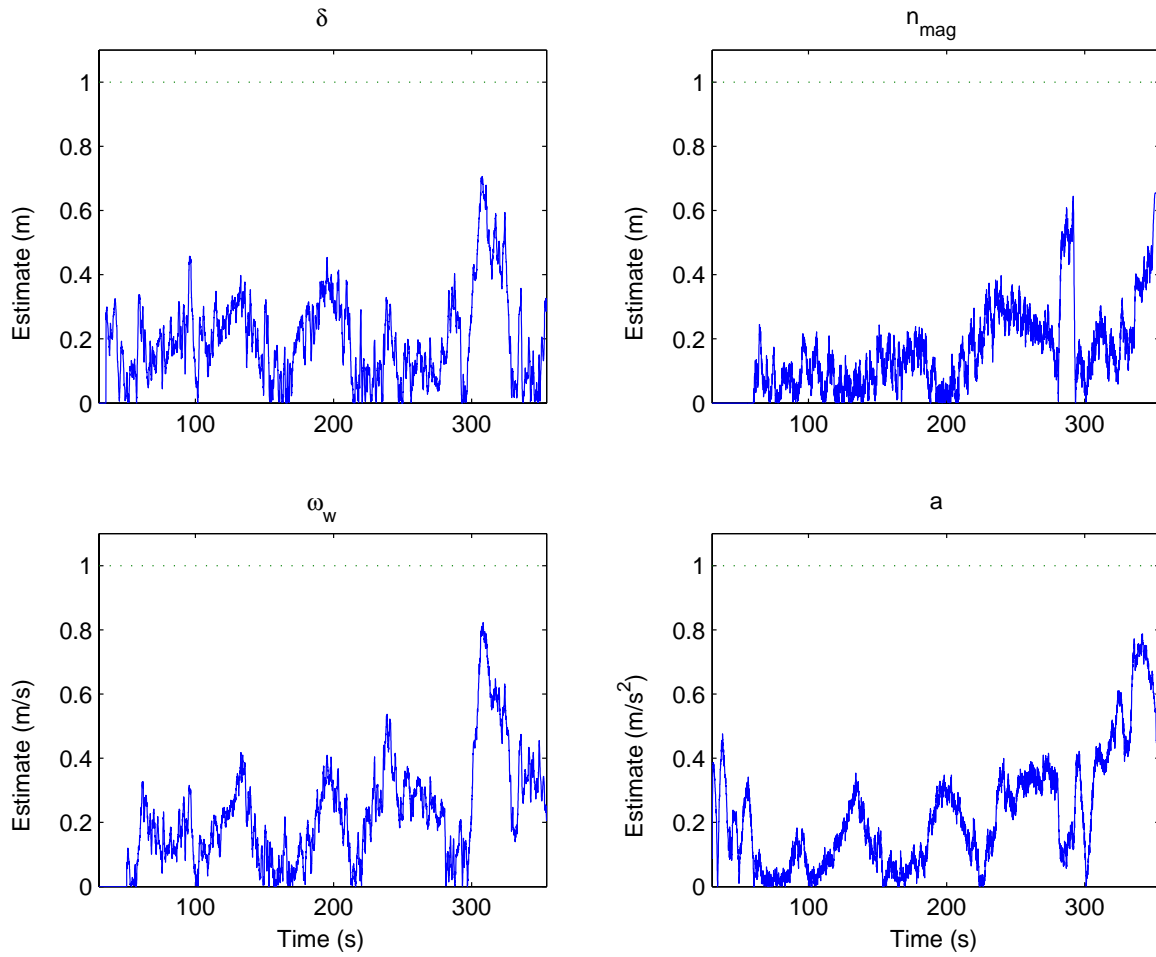
Figure 4.6: Diagnostic system normalized fault mode estimates for the regulation layer components
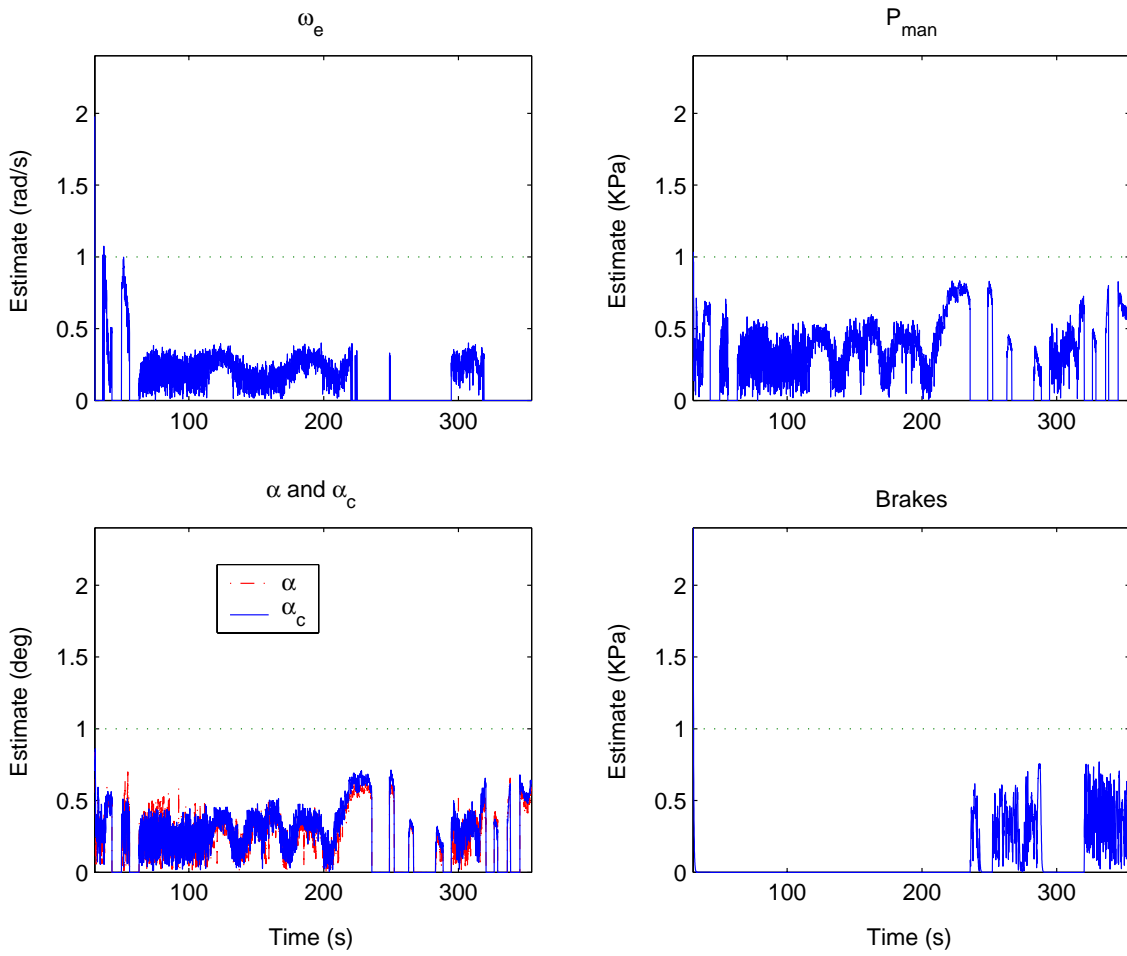
Figure 4.7: Diagnostic system normalized fault mode estimates for the physical layer components

4.4.2 Performance under faults in the physical layer control components

The next group of figures show experimental results for faults in the physical layer control components using the same testing scenario as in the previous sections. The diagnostic system performs extremely well at detecting, identifying, and correctly estimating the fault magnitudes for faults in the engine speed sensor, throttle angle sensor, throttle actuator, and braking system. Of course, this is subject to the limitations discussed in Section 4.4.1. Faults in the manifold pressure sensor are also readily detected and identified, as seen in Figs. 4.10 and 4.11, however the estimation of the fault magnitude is not as accurate. This is most likely caused by the approximation of a linear relationship between the residuals and faults, but the estimate appears accurate enough to get a first order approximation of the fault for use in control reconfiguration by the fault management system.
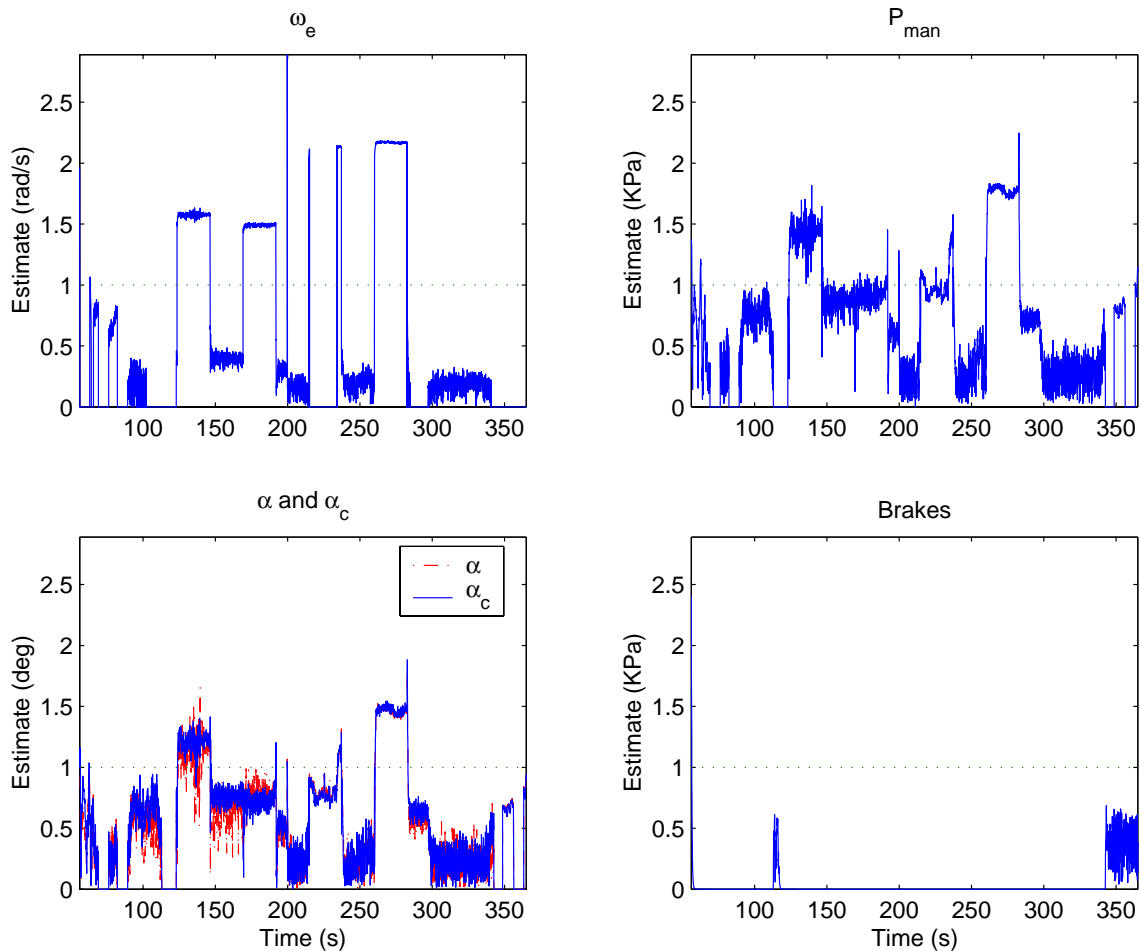
Figure 4.8: Diagnostic system normalized fault mode estimates under an engine speed sensor fault

4.5 Conclusions

This chapter showed the development of the fault diagnostic system for the longitudinal control system and it's two primary components; the residual generator and the residual processor. The residual
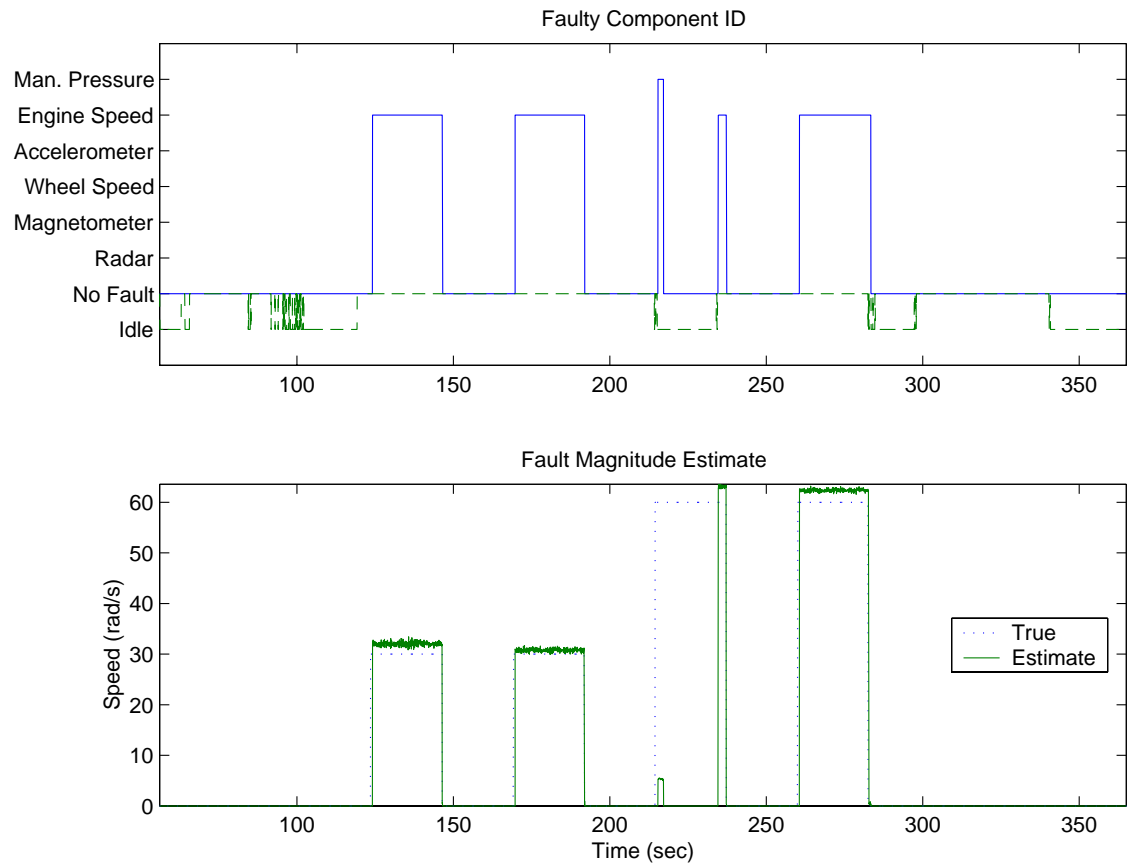
Figure 4.9: Fault identified (top) and fault mode estimate (bottom) under an engine speed sensor fault
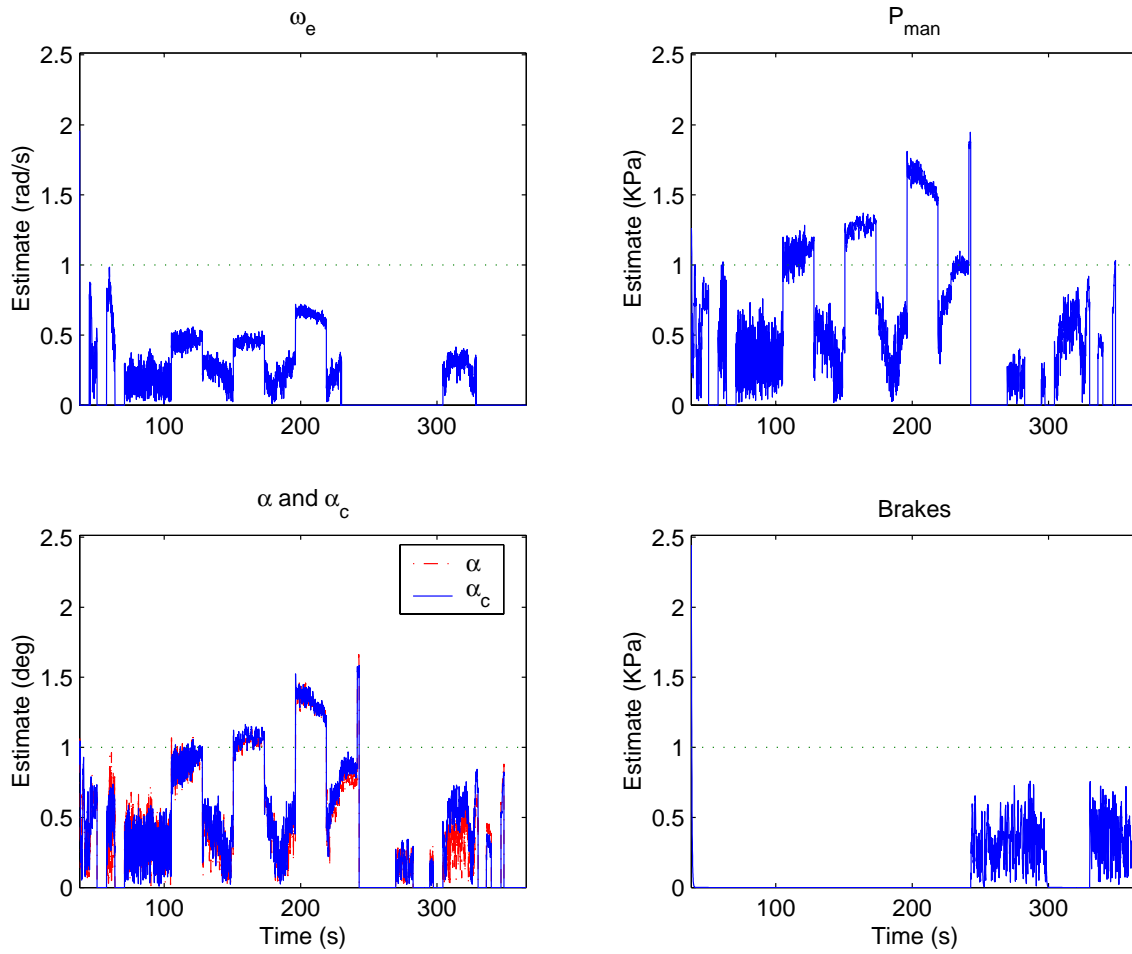
Figure 4.10: Diagnostic system normalized fault mode estimates under a manifold pressure sensor fault
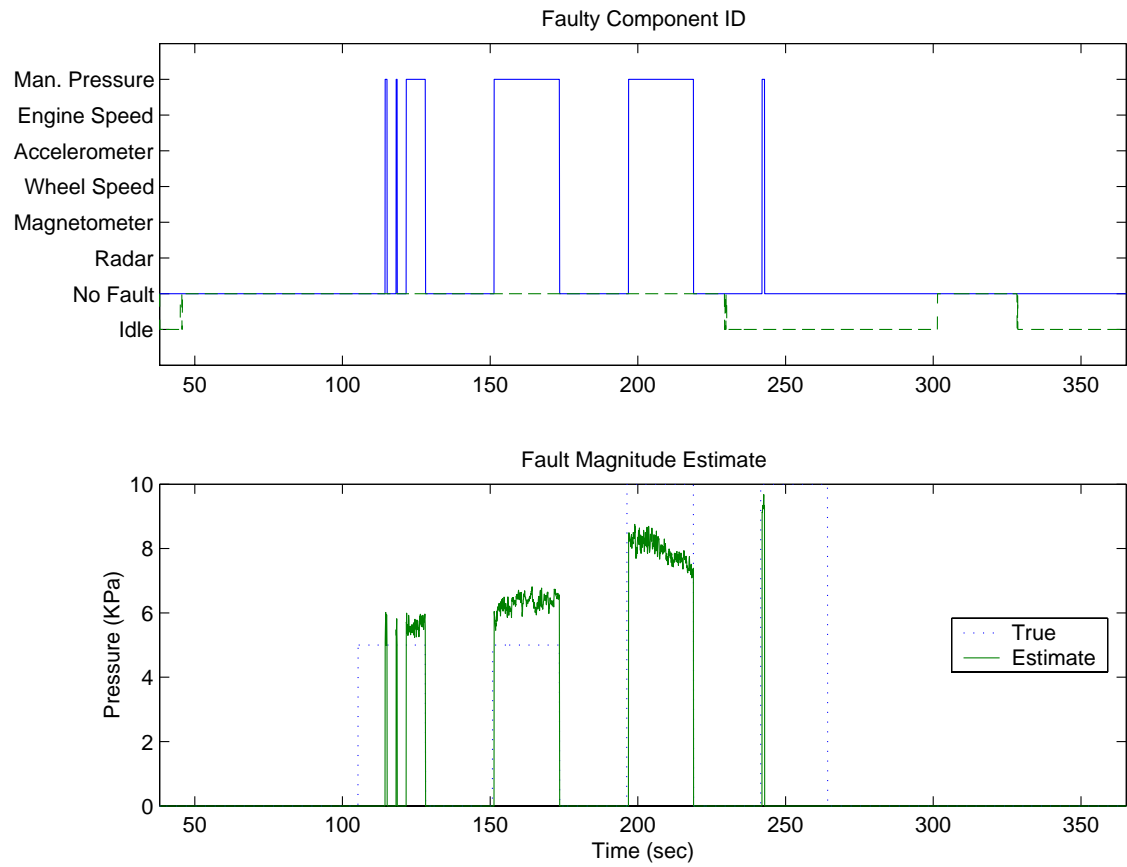
Figure 4.11: Fault identified (top) and fault mode estimate (bottom) under a manifold pressure sensor fault
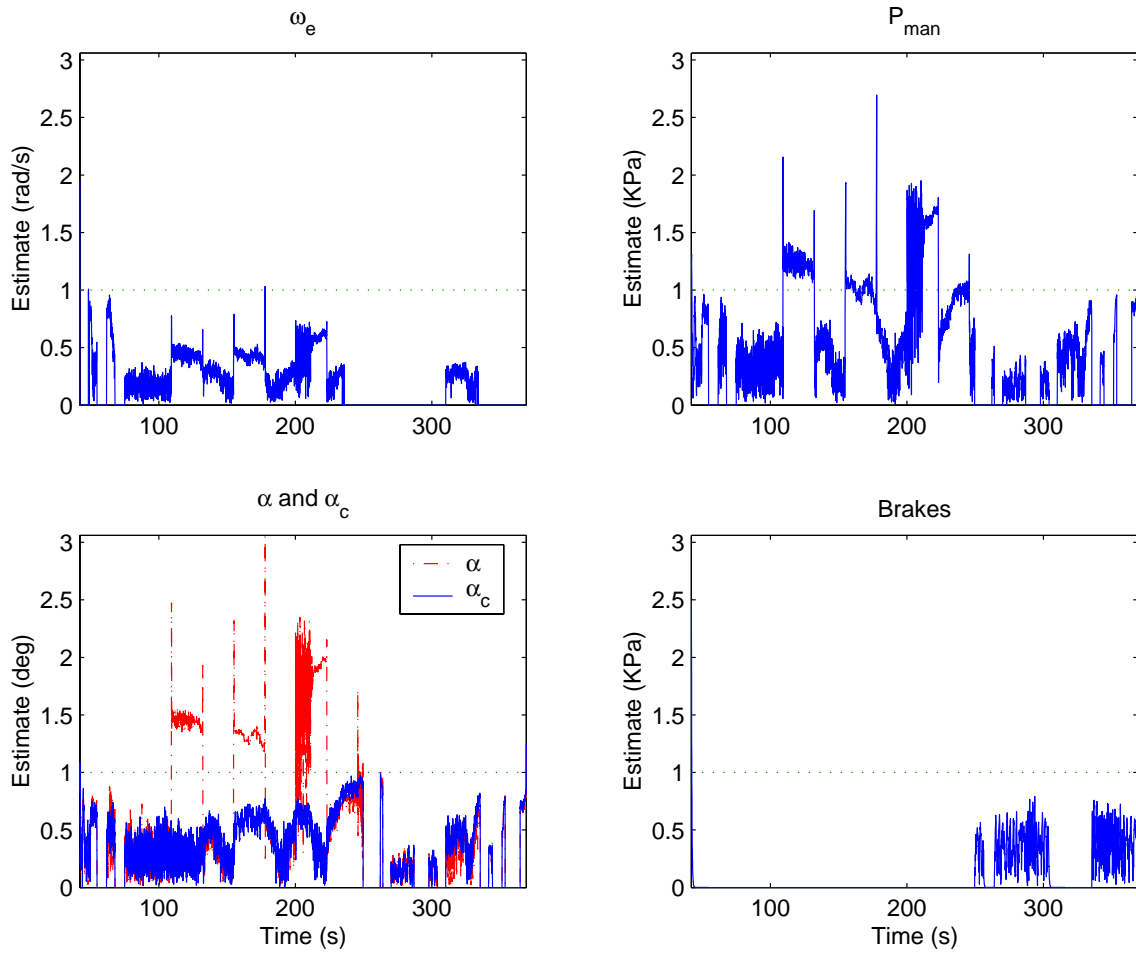
Figure 4.12: Diagnostic system normalized fault mode estimates under a throttle angle sensor fault
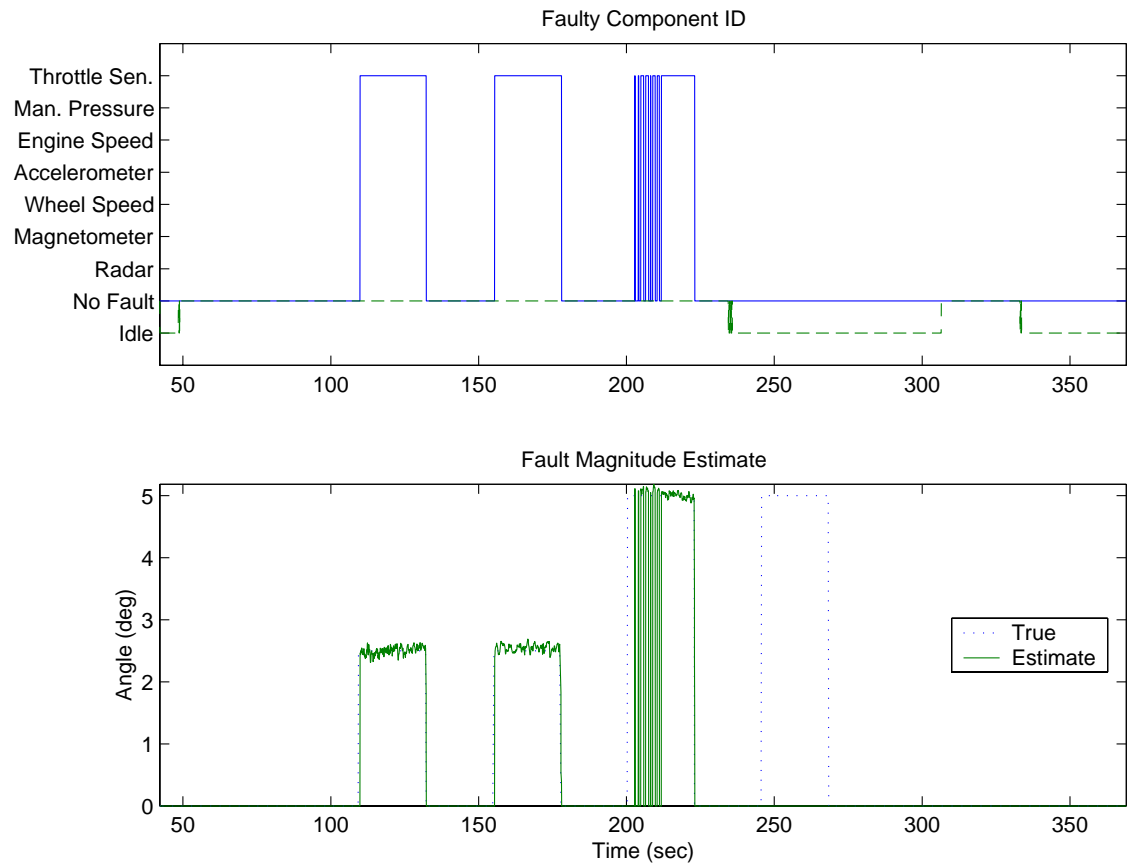
Figure 4.13: Fault identified (top) and fault mode estimate (bottom) under a throttle angle sensor fault
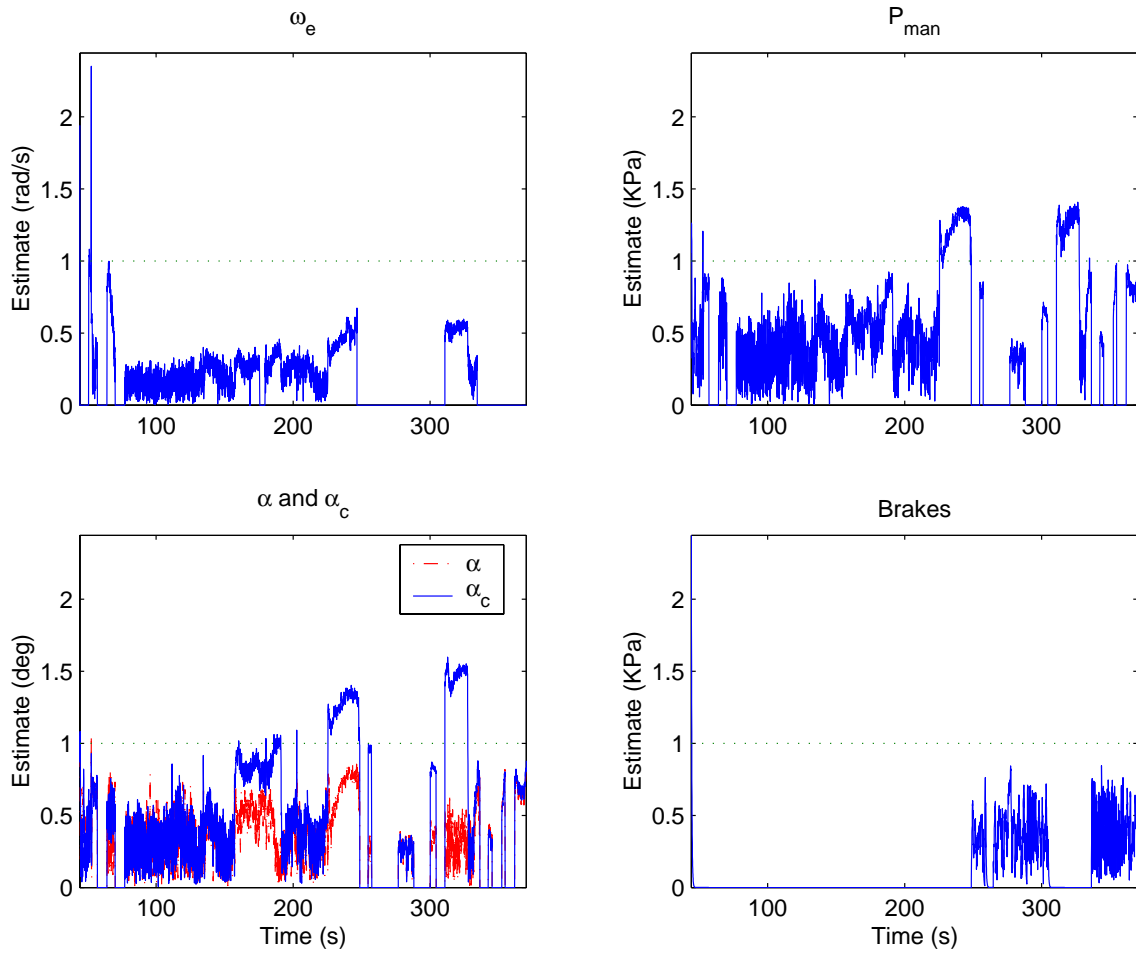
Figure 4.14: Diagnostic system normalized fault mode estimates under a throttle actuator fault
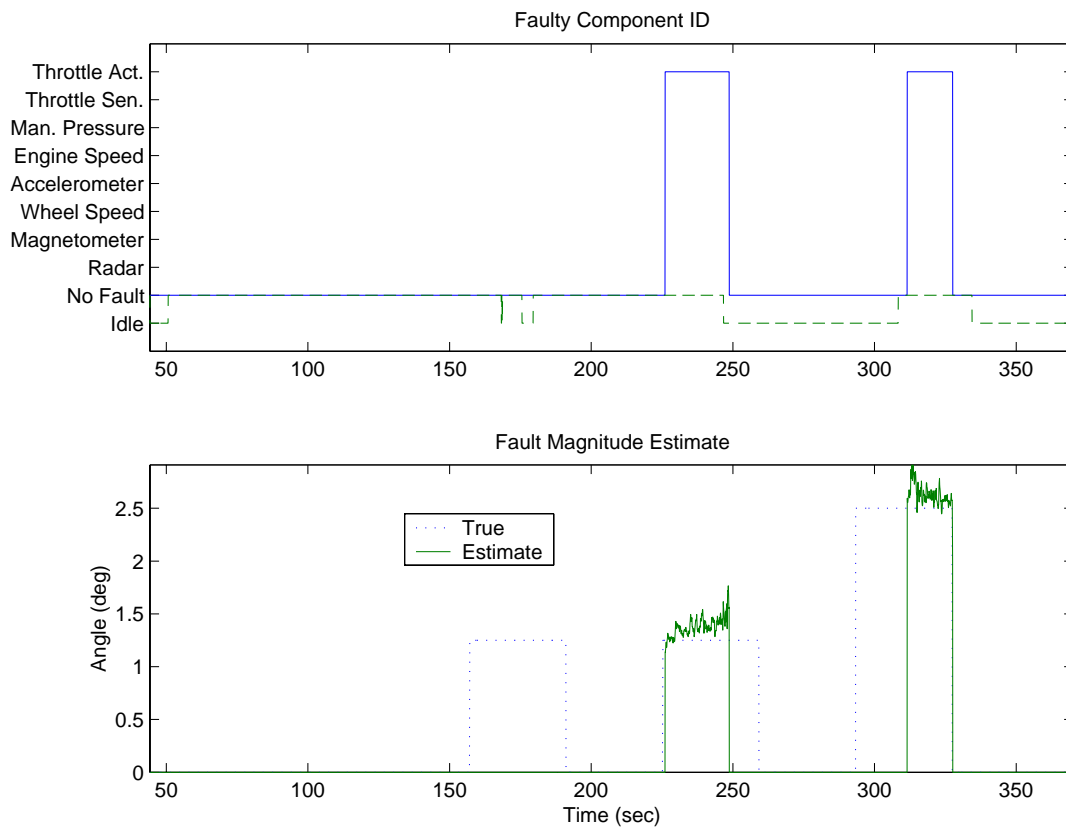
Figure 4.15: Fault identified (top) and fault mode estimate (bottom) under a throttle actuator fault
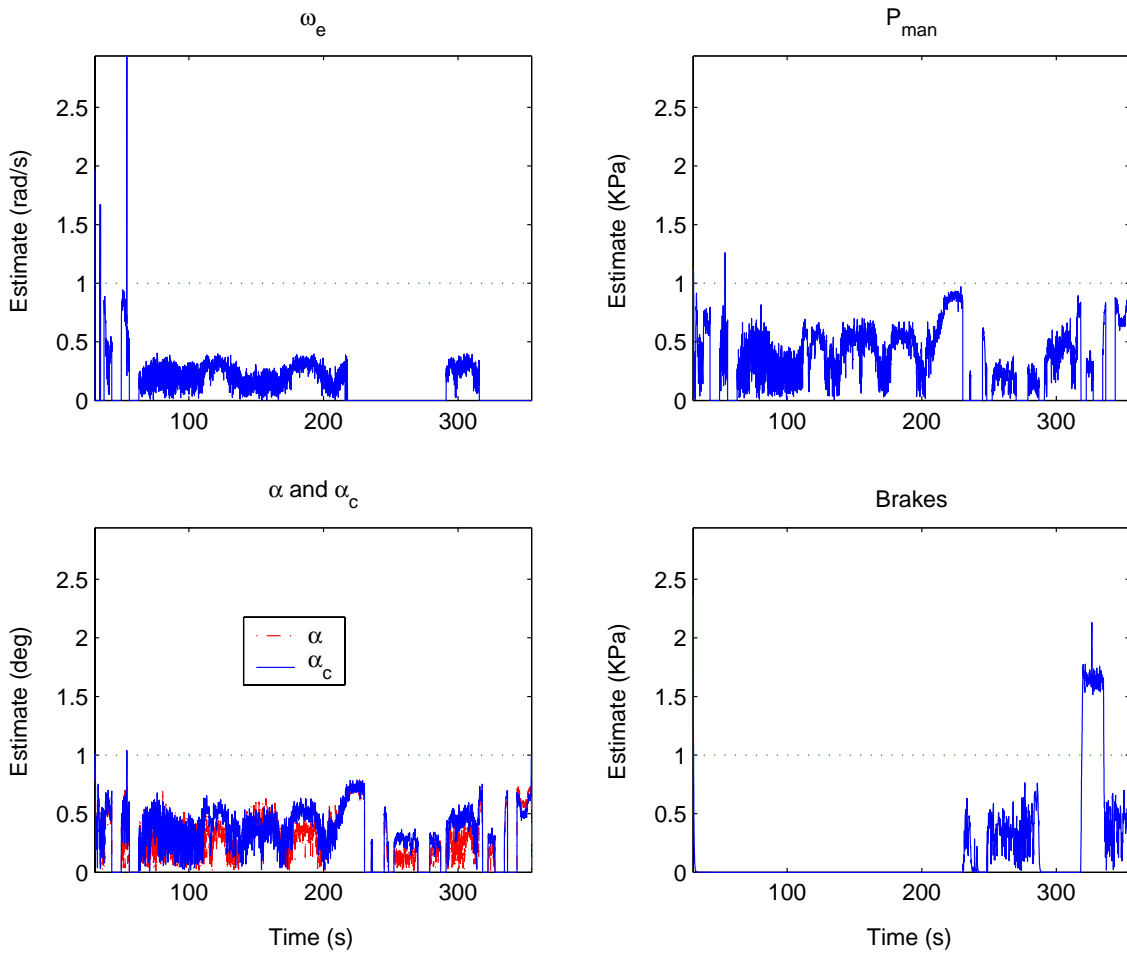
Figure 4.16: Diagnostic system normalized fault mode estimates under a brake system fault
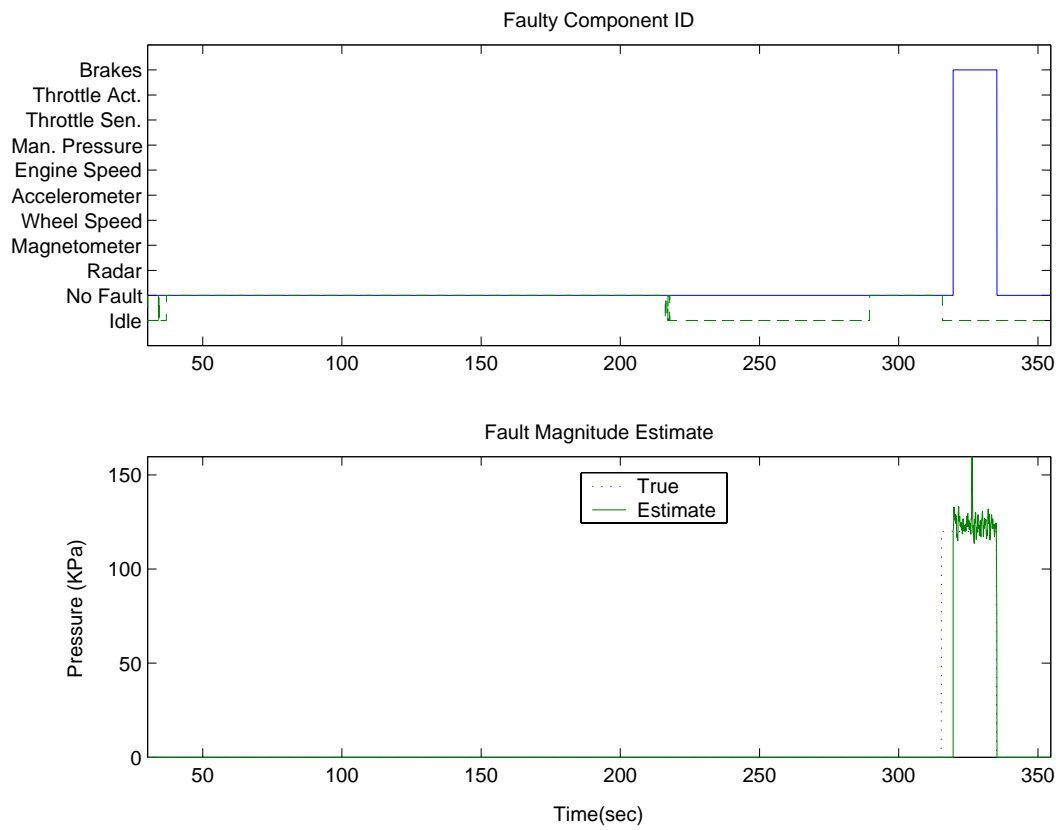
Figure 4.17: Fault identified (top) and fault mode estimate (bottom) under a brake system fault

generator used the inherent analytical redundancy of the vehicle model to design a set of residual signals sensitive to faults in the longitudinal control components. The residual processor monitors these residuals to determine when a fault has occurred, identifies the faulty component, and provides a least squares estimate of the fault magnitude. The complete system has been experimentally implemented and shown to provide exceptional performance under conditions limited by the quality of the underlying model. Further research into improving the vehicle model at idle and the diagnostic system's robustness to switched modes of operation is ongoing.

Chapter 5

Soft Fault Diagnostics and Handling — Tire/Road Friction Estimations and Emergency Braking Control

In the previous chapter, we discussed "hard" fault diagnostics and management in the regulation and coordination layers. In the rest of this report, we will focus on the "soft" fault diagnostics and management. The most important "soft" fault that we consider here is the vehicle deceleration and acceleration capabilities. It has been shown that spacing policies, in both independent vehicle and platooning scenarios, need to be related to the maximum acceleration and braking capabilities of neighboring vehicles (Alvarez, 1996). These capabilities, in turn, depend primarily on the forces of contact between tires and ground. In this chapter, we give an introduction to tire/road friction characteristics and review the literature on this topic. Then, we discuss the tire/road friction estimation approach in this report.

5.1   Background

5.1.1   Tire forces and moments

Tire/road interaction is very important for vehicle dynamics and control. Fig. 5.1 illustrates the tire/road interactions and Fig. 5.2 shows a SAE [1] standard representation of forces and moments generated by the tire/road interactions. In a general case, three forces, the longitudinal traction/braking force F_x, lateral force F_y, and vertical (normal) force F_z, and three moments, the overturning moment M_x, rolling resistance moment M_y, and self-aligning torque M_z, are generated by the tire/road contact.

To simplify the problem and focus more on the new model development for estimation and control purposes, in this and the next two chapters, we consider the case when the vehicle has only longitudinal motion. An extended three dimensional tire/road friction model combining the longitudinal and lateral motions was discussed in Claeys et al. (2001a) and Deur et al. (2001). Therefore, we have the following assumptions

---

[1]SAE stands for Society of Automotive Engineering.
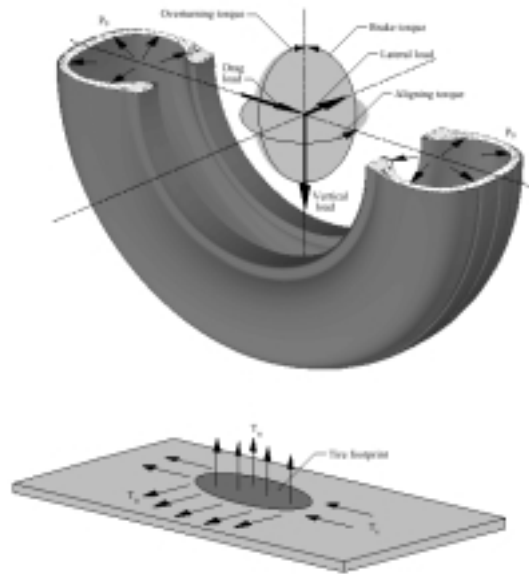
Figure 5.1: A schematic of tire/road interaction
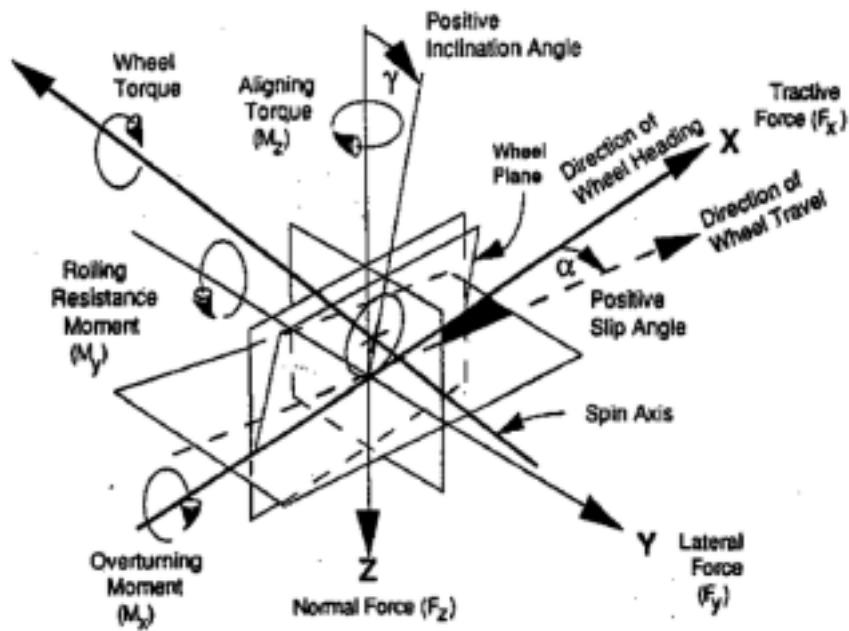
Figure 5.2: Tire/road contact forces and moments (SAE standard representation)

Assumption 5.1

1. *The vehicle only moves longitudinally, i.e. tire slip angle $\alpha = 0$ and steering angle $\vartheta = 0$.*

2. *The vehicle does not have yaw motion, i.e. yaw angle $\phi = 0$.*

3. *The tire plane is perpendicular to ground plane, i.e. tire camber angle $\gamma = 0$.*

By Assumption 5.1, we have

$$F_y = 0, \quad M_x = 0, \quad M_z = 0.$$

We will concentrate on the estimation of the longitudinal force F_x, i.e. longitudinal tire/road friction characteristics.

5.1.2 Tire/road friction characteristics

The longitudinal tire/road friction coefficient μ, or coefficient of road adhesion, or normalized friction force, is defined as [2]

$$\mu = \frac{F_x}{F_z} = \frac{\text{Friction force}}{\text{Normal force}}.$$
(5.1)

There is a significant amount of research in tire/road coefficient of friction estimation for individual vehicles. In this section, we review some major approaches.

Common to most of this research is the fact that the models used to describe the tire/road coefficient of friction employ the slip ratio of the wheel as the key variable to describe the underlying phenomenon. The slip λ is defined as a non-dimensional index that describes the difference between the longitudinal velocity of the vehicle, measured at the center of mass, and the longitudinal velocity of the tires, measured at the point of contact between the tires and the road, i.e.

$$\lambda = \begin{cases} \frac{r\omega - v}{r\omega} \,; & \text{in vehicle traction, } \omega \neq 0 \\ \frac{v - r\omega}{v} \,; & \text{in vehicle braking, } v \neq 0, \end{cases}$$
(5.2)

where r is the effective rolling radius of the tire, v and ω are the linear speed of the tire center and angular speed of the tire, respectively.
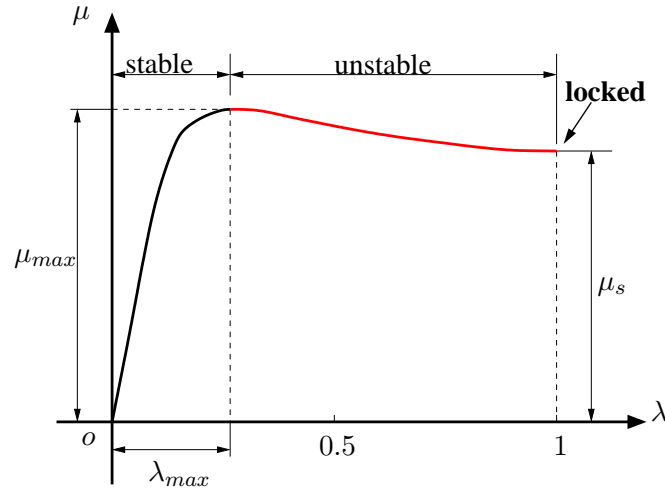
Figure 5.3: A schematic of pseudo-static tire/road friction model for a specific vehicle velocity (braking case)

The pseudo-static relationship between μ and λ, usually called a pseudo-static curve, is shown schematically in Fig. 5.3 for a given vehicle velocity and a set of tire/road conditions in the braking case. For the braking case, pseudo-static means that the velocity for each point on the μ-λ curve is fixed. By the definition of the longitudinal slip, it is easy to see that $\lambda \in [0, 1]$. When $\lambda = 0$, there

---

[2]In this report, we use μ to denote the longitudinal tire/road friction coefficient by default. We will explicitly use other variables to denote the lateral friction coefficient if necessary.

is no relative motion of the tire with respect to the ground and therefore the tire/road interaction does not generate any traction/braking forces. When $\lambda = 1$, the wheel is locked. As shown in the figure, the maximum friction coefficient μ_{max} is achieved at a particular longitudinal slip, denoted as maximum slip $\lambda_{max} \in (0,\ 1)$. When the vehicle slip satisfies $\lambda \le \lambda_{max}$, the vehicle motion is stable; otherwise, it is unstable. Moreover, the μ-λ curve varies under different tire/road conditions, vehicle normal forces, velocities, etc. Therefore, the maximum friction coefficient μ_{max} and maximum slip λ_{max} will change under varying environmental and vehicle conditions. Fig. 5.4 presents two curves, obtained from Harned et al. (1969), that represent typical μ versus λ behavior under different road conditions and vehicle velocities.

(a) Different road surface conditions

(b) Different vehicle velocities
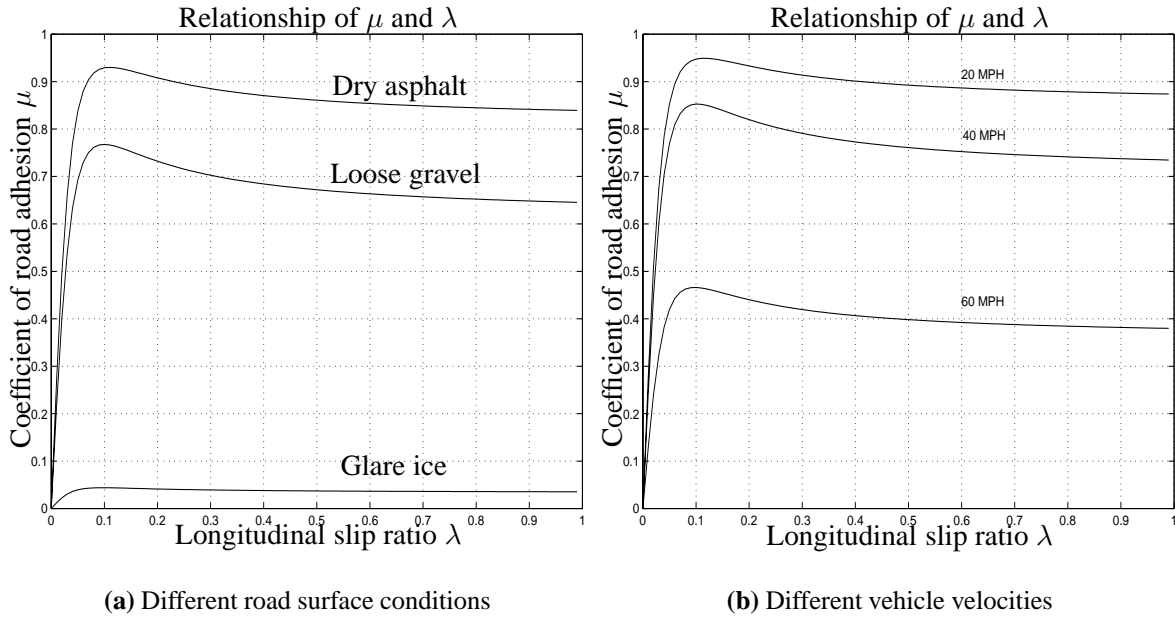
Figure 5.4: Variation of tire/road friction coefficient μ with respect to longitudinal slip λ

Empirical model approach

The pseudo-static μ-λ relationship is observed in experiments. Bakker et al. (1987), Bakker et al. (1989) and Burckhardt (1993) described two analytical models for tire/road interactions that are extensively used by researchers in the automotive industry. In these two models the friction coefficient μ is mainly determined based on the wheel slip λ and some other parameters like speed and normal load. The expression given by Bakker et al. (1987), also known as the "magic formula", was derived heuristically from experimental data to produce a good fit. As described by Bakker et al. (1987) and Bakker et al. (1989), the friction force F_x is approximated by [3]

$$F_x = C_1 \sin\left(C_2 \arctan\left(C_3\lambda + C_4 \arctan(C_5\lambda)\right)\right),\tag{5.3}$$

where model parameters $C_i,\ i = 1, \cdots, 5$, are functions of normal load F_z and determined by curve-fitting with the experimental data.

---

[3]If considering the combined longitudinal and lateral motions, the lateral force F_y and self-aligning torque are given by a similar formula.

The friction model given by Burckhardt (1993) is [4]

$$\mu = \left(C_1 \left(1 - e^{-C_2 \lambda}\right) - C_3 \lambda\right) e^{-C_4 \lambda v} \left(1 - C_5 F_z^2\right) , \qquad (5.4)$$

where v is the vehicle longitudinal velocity. In the above tire/road friction model (5.4), model parameters C_1, C_2 and C_3 change for various tire/road conditions, parameter C_4 modeles changing of vehicle speed, and parameter C_5 models changing of the normal load.

The empirical models (5.3) and (5.4) are derived by curve-fitting the observed experimental data. It is convenient to use these models for vehicle dynamics simulation and studies. There are important attempts to simplify these models, estimate the parameters of the simplified models, and use these parameters for traction/brake control (Kiencke, 1993; Kiencke and Daiss, 1994; Gustafsson, 1997). However, there are several disadvantages to using these two models for on-line estimation and control purposes:

1. First, the models are highly nonlinear in the model parameters. Therefore, it is difficult to identify the model parameters (C_i's) in real time. Once the tire or road conditions change, we have to re-calibrate the model parameters off-line using the experimental data.

2. Since these models are purely empirical curve-fits of observations, there is no physical meaning to the model parameters. It is difficult to interpret the variations of model parameters if the physical conditions have changed. In other words, there is no connection between model parameters and variations of physical conditions.

3. Finally, these models only capture the pseudo-static relationship between friction coefficient μ and longitudinal slip λ. Dynamic friction behavior has not been represented by the models. Moreover, for small slip situations, the models will not give a very accurate description of the dynamics.

Physical model approach

In order to understand the tire/road interactions, several researchers have analyzed the forces generated by the contact patch. Two different types of friction models are discussed here: pseudo-static (brush) and dynamic friction models.

(1). **Pseudo-static (brush) models**

The pseudo-static physical models assume that the friction dynamics between the tire and ground reach their steady-state, and that vehicle velocity (for braking case) or wheel angular velocity (for traction case) is constant. The basic idea of the physical model is to assume that the contact patch between the tire and the ground can be divided into an adhesion region and a sliding region. In the adhesion region, the interacting forces depend on the elastic properties of the tire; whereas in the sliding region, the interacting forces depend on the adhesive properties of the tire/road interface. Gim and Nikravesh (1990), Fancher and Bareket (1991), Wong (1993), and Fancher et al. (1997) described such a physical model approach. Here we give a brief description.

---

[4]In Burckhardt (1993), the lateral force F_y is given by the same formula with different definition of slip λ.

Assume that the tire/road sliding friction coefficient is μ_s. The tire/road contact patch is rectangular with length L and the normal load F_z is uniformly distributed on the patch. We can divide the contact into two separate regions: adhesion and sliding regions; see Fig. 5.5. We can set up a moving coordinate $O\zeta$ with the contact patch. We also assume that there is a critical length $L_c \leq L$ such that for the adhesion region, $0 \leq \zeta < L_c$ and for the sliding region, $L_c \leq \zeta \leq L$.
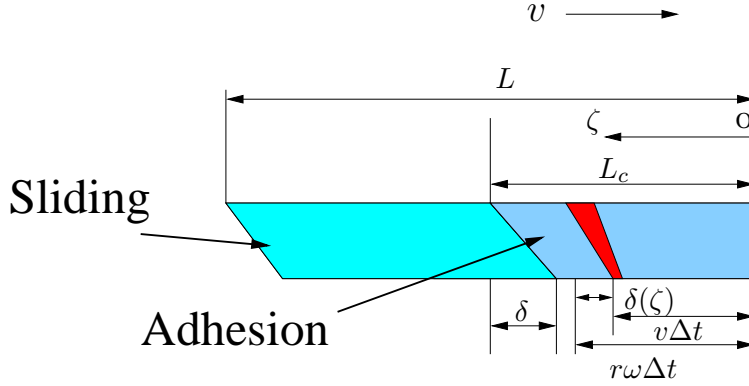
Figure 5.5: A brush model schematic of the tire contact deformation during traction.

Now we can calculate the sliding and adhesion forces:

1. In the *sliding region*, the friction force F_{x_s} opposes to the movement of the tire. The sliding force F_{x_s} is given by the fraction of the load in sliding contact with the ground.

$$F_{x_s} = \mu_s F_z \left(1 - \frac{L_c}{L} \right), \tag{5.5}$$

where L_c/L is the fraction of the adhesion patch.

2. In the *adhesion region*, the friction force is linear with tire tread deformation. Assume that the stiffness of the tire tread is F_z/L per unit length. Consider the traction case within time period Δt illustrated in Fig. 5.5.

$$\delta(\zeta) = r\omega\Delta t - v\Delta t, \quad \text{and} \quad \zeta = r\omega\Delta t.$$

Therefore, we obtain

$$\delta(\zeta) = \frac{r\omega - v}{r\omega}\zeta = \lambda\zeta, \tag{5.6}$$

and the friction force can be calculated by

$$F_{x_a} = \int_0^{L_c} dF_{x_a} = \int_0^{L_c} \frac{1}{L}\frac{F_z}{L}\delta(\zeta)d\zeta = \frac{F_z}{2}\left(\frac{L_c}{L}\right)^2 \lambda = C_s\lambda, \tag{5.7}$$

where $C_s = \frac{F_z}{2}\left(\frac{L_c}{L}\right)^2$ is the longitudinal stiffness of the tire.

The total friction force F_x at the contact patch interface is the combination of these two effects and is given by:

$$F_x = F_{x_s} + F_{x_a} = \mu_s F_z \left(1 - \frac{L_c}{L} \right) + \frac{F_z}{2} \left(\frac{L_c}{L} \right)^2 \lambda \,. \tag{5.8}$$

The fraction L_c/L can be determined as the position where the adhesion force F_{x_a} reaches its critical value $F_{a_c} = C_s \lambda_c$ where sliding begins. It is easy to see that $L_c/L = \lambda_c/\lambda$ and thus Eq. (5.8) becomes

$$F_x = F_{x_s} + F_{x_a} = \mu_s F_z \left(1 - \frac{\lambda_c}{\lambda} \right) + \frac{F_z}{2} \frac{\lambda_c^2}{\lambda} = \mu_s F_z \left[1 + \frac{1}{\lambda} \left(\lambda_c - \frac{\lambda_c^2}{2} \right) \right] \,, \tag{5.9}$$

where $\lambda_c = F_{a_c}/C_s$.
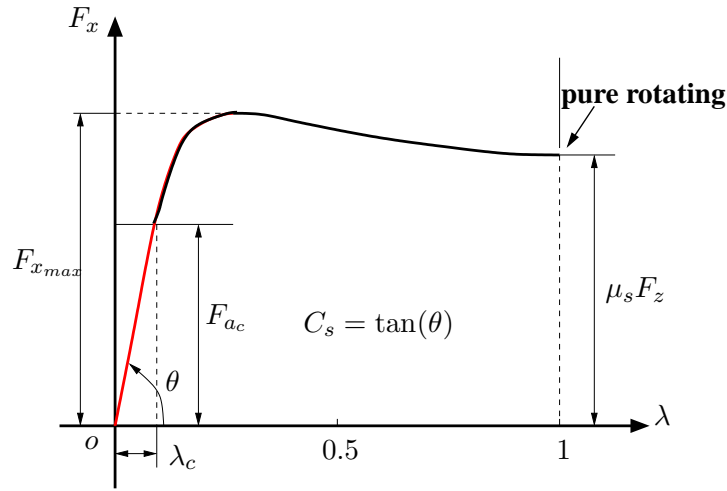
Figure 5.6: Longitudinal force F_x of pseudo-static (brush) physical tire/road friction model for a specific wheel angular velocity (traction case)

Fig. 5.6 illustrates the underlying physical meaning of model (5.9) for the traction case. When longitudinal slip $0 \le \lambda \le \lambda_c$, the friction force F_x is given by the adhesion portion and thus is linear with slip λ. Once the slip $\lambda_c < \lambda \le 1$, the contact patch is also partially sliding and the total friction force F_x is contributed to by both adhesion and sliding forces. When the wheel is purely rotating, i.e. $\lambda = 1$, the friction force $F_x \approx \mu_s F_z$ is given by Eq. (5.9).

The same example could be applied to the lateral direction in order to calculate the lateral force F_y (Gim and Nikravesh, 1990; Fancher and Bareket, 1991; Fancher et al., 1997).

(2) .**Dynamic friction models**

Although the brush models explain the physical deflections of the tire tread, they do not describe the dynamic friction behavior of the tire/road interface because of the assumption that the deformation reaches its steady-state. However, the dynamic friction behavior is sometimes important for studying vehicle dynamics and stability. For example, when the braking/traction torques change significantly, we need to study the tire dynamics for large relative velocities.

Recently, several dynamic friction models have been proposed and used to study and compensate friction in mechanical and electromechanical systems. These dynamic friction models use hysteresis models to describe the process of compression and expansion that takes place at the region of contact between two surfaces. The first version of such a model is called *Dahl friction model*. Basically, Dahl (1976) describes friction as a dynamical system. Let x be the relative displacement of the two contact surfaces and v is the relative velocity between the two surfaces. The model is given by

$$\frac{dF}{dx} = \sigma_0 \left(1 - \frac{F}{F_c} \, \text{sign}(v) \right)^\alpha ,$$

(5.10)

where σ_0 is the stiffness coefficient, and α is a parameter that determines the shape of the stress-strain curve. The value $\alpha = 1$ is most commonly used. The friction force $|F|$ will never be larger than F_c if its initial value satisfies $|F(0)| < F_c$, where F_c is the maximal friction force (Coulomb friction force). Bliman (1992), Bliman and Sorine (1991) and Bliman and Sorine (1995) extended the Dahl friction model by using two internal friction states to capture different friction properties. Canudas de Wit et al. (1995) proposed the so-called *LuGre friction model* [5] using only one internal friction state to capture different friction characteristics. We will give a brief description of these dynamic friction models in Chapter 5.2. For details about the LuGre dynamic friction model, readers can refer to Olsson (1996).

One interesting property of using dynamic friction models to describe tire/road interaction is that these models can reproduce the pseudo-static relationship between the friction coefficient μ and slip λ (Bliman et al., 1995; Canudas de Wit and Tsiotras, 1999; Canudas de Wit and Horowitz, 1999; Yi et al., 2000). Therefore, we can use these models to capture the tire/road friction characteristics. We will discuss in detail the use of the LuGre dynamic friction model in tire/road friction estimation and braking control in later chapters.

Other approaches of estimating the friction coefficient μ

There is a significant amount of research that focuses on determining the instantaneous value of the coefficient of friction and using this value for control purposes, for example, Lee and Tomizuka (1995), Ray (1997), Yi and Jeong (1998) and Yi et al. (1999). Pasterkamp and Pacejka (1997) and Pal et al. (1994) proposed a neural network technique to estimate the friction coefficient. In Jansen et al. (2000) and Sorine and Szymanski (2000), the dynamics of the tire belt are considered using a second-order dynamic friction model; some simulation results are compared with the "magic formula". In the analytical and experimental work of Sakai (1982), Gim and Nikravesh (1990), and Dixon (1991), the dynamical properties of the tire are discussed. Finite element methods have also been applied to analyze the tire dynamical properties (Mastinu and Fainello, 1992; Tanner, 1996).

All of the above modeling work did not consider different environmental variations such as rain, road conditions etc. The studies of Horne and Buhlmann (1983), Lenke and Graul (1986), and Bareket and Fancher (1989) discussed the effect of different pavements. The effects of tire pressure variations and distributions have been investigated analytically and experimentally in Lippmann and Oblizajek (1974), Clark (1981) and Gim and Nikravesh (1990). There is little work that considers the effect of temperature on the tire/road friction despite the fact that this is a very important

[5]The LuGre acronym comes from the two university names that authors are affiliated: **Lu**nd Institute of Technology in Sweden and Laboratoire d'Automatique de **Gre**noble in France.

factor. All of these physical models of the tire/road interface employed either mechanical analysis of tire deflection (and/or finite element methods), or empirical curve-fitting to experimental data for a particular type of tire on a specific road. Moreover, these models are very complicated and thus are not attractive for estimation and vehicle control.

5.1.3 Tire/road friction models used in this project

In this project, we will focus on a tire/road friction estimation scheme using dynamic model approaches. In MOU 312, we proposed a new pseudo-static friction model and an adaptation scheme was then presented to estimate the model parameters. Based on this friction model and the estimation scheme, an emergency braking control law was designed. An attractive property of that controller is that, by choosing appropriate initial conditions of adaptation parameters and gains, underestimation of the maximum friction coefficient and slip can be guaranteed, which is very important for vehicle operation safety. In this project, we investigate how the LuGre dynamic friction model can be used for tire/road friction estimation and brake control system design. In particular, we consider the design of an emergency braking maneuver. In Task Order 4207, we extend the dynamic friction model systematically to capture more physical variations. Two specific models have been studied: a three dimensional friction model combined longitudinal and lateral motions, and a tire friction model under wet road conditions.

5.2 Adaptive Emergency Braking Control Using a Dynamic Tire/road Friction Model

In MOU 312, we proposed an empirical pseudo-static tire/road friction model and an emergency braking controller was designed based on this model. In this chapter, we explore a physical friction modeling approach to the tire/road interaction. We first introduce a dynamic friction model, the so-called *LuGre* model, and then apply it to the problem of tire/road interactions. Two emergency braking controllers are designed using this dynamic friction model: the first one assumes that the friction internal state and the vehicle velocity information is known while the second one relaxes this assumption by constructing a state observer.

5.2.1 The LuGre dynamic friction model

Friction is an important issue in the control of electro-mechanical systems. Control strategies that attempt to compensate the effects of friction, without resorting to high gain loops, require a suitable friction model to predict and cancel its adverse effects. Most classical friction models, such as the Coulomb and viscous friction models, describe the static relationship between the friction force and the velocity (Armstrong-Hélouvry et al., 1994; Olsson, 1996). As pointed out in Canudas de Wit et al. (1995), these classical models cannot explain certain observed phenomena, such as (1) the hysteresis behavior that appears when studying friction for non-stationary velocities, (2) variations in the break-away force with the experimental condition, and (3) small displacements that occur at the contact interface during stiction [6]. In order to capture these friction characteristics, it is necessary

---

[6]Sometimes this phenomena is also referred to as the Dahl effect (Dahl, 1976).

to introduce dynamics into the friction model.

In Bliman and Sorine (1995), a two state variable dry friction model was presented with some desired properties for control purposes. These properties permitted a unified description of kinetic and static friction and suitably captured the Dahl and Stribeck effects and stick slip. The model in Bliman and Sorine (1995) can be described as

$$
\begin{cases}
\dot{\mathbf{x}} = |\dot{v}|A\mathbf{x} + B\dot{v} \\
F = C\mathbf{x} + D\operatorname{sign}(\dot{v}),
\end{cases}
\tag{5.11}
$$

where $\mathbf{x} = [x_1, \ x_2]^T$ is the internal state vector, v is the relative velocity between two sliding surfaces, and

$$
A = -\frac{1}{\epsilon}\begin{bmatrix} \frac{1}{\eta} & 0 \\ 0 & 1 \end{bmatrix}, \quad B = \frac{1}{\epsilon}\begin{bmatrix} \frac{f_1}{\eta} \\ -f_2 \end{bmatrix}, \quad C = \begin{bmatrix} 1 & 1 \end{bmatrix}, \quad D = 0,
$$

$\eta > 0$ dimensionless, $\epsilon > 0$ is a distance, $f_1 > 0$ and $f_2 \geq 0$ are known forces. The Bliman model (5.11) has been applied to the tire/road friction estimation by considering a distributed contact patch between the tire and the ground. The case of longitudinal motion was treaded in Bliman et al. (1995), while combined longitudinal and lateral motions was developed in Sorine and Szymanski (2000). Due to its complexity, it is not convenient to apply this model to friction estimation and automatic control.

Recently, a simpler dynamic friction model, the *LuGre* friction model, was proposed and has been applied to friction compensations of various mechanical-electrical systems (Canudas de Wit et al., 1995; Canudas de Wit and Lischinsky, 1997; Hirschorn and Miller, 1999). The LuGre friction model can be described as

$$
\begin{cases}
\dot{z} = v_r - \frac{\sigma_0|v_r|}{h(v_r)}z \\
F = (\sigma_0 z + \sigma_1 \dot{z} + \sigma_2 v_r)F_n,
\end{cases}
\tag{5.12}
$$

where z is an internal friction state, v_r is the relative velocity, $h(v_r) = \mu_c + (\mu_{st} - \mu_c)e^{-|\frac{v_r}{v_s}|^{1/2}}$, σ_0 is the stiffness coefficient, σ_1 is the damping coefficient, σ_2 is the viscous relative damping coefficient, μ_{st} is the normalized static friction coefficient, μ_c is the normalized Coulomb friction, and v_s is the Stribeck relative velocity.

The LuGre friction model can be interpreted as describing the forces generated by the interaction between two brush-like surfaces (see Fig. 5.7.) The bristles on the lower surface are assumed to be rigid for simplicity. Each bristle on the upper surface transfers forces that are captured by the spring/dumper model shown in Fig. 5.7. The LuGre model is obtained by aggregating their effects, and introducing a viscous term ($\sigma_2 v$) (Canudas de Wit et al., 1995).

Note that we have the following properties for the LuGre model (5.12):

Property 5.1
1. $\mu_c \leq \mu_{st}$ and $\mu_c, \mu_{st} \in [0, \ 1]$;
2. if $|z(0)| < \frac{\mu_{st}}{\sigma_0}$, then $|z(t)| < \frac{\mu_{st}}{\sigma_0}, \forall t \geq 0$;
3. $0 < \mu_c \leq h(v_r) \leq \mu_{st} < \infty$;
4. The change rate of the internal state z is proportional to the parameter σ_0 and it converges faster for large σ_0.

67
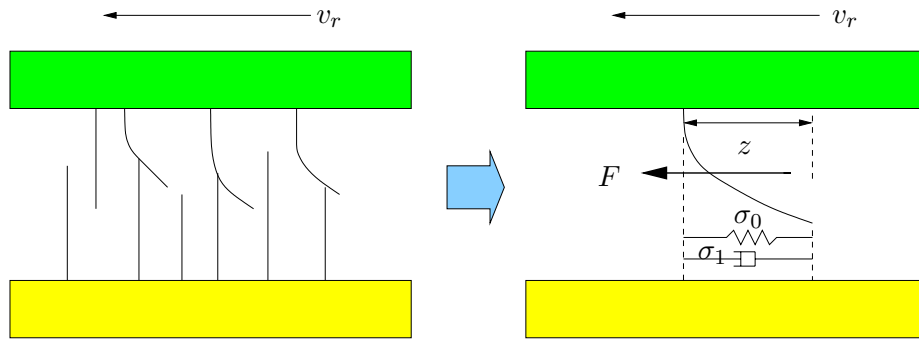
Figure 5.7: A schematic of bristle contact between two surfaces for LuGre friction model.

It has been shown that the LuGre model (5.12) can reduce to the Dhal model and, moreover, it can capture the Stribeck effect, hysteresis, spring-like characteristics for stiction, and varying break-away force (Canudas de Wit et al., 1995). One of the attractive properties of the LuGre model is that all these friction phenomena are unified into a first-order nonlinear differential equation. However, in order to use the LuGre model to predict and compensate the friction, we must construct a state observer for the internal friction state z. Moreover, parameter estimation and adaptation schemes are needed to accommodate the variations in physical conditions.

In the remainder of this chapter, we will explore the use of the LuGre dynamic friction model to describe the tire/road interaction. Basically, we are trying to address two problems: estimation of tire/road friction and emergency braking control under various conditions. In section 5.2.2, we assume that the internal state z in the friction model and the vehicle longitudinal velocity v are known and an adaptation scheme and a braking controller are then presented to achieve the maximum deceleration. In section 5.2.3, we relax the assumption of availability of internal state z and velocity v by construction of a model-based observer.

5.2.2 Adaptive emergency braking control with full information

The goal of the proposed scheme in this section is to design an on-line strategy for vehicles to estimate their own tire/road friction characteristics and the overall gain of the braking system. We will investigate the application of the LuGre dynamic friction model to the tire/road interaction for the braking process. A distributed LuGre friction model is proposed and compared with the lumped model. The wheel relative velocity that achieves maximum braking effort in a quasi-static LuGre friction model solution is estimated on line, assuming that the tire/road friction model dynamics is much faster than the vehicle braking dynamics. This information is used to design a controller that achieves near-maximum braking effort.

A distributed LuGre tire/road friction model

Canudas de Wit and Tsiotras (1999) first applied the LuGre model to the tire/road interaction for a vehicle traction case. In Canudas de Wit and Horowitz (1999), an estimation scheme of the tire/road friction was proposed using only the wheel angular velocity information. Variations in the tire and road were modeled in Canudas de Wit and Horowitz (1999) with an external model variable $\theta\ (> 0)$.

The modified LuGre dynamic friction model is given by

$$
\begin{cases}
\dot{z} = v_r - \theta \frac{\sigma_0 |v_r|}{h(v_r)} z \\
F = (\sigma_0 z + \sigma_1 \dot{z} + \sigma_2 v_r) F_n \,,
\end{cases}
\tag{5.13}
$$

where $v_r = r\omega - v$, r is the wheel radius, ω is the wheel angular velocity and v is the vehicle longitudinal velocity. The introduction of the new model parameter θ into the dynamics (5.13) can be taken as an exchange of the function $h(v_r)$ by $\frac{h(v_r)}{\theta}$, due to the variations in tire and road conditions [7].

The dynamic model in Eq. (5.13) is a lumped parameter model with only one internal state z, i.e. point-to-point contact. As discussed in Canudas de Wit and Tsiotras (1999) it is also possible to obtain a distributed friction dynamic model by assuming the existence of a contact patch between tire and ground (see Fig. 5.8.)

Before preceding with the derivation of the model, we make the following assumptions:

Assumption 5.2
1. *The vehicle has only longitudinal motion.*
2. *The contact patch between the tire and road is rectangular.*
3. *The pressure is uniformly distributed on the tire/road contact patch.*
4. *The wheel radius does not change during the braking process.*
5. *The dynamics of the tire rubber belt are not considered, i.e. we consider a rigid rubber belt.*
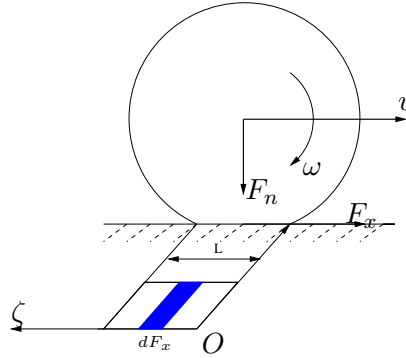
Figure 5.8: A schematic of one vehicle wheel with distributed force.

Based on the above assumptions and following the same procedures as those given in Canudas de Wit and Tsiotras (1999) for the traction case, we can develop a quasi-static μ-λ curve for the braking case. The distributed LuGre friction model is given as

$$
\begin{cases}
\frac{d\delta z}{dt}(\zeta, t) = v_r - \theta \frac{\sigma_0 |v_r|}{h(v_r)} \delta z \\
F_x = \int_0^L (\sigma_0 \delta z + \sigma_1 \delta \dot{z} + \sigma_2 v_r) \delta F_z d\zeta
\end{cases}
\tag{5.14}
$$

---

[7]In fact, introducing only one parameter θ cannot capture the variations of **all** tire and road conditions. It can possibly capture **part** of variations of tire/road conditions, for example, wet road condition, etc. However, to simplify the estimation and control system design, we only consider one parameter θ for variations of tire and road conditions in this chapter.

with boundary conditions as

$$\delta z(0,t) = \delta z(L,t) = 0, \qquad \forall t \geq 0, \tag{5.15}$$

where $\delta F_z = F_z/L$ and L is the length of the patch which is assumed to be constant. Assume that v and ω are constant and $\frac{\partial \delta z}{\partial t}(\zeta, t) = 0$ within a small enough interval of time, essentially a quasi-static condition. Then we have

$$\begin{cases} \frac{d\delta z}{d\zeta}(\zeta) = \frac{v_r}{r\omega} - \theta \frac{\sigma_0 |v_r/r\omega|}{h(v_r)} \delta z & \zeta \in (0,\ L) \\ \delta(0) = \delta(L) = 0\,. \end{cases} \tag{5.16}$$

Defining $\eta = v_r/r\omega$ and solving the above equation for $\delta z(\zeta)$ with initial condition $\delta z(\zeta) = \zeta = 0$, we obtain

$$\delta z(\zeta) = \begin{cases} \frac{h(v_r)}{\theta \sigma_0} (e^{-\theta \frac{\sigma_0 |\eta|}{h(v_r)}\zeta} - 1), & 0 \leq \zeta \leq \frac{L}{2} \\ \frac{h(v_r)}{\theta \sigma_0} \left[e^{-\theta \frac{\sigma_0 |\eta|}{h(v_r)}(L-\zeta)} - 1 \right], & \frac{L}{2} < \zeta \leq L\,. \end{cases}$$

Calculating the friction force term by term using Eq. (5.14) we obtain

$$\int_0^L \delta z(\zeta) d\zeta = -\frac{h(v_r)}{\theta \sigma_0} L \left[1 + \frac{2h(v_r)}{\theta \sigma_0 L |\eta|} (e^{-\frac{\theta \sigma_0 |\eta| L}{2h(v_r)}} - 1) \right]$$

$$\int_0^L \delta \dot{z}(\zeta) d\zeta = -\frac{2vh(v_r)}{\theta \sigma_0} \left(1 - e^{-\frac{\theta \sigma_0 |\eta| L}{2h(v_r)}} \right)$$

then for constant velocity v we have

$$F_x(\eta, v) = -\frac{F_z h(v_r)}{\theta} \left[1 + 2\gamma \frac{h(v_r)}{\theta \sigma_0 L |\eta|} (e^{-\frac{\theta \sigma_0 L |\eta|}{2h(v_r)}} - 1) \right] - F_z \sigma_2 v_r \tag{5.17}$$

where

$$\eta = \frac{v_r}{r\omega} = \frac{\lambda}{1-\lambda}, \quad \gamma = 1 - \frac{\theta \sigma_1 |\eta|}{r\omega h(v_r)},$$

and $\lambda = 1 - r\omega/v$ is the longitudinal slip ratio. This formula is similar to the traction case derived in Canudas de Wit and Tsiotras (1999) that considers the angular velocity ω to be constant. $\lambda \in [0,\ 1]$ is used in Canudas de Wit and Tsiotras (1999) while $\eta \in (-\infty,\ 0]$ is used here.

Remark 5.1 In the pseudo-static curve in Eq. (5.17) we assume constant velocity. If velocity changes, the curve changes as well. However, by taking a look at the dynamic equation for the internal state z we find that it changes much faster than the vehicle dynamics. Therefore, we can make the assumption that, for each time step, this formula can be used to calculate the approximated maximum peak value for the braking force produced by the tire/road friction.

Remark 5.2 The static curve in Eq. (5.17) is a function of longitudinal slip ratio λ. In the braking case it has been defined as $\lambda = \frac{v-r\omega}{v}$. When the vehicle's velocity becomes very small, the relationship does not have a physical interpretation. However, since we are interested in finding a controller strategy for braking the car at fairly high speeds, we can use this approach for large velocities and establish a lower bound v_{min} to obtain good braking.

70

The distributed model given by Eq. (5.14) is consistent with the lumped model given by Eq. (5.13) in the following sense: assuming that the patch region does not change with time and defining

$$\bar{z}(t) = \frac{1}{L} \int_0^L \delta z(\zeta, t) d\zeta \,, \tag{5.18}$$

we have

$$\dot{\bar{z}}(t) = \frac{d}{dt} \left(\frac{1}{L} \int_0^L \delta z(\zeta, t) d\zeta \right) = \frac{1}{L} \int_0^L \frac{\partial}{\partial t} \left(\delta z(\zeta, t) \right) d\zeta \,, \tag{5.19}$$

we know that

$$
\begin{aligned}
\delta \dot{z} &= \frac{d}{dt}(\delta z(\zeta, t)) = \frac{\partial}{\partial t}(\delta z(\zeta, t)) + \frac{\partial}{\partial \zeta}(\delta z(\zeta, t))\dot{\zeta} \\
&= \frac{\partial}{\partial t}(\delta z(\zeta, t)) + v\frac{\partial}{\partial \zeta}(\delta z(\zeta, t)) = v_r - \theta \frac{\sigma_0 |v_r|}{h(v_r)}\delta z(\zeta, t) \,,
\end{aligned}
$$

then Eq. (5.19) becomes

$$
\begin{aligned}
\dot{\bar{z}}(t) &= \frac{1}{L} \int_0^L \left(\delta \dot{z} - v\frac{\partial}{\partial \zeta}(\delta z(\zeta, t)) \right) d\zeta \\
&= \frac{1}{L} \int_0^L \left(v_r - \theta \frac{\sigma_0 |v_r|}{h(v_r)}\delta z(\zeta, t) \right) d\zeta - \frac{1}{L} \int_0^L v\frac{\partial}{\partial \zeta}(\delta z(\zeta, t)) d\zeta \\
&= \frac{1}{L} \int_0^L v_r d\zeta - \theta \frac{\sigma_0 |v_r|}{h(v_r)} \frac{1}{L} \int_0^L \delta z(\zeta, t) d\zeta - \frac{v}{L} \left[\delta z(L, t) - \delta z(0, t) \right] \\
&= v_r - \theta \frac{\sigma_0 |v_r|}{h(v_r)}\bar{z} \tag{5.20}
\end{aligned}
$$

in the last step we use Eq. (5.15).

Similarly, we can find the friction force given by Eq. (5.14) using the state $\bar{z}$ as

$$F_x = \int_0^L (\sigma_0 \delta z + \sigma_1 \delta \dot{z} + \sigma_2 v_r)\delta F_z d\zeta = F_z \left(\sigma_0 \bar{z} + \sigma_2 v_r + \frac{\sigma_1}{L} \int_0^L \delta \dot{z} d\zeta \right) \,,$$

note that

$$
\begin{aligned}
\frac{1}{L} \int_0^L \delta \dot{z} d\zeta &= \frac{1}{L} \int_0^L \left(\frac{\partial}{\partial t}(\delta z(\zeta, t)) + v\frac{\partial}{\partial \zeta}(\delta z(\zeta, t)) \right) d\zeta \\
&= \frac{1}{L} \int_0^L \frac{\partial}{\partial t}(\delta z(\zeta, t)) d\zeta + \frac{v}{L} \left[\delta z(L, t) - \delta z(0, t) \right] \\
&= \frac{d}{dt} \left(\frac{1}{L} \int_0^L \delta z(\zeta, t) d\zeta \right) = \dot{\bar{z}}(\zeta, t) \,,
\end{aligned}
$$

therefore

$$F_x = (\sigma_0 \bar{z} + \sigma_1 \dot{\bar{z}} + \sigma_2 v_r)F_z \tag{5.21}$$

71

Remark 5.3 Comparing the lumped LuGre dynamic model in Eqs. (5.20) and (5.21) with the lumped model in Eq. (5.13), we find that the lumped model for the tire/road dynamics can be obtained by using the transformation in Eq. (5.18) and converting the PDE in Eq. (5.14) into the ODE in Eq. (5.20).

Remark 5.4 In the above derivation of the equivalence between the lumped and the distributed LuGre friction models, we used the simplifying assumption that the tire and road contact patch is rectangular and the pressure is uniformly distributed on this patch. We thus defined the boundary condition $\delta z(L, t) = 0$, and the distributed model was shown to be equivalent to the lumped model by the transformation (5.18). If we consider a non-uniform pressure distribution and non-symmetric deformations of the tire rubber belt on the contact patch, then $\delta z(L, t) \neq 0$ and we cannot conclude the equivalence between these two models (Deur, 2001). In Deur (2001), a modified equivalent lumped LuGre model was derived as

$$
\begin{cases}
\dot{z} = v_r - \left(\theta \frac{\sigma_0 |v_r|}{h(v_r)} + \frac{\kappa}{L} r\omega \right) z \\
F_x = (\sigma_0 z + \sigma_1 \dot{z} + \sigma_2 v_r) F_z \,,
\end{cases}
\tag{5.22}
$$

where κ is the ratio of the deformation at the edge $\zeta = L$ to the average deformation along the contact patch [8]. In Deur (2001), κ is taken as a constant between a value of 1.1 and 1.4, i.e., $\kappa \in [1.1, 1.4]$. With the modified lumped LuGre model (5.22), the estimation and control scheme developed in this chapter can be easily modified since the wheel angular velocity ω is measurable. For simplicity, we use the lumped LuGre model given by (5.13) in our design.

In order to see the consistence between the LuGre dynamic friction model with the pseudo-static tire/road friction relationship, we compare the pseudo-static curve in Eq. (5.17) obtained from the dynamical model, against the magic formula for one of the tested tires in Schuring (1976). Fig. 5.9 shows the results using the formula in Eq. (5.17). From the figure we see that the dynamic model can fit the experimental data very well. The parameters for the LuGre dynamic model are listed in Table 5.1.

Table 5.1: Parameters used for the static curve of Eq. (5.17).

Parameters	Values	Units
σ_0	100	$1/m$
σ_1	0.7	s/m
σ_2	0.011	s/m
μ_{st}	0.5	–
μ_c	0.35	–
v_s	10.0	m/s
L	0.25	m

---

[8]For more details about the definition of κ, reader is referred to Deur (2001) and Canudas de Wit et al. (2001).
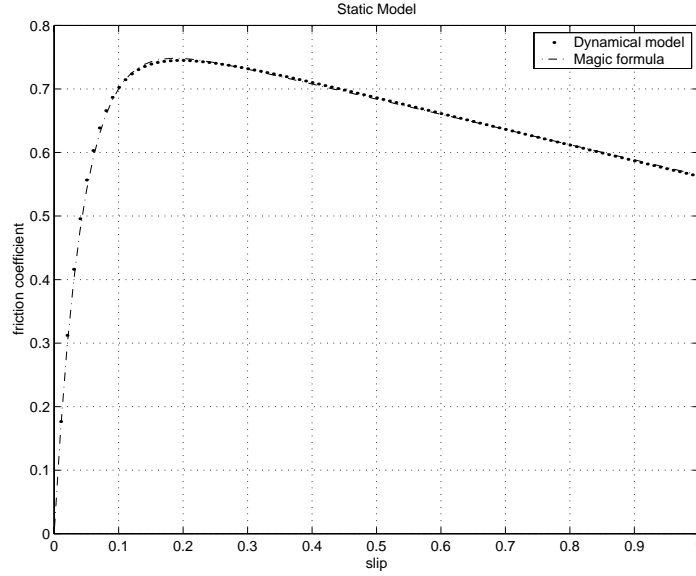
Figure 5.9: Comparison between the LuGre dynamic model and the "magic formula" for a tested tire in braking case with $v = 30\ mph$ and $\theta = 1$ in the model

System dynamics

In order to model and control the system dynamics using the LuGre friction model, we consider, in addition to Assumption 5.2, the following assumptions regarding the wheel and vehicle dynamics.

Assumption 5.3

1. *Normal forces on the tires are constant and evenly distributed.*
2. *The braking forces are equal on all tires.*
3. *The friction internal state z and the vehicle velocity v are known.*
4. *The wheel angular velocity ω is measurable.*
5. *The road is flat, i.e. the slope of the road is zero.*

   Based on the above assumptions, we consider the LuGre model together with vehicle dynamics as:

$$
\begin{cases}
\dot{z} = v_r - \theta \frac{\sigma_0 |v_r|}{h(v_r)} z \\
J\dot{\omega} = -rF_x - \sigma_\omega \omega - u_\tau \\
m\dot{v} = 4F_x - F_{av} ,
\end{cases}
\tag{5.23}
$$

where σ_ω is the coefficient of the viscous resistance moments, $F_{av} = C_{av}v^2$ is the aerodynamic force, u_τ is the traction/braking torque, and F_x is the traction/braking force given by the tire/road contacting. The braking force F_x is given by

$$
F_x = F_n(\sigma_0 z + \sigma_1 \dot{z} + \sigma_2 v_r) .
$$

Define the state variables as

$$
x_1 := z, \quad x_2 := v, \quad , x_3 := v_r = r\omega - v
$$

and rewrite the system dynamics in Eq. (5.23) as

$$\dot{x}_1 = \dot{z} = x_3 - \theta \frac{\sigma_0 |x_3|}{h(x_3)} x_1 = x_3 - \theta f(x_3) x_1 \tag{5.24}$$

where $f(x_3) = \frac{\sigma_0 |x_3|}{h(x_3)}$, $h(x_3) = \mu_c + (\mu_{st} - \mu_c) e^{-|\frac{x_3}{v_s}|^{1/2}}$,

$$\dot{x}_2 = g \left[\sigma_0 x_1 + \sigma_1 (x_3 - \theta f(x_3) x_1) + \sigma_2 x_3 \right] - C_{av} x_2^2 \tag{5.25}$$

g is the gravity constant and $C_{avm} = C_{av}/m$. For the state variable x_3 we have

$$\dot{x}_3 = q \left[\sigma_0 x_1 + \sigma_1 (x_3 - \theta f(x_3) x_1) \right] - g \sigma_2 x_3 + C_{av} x_2^2 - \frac{r \sigma_\omega}{J} (x_2 + x_3) - \frac{r}{J} K_b P_b, \tag{5.26}$$

where $q = -\left(g + \frac{F_n r^2}{J} \right)$. In the above equation we use the same formula $u_\tau = K_b P_b$ as the previous chapter, where K_b is the brake coefficient gain and P_b the brake pressure which is the controlled variable.

Controller design

The objective of an emergency braking maneuver is to bring the vehicle to a stop as quickly as possible. We need to design a braking controller that achieves a vehicle longitudinal slip close to λ_{max}, while keeping the vehicle stable. In Tan and Tomizuka (1990), a traction control was designed to force the slip to track λ_{max}, assuming that λ_{max} is known and fixed. In Drakunov et al. (1995), a sliding mode controller and friction force observer achieve maximum friction force using an extremum seeking technique.

In this section, we use the LuGre dynamic tire/road friction model to estimate the maximum slip λ_{max} by means of an equivalent pseudo-static model given in Eq. (5.17). Thus, assuming that v is known, we can calculate the maximum slip λ_{max} by solving for it numerically from the equivalent pseudo-static model in Eq.(5.17):

$$\lambda_{max} = \arg \max_\lambda \left\{ \mu(\eta, v, \hat{\theta}) \right\}. \tag{5.27}$$

Note that the tire/road condition (θ) is unknown. If we can guarantee that $\hat{\theta} \to \theta$, then we can achieve the maximum deceleration.

Arrange the system dynamics (5.24), (5.25) and (5.26) as

$$\begin{cases} \dot{x}_1 = x_3 - f_1(\mathbf{x}) \theta \\ \dot{x}_2 = f_2(\mathbf{x}) - \left[g \sigma_1 f_1(\mathbf{x}) \right] \theta \\ \dot{x}_3 = f_3(\mathbf{x}) - \left[q \sigma_1 f_1(\mathbf{x}) \right] \theta - \frac{r}{J} K_b P_b, \end{cases} \tag{5.28}$$

where

$$\begin{aligned} f_1(\mathbf{x}) &= f(x_3) x_1, \quad f_2(\mathbf{x}) = g \left[\sigma_0 x_1 + (\sigma_1 + \sigma_2) x_3 \right] - C_{avm} x_2^2 \\ f_3(\mathbf{x}) &= q \sigma_0 x_1 + (q \sigma_1 - g \sigma_2) x_3 + C_{avm} x_2^2 - \frac{\sigma_\omega}{J} (x_2 + x_3). \end{aligned}$$

Define

$$\tilde{s} := x_3 - x_{3d}(\hat{\theta}) = x_3 + \lambda_{max}(\hat{\theta})x_2 \,,$$

where $\lambda_{max}(\hat{\theta})$ is the peak value of the longitudinal slip λ under current conditions based on the estimated parameter $\hat{\theta}$ given by Eq. (5.27). Differentiate $\tilde{s}$ to obtain

$$\dot{\tilde{s}} \;=\; \dot{x}_3 + \dot{x}_2 \lambda_{max} + x_2 \dot{\lambda}_{max} = \varrho K_b P_b + \beta_1(\mathbf{x})\theta + \beta_2(\mathbf{x}) \,, \qquad (5.29)$$

where

$$\varrho = -\frac{r}{J}, \; \beta_1(\mathbf{x}) = -\left[q\sigma_1 f_1(\mathbf{x}) + g\sigma_1 f_1(\mathbf{x})\lambda_{max} \right], \; \beta_2(\mathbf{x}) = \left[f_3(\mathbf{x}) + x_2 \dot{\lambda}_{max} + \lambda_{max} f_2(\mathbf{x}) \right].$$

Let $M_b := \frac{1}{K_b}$ be the adaptation variable and define the error variables

$$\tilde{\theta} := \theta - \hat{\theta}, \qquad \tilde{M}_b := M_b - \hat{M}_b \,.$$

Let the control input P_b be

$$P_b = \frac{\hat{M}_b}{\varrho}\left[-\beta_1(\mathbf{x})\hat{\theta} - \beta_2(\mathbf{x}) - \eta\tilde{s} \right], \qquad (5.30)$$

where $\eta > 0$ is a control gain. Then the dynamics for $\tilde{s}$ in Eq. (5.29) can be described as

$$\dot{\tilde{s}} = K_b \hat{M}_b \left[-\beta_1(\mathbf{x})\hat{\theta} - \beta_2(\mathbf{x}) - \eta\tilde{s} \right] + \beta_1(\mathbf{x})\theta + \beta_2(\mathbf{x})$$
$$= \beta_1(\mathbf{x})\tilde{\theta} - \eta\tilde{s} + K_b \tilde{M}_b \left[\beta_1(\mathbf{x})\hat{\theta} + \beta_2(\mathbf{x}) + \eta\tilde{s} \right] . \qquad (5.31)$$

Consider now the following Lyapunov candidate

$$V = \frac{1}{2}\tilde{s}^2 + \frac{1}{2\gamma}\tilde{\theta}^2 + \frac{1}{2\xi}K_b \tilde{M}_b^2 \,,$$

where $\gamma > 0, \; \xi > 0$ are gains. Then

$$\dot{V} \;=\; \tilde{s}\dot{\tilde{s}} + \frac{1}{\gamma}\tilde{\theta}\dot{\tilde{\theta}} + \frac{1}{\xi}K_b \tilde{M}_b \dot{\tilde{M}}_b$$
$$=\; \tilde{s}\left[\beta_1\tilde{\theta} - \eta\tilde{s} + K_b \tilde{M}_b(\beta_1\hat{\theta} + \beta_2 + \eta\tilde{s}) \right] + \frac{1}{\gamma}\tilde{\theta}\dot{\tilde{\theta}} + \frac{1}{\xi}K_b \tilde{M}_b \dot{\tilde{M}}_b$$
$$=\; \tilde{\theta}\left[\beta_1\tilde{s} + \frac{1}{\gamma}\dot{\tilde{\theta}} \right] + K_b \tilde{M}_b \left[\frac{\dot{\tilde{M}}_b}{\xi} + \tilde{s}(\beta_1\hat{\theta} + \beta_2 + \eta\tilde{s}) \right] - \eta\tilde{s}^2 \,.$$

Letting

$$\dot{\hat{\theta}} = \gamma\beta_1(\mathbf{x})\tilde{s},$$
$$\dot{\hat{M}}_b = \xi\tilde{s}\left[\beta_1(\mathbf{x})\hat{\theta} + \beta_2(\mathbf{x}) + \eta\tilde{s} \right], \qquad (5.32)$$

we obtain

$$\dot{V} = -\eta\tilde{s}^2 \leq 0 \,.$$

By Lyapunov's theorem, $(\tilde{s} = 0, \tilde{\theta} = 0, \tilde{M}_b = 0)$ is a stable equilibrium point and $\tilde{s}$, $\tilde{\theta}$ and $\tilde{M}_b$ are bounded. Notice that

$$\ddot{V} = -2\eta\tilde{s}\dot{\tilde{s}}$$

is bounded. Thus, by Barbalat's Lemma, $\tilde{s} \to 0$ as $t \to \infty$, and

$$x_3 \to -\lambda_{max}(\hat{\theta})x_2 \ .$$

Remark 5.5 Even if we can calculate the dynamic surface by Eq. (5.17), we still need to compute its time derivative. We approach this by numerical differentiation which can be easily implemented. A low-pass filter is used to smooth the numerical noise in the input.

Simulation results

In the simulation we use the parameters from the LeSabre cars used in the California PATH program. These parameters are: $m = 1701.0 \ Kg$, $C_{av} = 0.3693 \ N \cdot s^2/m^2$, $J = 2.603 \ Kg \cdot m^2$, $r = 0.323m$. We also assumed the characteristic parameter to be $\theta = 1$, and the brake coefficient gain $K_b = 0.9$, therefore $M = 1/K_b = 1.11$.

We simulate a vehicle starting an emergency braking maneuver at the initial velocity $v = 30m/s$, by applying the designed controller without an observer. Fig. 5.10 shows the vehicle's velocity change as well as the internal state z and the relative velocity $(-v_r)$.
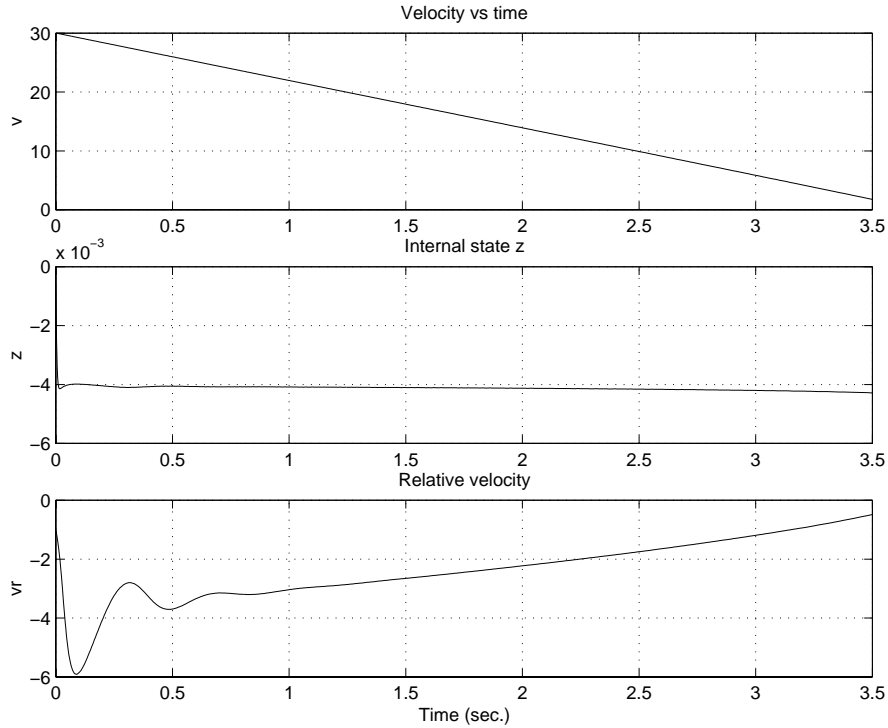
Figure 5.10: Vehicle velocity v (m/s), internal state z and relative velocity v_r (m/s)

The controlled brake pressure and the sliding surface errors are illustrated in Fig. 5.11. The adaptations of parameters θ and K_b are plotted in Fig. 5.12. From the simulation results we find that

the vehicle stopped quickly with an almost constant deceleration (around $8m/s^2$) and both of the parameters K_b and θ converge to the true values 0.9 and 1.0, respectively. Using this control, we can achieve braking around its peak value at each transient time, and this can be seen from the Fig. 5.13, which shows the friction coefficient and slip during the emergency braking. Note that the slip ratio converges to the value estimated by the dynamic model.
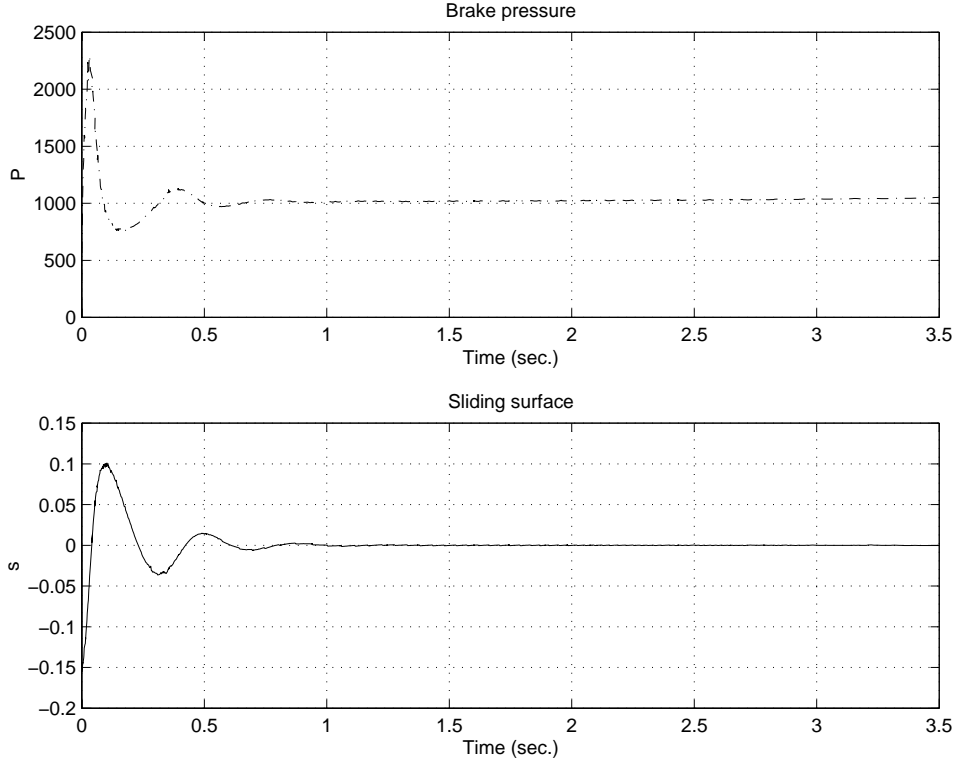
Figure 5.11: Brake pressure P (KPa) and sliding surface $\tilde{s}$

5.2.3 Observer-based adaptive emergency braking control with only wheel angular velocity information

Motivation

In the previous section, we discussed the use of the LuGre dynamic friction model to describe the tire/road interaction. An adaptive friction estimation scheme and an emergency braking controller were investigated analytically and numerically with an assumption of availability of the internal friction state z and the vehicle velocity v. However, since state z in the LuGre dynamic friction model and the vehicle longitudinal velocity v are typically not measurable, an observer must be constructed to estimate these state variables using only the measurable wheel angular velocity. In this section, we explore the approach of the observer-based adaptive controller synthesis.
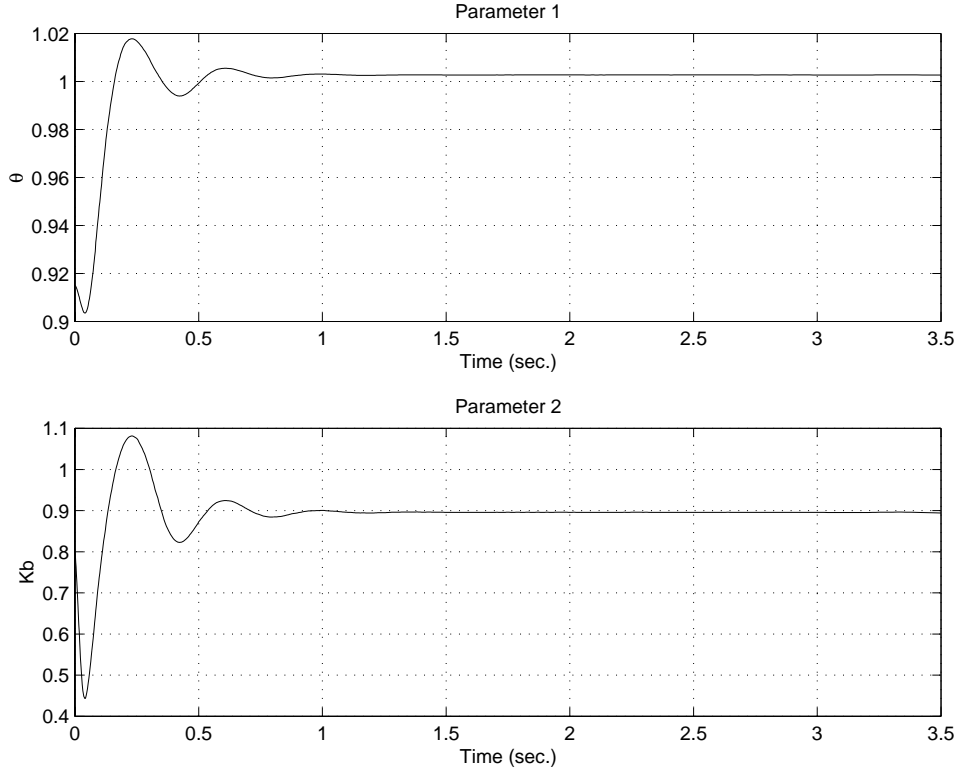
Figure 5.12: Friction characteristic parameter θ and brake coefficient K_b (Nm/KPa)

System dynamics and control objectives

We will retain the system dynamics given by Eqs. (5.28) with the replacement of the quadratic aerodynamic term $F_{av} = C_{av}v^2$ with a linear force of rolling resistance $F_r = \sigma_v mgv$, in order to simplify the analysis [9]. σ_v is the rolling resistance coefficient and g is the gravity constant (Wong, 1993). We define the following state variables

$$x_1 := \sigma_0 z, \quad x_2 := v, \quad , x_3 := v_r = v - r\omega.$$

For most vehicles, we can measure the angular velocity of each wheel, thus the output equation can be obtained as

$$y = \omega = \frac{1}{r}(x_2 - x_3) \tag{5.33}$$

Rearrange the dynamics (5.28) and (5.33) as

$$\begin{cases} \dot{\mathbf{x}} = A\mathbf{x} + B_1\theta\psi(\mathbf{x}) + B_2 u \\ y = C\mathbf{x} \end{cases} \tag{5.34}$$

---

[9]Since both the aerodynamics coefficient C_{av} and the rolling resistance coefficient σ_v are tiny, the change of F_{av} with F_r does not affect the system dynamics much. However, it changes the structure of the system dynamics to avoid the singularity. We will discuss the convergence rate in section 5.2.3.
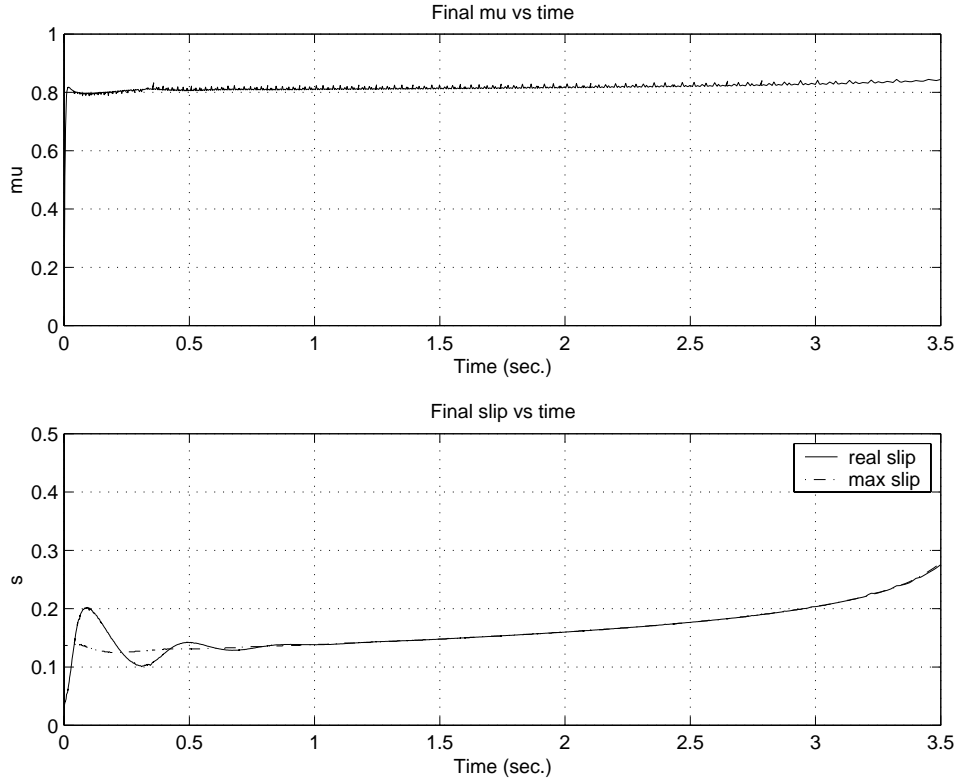
Figure 5.13: Friction coefficient μ and slip λ during emergency braking

where

$$\mathbf{x} = \begin{bmatrix} x_1 \\ x_2 \\ x_3 \end{bmatrix}, \ A = \begin{bmatrix} 0 & 0 & -\sigma_0 \\ g & -g\sigma_v & -g(\sigma_2 + \sigma_1) \\ q & -g\sigma_v & -q(\sigma_2 + \sigma_1) \end{bmatrix}, \ B_1 = \begin{bmatrix} -\sigma_0 \\ -g\sigma_1 \\ -q\sigma_1 \end{bmatrix}, \ B_2 = \begin{bmatrix} 0 \\ 0 \\ \frac{r}{J}K_b \end{bmatrix},$$

$$C = \begin{bmatrix} 0 & \frac{1}{r} & -\frac{1}{r} \end{bmatrix}, \quad \psi(\mathbf{x}) = x_1 f(x_3), \quad u = P_b.$$

Note that the internal friction state z and the vehicle longitudinal velocity v are assumed not to be measurable, and the tire/road condition (θ) is unknown. It is therefore difficult to obtain λ_{max} for the current vehicle control design. It is necessary to construct an observer that guarantee $\hat{v} \to v$ and $\hat{\theta} \to \theta$, so that near maximum deceleration can be achieved around $\hat{\lambda}_{max}$. $\hat{\lambda}_{max}$ can be determined from the estimated velocity ($\hat{v}$) and parameter ($\hat{\theta}$) as follows:

$$\hat{\lambda}_{max} = \arg\max_{\hat{v},\lambda,\hat{\theta}} \left\{ \hat{\mu}(\lambda, \hat{v}, \hat{\theta}) \right\}. \tag{5.35}$$

Another important control objective, which is needed to preserve vehicle steering stability, is to always underestimate the slip during an emergency braking maneuver, namely to ensure $\hat{\lambda}_{max}(t) \leq \lambda_{max}(t)$.

Observer-based braking controller design

In this section we formulate the design of a controller, based on the available angular velocity output. We construct the following model-based nonlinear observer

$$\dot{\hat{\mathbf{x}}} = A\hat{\mathbf{x}} + B_1\hat{\theta}\psi(\hat{\mathbf{x}}) + B_2u + L_2(y - C\hat{\mathbf{x}}) + B_1\mathcal{G}, \tag{5.36}$$

where $\mathcal{G}$ is a tuning function to be determined and $L_2 \in \mathbb{R}$ is the observer gain.

The following assumptions are made for the system (5.34) and observer (5.36):

(i) (A, B_1) is controllable and (A, C) is observable;

(ii) $f(x_3)$ is non-negative and bounded and $f'(x_3)$ is bounded, i.e.

$$0 \le f(x_3) \le f_{max} \le \rho_2 < \infty, \quad |f'(x_3)| \le \rho_3 < \infty, \ \forall x_3 \in \mathbb{R}. \tag{5.37}$$

(iii) The unknown parameter θ is bounded, i.e.

$$0 < \theta \le \theta_{max}. \tag{5.38}$$

(iv) The map $w \mapsto \xi$ of the system

$$\begin{cases} \dot{\zeta} = (A - L_2C)\zeta + B_1w \\ \xi = C\zeta \end{cases} \tag{5.39}$$

with $(A - L_2C)$ Hurwitz, is strictly passive; moreover, $\exists \rho_1 > 0$ a constant, and $\exists P = P^T > 0$ such that

$$(A - L_2C)^TP + P(A - L_2C) + (\rho_1^2 + \rho_4)I < 0 \tag{5.40}$$

as well as

$$PB_1 = C^T, \tag{5.41}$$

where $\rho_4 = \frac{2\theta_{max}\rho_2}{r} > 0$.

Theorem 5.1 *Under assumptions (i) – (iv) there exists an adaptive emergency braking controller that achieves*

$$\hat{\lambda} \to \hat{\lambda}_{max}$$

asymptotically for the system (5.34) using the measured angular velocity ω, where the estimated slip $\hat{\lambda} := \frac{\hat{x}_3}{\hat{x}_2} = \frac{\hat{v} - r\hat{\omega}}{\hat{v}}$ and $\hat{\lambda}_{max} := \hat{\lambda}_{max}(\hat{v}_r, \hat{v})$ is the longitudinal slip corresponding to the estimated maximum friction coefficient $\hat{\mu}_{max}$ in the pseudo-static relationship between μ and λ, given by Eq.(5.17).

Proof: Define $\tilde{\mathbf{x}} := \mathbf{x} - \hat{\mathbf{x}}$, $\tilde{y} := y - \hat{y} = C\tilde{\mathbf{x}}$ and $\tilde{\theta} := \theta - \hat{\theta}$, then the error dynamics for the system is

$$\dot{\tilde{\mathbf{x}}} = (A - L_2C)\tilde{\mathbf{x}} + B_1\left[\theta\psi(\mathbf{x}) - \hat{\theta}\psi(\hat{\mathbf{x}})\right] - B_1\mathcal{G}. \tag{5.42}$$

Define the dynamic surface $\tilde{s}$ as

$$\tilde{s} := \hat{x}_3 - \hat{\lambda}_{max}\hat{x}_2$$

80

and differentiate $\tilde{s}$:

$$
\begin{aligned}
\dot{\tilde{s}} &= \dot{\hat{x}}_3 - \dot{\hat{x}}_2 \hat{\lambda}_{max} - \dot{\hat{\lambda}}_{max} \hat{x}_2 \\
&= \frac{r}{J} K_b P_b - \sigma_1 (q - g\hat{\lambda}_{max}) f(\hat{x}_3)\hat{\theta} + \Big\{ (q - g\hat{\lambda}_{max}) \left[\hat{x}_1 - (\sigma_2 + \sigma_1)\hat{x}_3 \right. \\
&\quad \left. -(1 - \hat{\lambda}_{max}) g\sigma_v \hat{x}_2 \right] + (l_3 - l_2\hat{\lambda}_{max})\tilde{y} \Big\} - \sigma_1 (q - g\hat{\lambda}_{max})\mathcal{G} - \dot{\hat{\lambda}}_{max}\hat{x}_2 \\
&= \varrho K_b P_b + \beta_1(\hat{\mathbf{x}})\hat{\theta} + \beta_2(\hat{\mathbf{x}}) + \beta_3(\hat{\mathbf{x}})\mathcal{G} \tag{5.43}
\end{aligned}
$$

where

$$
\varrho = \frac{r}{J}, \quad \beta_1(\hat{\mathbf{x}}) = -\sigma_1(q - g\hat{\lambda}_{max})f(\hat{x}_3)\hat{x}_1,
$$

$$
\beta_2(\hat{\mathbf{x}}) = (q - g\hat{\lambda}_{max}) \left[\hat{x}_1 - (\sigma_2 + \sigma_1)\hat{x}_3\right] + (l_3 - l_2\hat{\lambda}_{max})\tilde{y} - \dot{\hat{\lambda}}_{max}\hat{x}_2 - (1 - \hat{\lambda}_{max})g\sigma_v\hat{x}_2,
$$

$$
\beta_3(\hat{\mathbf{x}}) = -\sigma_1(q - g\hat{\lambda}_{max}),
$$

and l_2, l_3 are the second and third elements of the gain vector $L_2 \in \mathbb{R}^3$.

Consider the following Lyapunov function candidate

$$
V = \frac{1}{2}\tilde{s}^2 + \frac{1}{2\gamma}\tilde{\theta}^2 + \tilde{\mathbf{x}}^T P \tilde{\mathbf{x}},
$$

where $\gamma > 0$. Then

$$
\begin{aligned}
\dot{V} &= \dot{\tilde{\mathbf{x}}}^T P \tilde{\mathbf{x}} + \tilde{\mathbf{x}}^T P \dot{\tilde{\mathbf{x}}} + \tilde{s}\dot{\tilde{s}} + \frac{1}{\gamma}\tilde{\theta}\dot{\tilde{\theta}} \\
&= \tilde{\mathbf{x}}^T \left[(A - L_2C)^T P + P(A - L_2C)\right] \tilde{\mathbf{x}} + 2\tilde{\mathbf{x}}^T P B_1 \left[\theta\psi(\mathbf{x}) - \hat{\theta}\psi(\hat{\mathbf{x}})\right] + \\
&\quad \frac{1}{\gamma}\tilde{\theta}\dot{\tilde{\theta}} + \tilde{s}\dot{\tilde{s}} - 2\tilde{\mathbf{x}}^T P B_1 \mathcal{G}.
\end{aligned}
$$

Notice that

$$
\theta\psi(\mathbf{x}) - \hat{\theta}\psi(\hat{\mathbf{x}}) = \tilde{\theta}\psi(\hat{\mathbf{x}}) + \theta\left[\psi(\mathbf{x}) - \psi(\hat{\mathbf{x}})\right]
$$

and use fact (5.41) to obtain

$$
\begin{aligned}
\dot{V} &= \tilde{\mathbf{x}}^T \left[(A - L_2C)^T P + P(A - L_2C)\right] \tilde{\mathbf{x}} + 2\tilde{y}\tilde{\theta}\psi(\hat{\mathbf{x}}) + 2\tilde{\mathbf{x}}^T P B_1 \theta\left[\psi(\mathbf{x}) - \psi(\hat{\mathbf{x}})\right] + \\
&\quad \frac{1}{\gamma}\tilde{\theta}\dot{\tilde{\theta}} + \tilde{s}\left[\varrho K_b P_b + \beta_1(\hat{\mathbf{x}})\hat{\theta} + \beta_2(\hat{\mathbf{x}}) + \beta_3(\hat{\mathbf{x}})\mathcal{G}\right] - 2\tilde{\mathbf{x}}^T P B_1 \mathcal{G}. \tag{5.44}
\end{aligned}
$$

Let the control input be

$$
u = P_b = \frac{1}{\varrho K_b}\left[-\beta_1(\hat{\mathbf{x}})\hat{\theta} - \beta_2(\hat{\mathbf{x}}) - \beta_3(\hat{\mathbf{x}})\mathcal{G} - \xi\tilde{s}\right],
$$

then Eq.(5.43) becomes

$$
\dot{\tilde{s}} = -\xi\tilde{s}. \tag{5.45}
$$

Using (5.41) and (5.45) and letting

$$
\dot{\hat{\theta}} = 2\gamma\tilde{y}\psi(\hat{\mathbf{x}}), \tag{5.46}
$$

81

we obtain from Eq.(5.44)

$$\dot{V} = \tilde{\mathbf{x}}^T \left[(A - L_2 C)^T P + P(A - L_2 C) \right] \tilde{\mathbf{x}} + 2\tilde{\mathbf{x}}^T P B_1 \theta \left[\psi(\mathbf{x}) - \psi(\hat{\mathbf{x}}) \right] - \xi \tilde{s}^2 - 2\tilde{y}\mathcal{G}.$$

Note that

$$\psi(\mathbf{x}) - \psi(\hat{\mathbf{x}}) \;=\; x_1 f(x_3) - \hat{x}_1 f(\hat{x}_3) = f(x_3)\tilde{x}_1 + \hat{x}_1 f'(x_3^*)(x_3 - \hat{x}_3),$$

where x_3^* is a value between x_3 and $\hat{x}_3$ derived by applying the Mean Value Theorem to the smooth function $f(x) = \frac{x}{h(x)}$. Moreover, by Eqs. (5.37), (5.38) and (5.46)

$$
\begin{aligned}
\dot{V} \;\leq\;& \tilde{\mathbf{x}}^T \left[(A - L_2 C)^T P + P(A - L_2 C) \right] \tilde{\mathbf{x}} + 2\tilde{\mathbf{x}}^T C^T \theta_{max} \rho_2 \tilde{x}_1 + 2\rho_3 \theta_{max} |\tilde{y}||\hat{x}_1||\tilde{x}_3| - \\
& \xi \tilde{s}^2 - 2\tilde{y}\mathcal{G} \\
=\;& \tilde{\mathbf{x}}^T \left[(A - L_2 C)^T P + P(A - L_2 C) \right] \tilde{\mathbf{x}} + \frac{1}{r}\theta_{max}\rho_2(2\tilde{x}_1\tilde{x}_2 - 2\tilde{x}_1\tilde{x}_3) + \\
& 2\rho_3\theta_{max}|\tilde{y}||\hat{x}_1||\tilde{x}_3| - \xi\tilde{s}^2 - 2\tilde{y}\mathcal{G} \\
\leq\;& \tilde{\mathbf{x}}^T \left[(A - L_2 C)^T P + P(A - L_2 C) \right] \tilde{\mathbf{x}} + \rho_4\left(\tilde{x}_1^2 + \frac{1}{2}\tilde{x}_2^2 + \frac{1}{2}\tilde{x}_3^2 \right) - \\
& \frac{\rho_4}{2}\left(|\tilde{x}_3| - \frac{\rho_3 r}{\rho_2}|\tilde{y}\hat{x}_1| \right)^2 + \frac{\rho_4}{2}\tilde{x}_3^2 + \frac{\rho_4}{2}\left(\frac{\rho_3 r}{\rho_2} \right)^2 \hat{x}_1^2\tilde{y}^2 - \xi\tilde{s}^2 - 2\tilde{y}\mathcal{G} \\
\leq\;& \tilde{\mathbf{x}}^T \left[(A - L_2 C)^T P + P(A - L_2 C) + \rho_4 I \right] \tilde{\mathbf{x}} - \xi\tilde{s}^2 - \\
& \frac{\rho_4}{2}\left(|\tilde{x}_3| - \frac{\rho_3 r}{\rho_2}|\tilde{y}\hat{x}_1| \right)^2 + \tilde{y}\left[\frac{\rho_4}{2}\left(\frac{\rho_3 r}{\rho_2} \right)^2 \hat{x}_1^2\tilde{y} - 2\mathcal{G} \right] \\
\leq\;& -\rho_1^2\|\tilde{\mathbf{x}}\|^2 - \xi\tilde{s}^2 - \frac{\rho_4}{2}\left(|\tilde{x}_3| - \frac{\rho_3 r}{\rho_2}|\tilde{y}\hat{x}_1| \right)^2 + \tilde{y}\left[\frac{\rho_4}{2}\left(\frac{\rho_3 r}{\rho_2} \right)^2 \hat{x}_1^2\tilde{y} - 2\mathcal{G} \right].
\end{aligned}
$$

If we choose $\mathcal{G}$ such that

$$\mathcal{G} = \frac{\rho_4}{4}\left(\frac{\rho_3 r}{\rho_2} \right)^2 \hat{x}_1^2\tilde{y} \tag{5.47}$$

then

$$\dot{V} \;\leq\; -\rho_1^2\|\tilde{\mathbf{x}}\|^2 - \xi\tilde{s}^2 - \frac{\rho_4}{2}\left(|\tilde{x}_3| - \frac{\rho_3 r}{\rho_2}|\tilde{y}\hat{x}_1| \right)^2 \leq 0.$$

Using Barbalat's Lemma, we can conclude that

$$\tilde{s} \to 0, \quad \tilde{\mathbf{x}} \to 0, \qquad \text{as } t \to \infty.$$

Thus, by definition of $\tilde{s}$ and λ we have

$$\hat{\lambda} \to \hat{\lambda}_{max} \qquad \text{as } t \to \infty.$$

∎

82

Remark 5.6 To compute the controlled input P_b we need to know $\hat{\lambda}_{max}$ and $\dot{\hat{\lambda}}_{max}$. We use Eq. (5.35) to calculate the estimated maximum slip $\hat{\lambda}_{max}$ under current estimated vehicle velocity and tire/road conditions. $\dot{\hat{\lambda}}_{max}$ is then calculated numerically. The tuning function $\mathcal{G}$ given by (5.47) is a linear function of $\tilde{y}$ and appears both in the observer and the control input. Compared with the tuning function in Canudas de Wit and Horowitz (1999), Eq. (5.47) does not require switching in the control input, and therefore produces a smoother control.

Remark 5.7 The adaptive nonlinear observer structure presented in this section is similar to the scheme presented in Cho and Rajamani (1997), although the results in Cho and Rajamani (1997) require an additional Lipschitz assumption on the function $\psi(x)$, and condition (5.41) is replaced by $B_1^T P C^\perp = 0$ where $C^\perp$ is the projection onto $\mathrm{null}(C)$.

Assumptions (i) through (iv) must be satisfied by the system dynamics described by Eq. (5.34) for the theorem to hold:

(1). Regarding assumption (i), we can calculate the observability matrix

$$
\mathcal{O} = \begin{bmatrix} 0 & \frac{1}{r} & -\frac{1}{r} \\ \frac{g-q}{r} & 0 & \frac{a}{r} \\ \frac{qa}{r} & -\frac{g\sigma_v a}{r} & \frac{(g-q)\left[q(\sigma_2+\sigma_1)^2+\sigma_0\right]}{r} \end{bmatrix}
$$

where $a = (\sigma_2 + \sigma_1)(q - g)$, thus $rank(\mathcal{O}) = 3$, and (A, C) is an observable pair. Similarly, the controllability matrix $\mathcal{C} = \begin{bmatrix} B_1 & AB_1 & A^2 B_1 \end{bmatrix}$ satisfies $rank(\mathcal{C}) = 3$. Hence, assumption (i) always holds;

(2). To see that assumption (ii) is always satisfied, we have

$$
0 \le f(x_3) = \frac{x_3}{h(x_3)} \le \frac{x_3}{\mu_c} \le \frac{\lambda_{max} v_{max}}{\mu_c} = \rho_2
$$

and

$$
|f'(x_3)| \le \frac{1}{\mu_c}\left\{1 + \left(\frac{\mu_{st}}{\mu_c} - 1\right)\left[1 + \frac{1}{2}\left(\frac{v_{max}}{v_s}\right)^{1/2}\right]\right\} = \rho_3 .
$$

(3). Assumption (iv) is satisfied by construction. As for (iv), we must pick an observer gain L_2 and a positive symmetric matrix P such that following optimization problem is feasible

$$
\begin{cases} \max & \rho_1 \\ \text{s.t.:} & (A - L_2 C)^T P + P(A - L_2 C) + \rho_1^2 I + \rho_4 I < 0 \\ & P B_1 = C^T, \quad P = P^T > 0 \ \text{and} \ \rho_1 > 0 \end{cases}
$$

This can be calculated by linear matrix inequality (LMI) algorithms, such as those presented in El Ghaoui et al. (1995).

83

Simulation results and discussion

In the following simulation example we use the parameters from the LeSabre cars used by the California PATH program. These parameters are: $m = 1701.0\ Kg$, $\sigma_v = 0.005\ N \cdot s^2/m^2$, $J = 2.603\ Kg \cdot m^2$, $r = 0.323m$. We also take the LuGre road friction parameter in Eq (5.23) to be $\theta = 1$ and the braking gain $K_b = 0.9$. The nominal values of the parameters in the dynamic LuGre friction model are the same as those in the previous section.

We simulate an emergency braking maneuver with a vehicle initial velocity of $v = 30m/s$ and the designed observer-based controller. The initial condition for the observer dynamics is $\hat{\mathbf{x}}(0) = [0\ 29.5\ 0]^T$ and the true state is $\mathbf{x}(0) = [0\ 30\ 0.5]^T$; namely we use the measurement $r\omega$ ($=29.5\,m/s$) as the initial condition for $\hat{v}$. Fig. 5.14 shows the time responses of the real state vector $\mathbf{x}$ and estimated state vector $\hat{\mathbf{x}}$, while Fig. 5.15(c) shows the time response of the estimated friction parameter $\hat{\theta}$. Fig. 5.15(a) shows the time response of the controlled pressure P while Fig. 5.15(b) shows the controlled sliding surface $\tilde{s}$. Fig. 5.15(d) illustrates the difference, $\tilde{y}$, between the measurement y and output of observer $\hat{y}$. From these figures we can see that the estimated state $\hat{z}$ and parameter $\hat{\theta}$ converge to their respective true values quickly, and that the controlled input (pressure P) remains within its feasible domain, enabling the vehicle to come to a quick halt (decelerating at around $10\,m/s^2$). This example verifies the results of the previous section. However, the simulation results also reveal that the estimated states $\hat{v}$ and $\hat{v}_r$ do not converge to their true states during the braking process, remaining within a constant offset, even though the vehicle achieved its maximum estimated deceleration level, which is based on estimated states, as shown by Fig. 5.15(b).

In what follows we present a formal explanation of the above simulation results.

From the state error dynamics (5.42) we find that

$$\dot{\tilde{y}} = -\frac{1}{r}[l_2 - l_3 + \sigma_1(g - q)\mathbf{g}]\tilde{y} + f_1(\tilde{\mathbf{x}}), \qquad (5.48)$$

where $f_1(\tilde{\mathbf{x}}) = (g - q)[(1 - \sigma_1\theta f(x_3)]\tilde{x}_1 - \sigma_v\tilde{x}_2 - (\sigma_1 + \sigma_2)\tilde{x}_3 - \sigma_1[\theta f(x_3) - \hat{\theta}f(\hat{x}_3)]\hat{x}_1$ and $\mathbf{g} = \frac{\rho_4}{4}\left(\frac{\rho_3 r}{\rho_2}\right)^2 \hat{x}_1^2$. In our example, we chose a relatively large value for the gain L_2 with $l_2 > l_3$ ($L_2 = [-400\ -60\ -500]^T$). As a consequence, $\tilde{y} \to 0$ quickly. Similarly, we can also assume that $\tilde{\theta} \to 0$ quickly, due to our choice of a high adaptation gain ($\gamma = 200$) and the presence of persistent excitation, which we observed in the numerical example [10].

Using the approximation $\tilde{y} \approx 0$ and $\tilde{\theta} \approx 0$, we now analyze the dynamics of the state errors (5.42) and obtain

$$\dot{\tilde{\mathbf{x}}} = \bar{A}(x_3)\tilde{\mathbf{x}}, \qquad (5.49)$$

where

$$\bar{A}(x_3) = \begin{bmatrix} -\sigma_0\theta f(x_3) & 0 & 0 \\ g[1 - \sigma_1\theta f(x_3)] & -g\sigma_v & -g\sigma_2 \\ q[1 - \sigma_1\theta f(x_3)] & -g\sigma_v & -q\sigma_2 \end{bmatrix}.$$

Notice that $\sigma_0 = 100$, $\hat{\theta} \approx 1$ and $\frac{v}{\mu_c} \geq f(x_3) > \frac{v_r}{\mu_{st}}$. We can therefore conclude that $\tilde{x}_1 \to 0$ quickly with a decay rate of around $\sigma_0\theta f(x_3)$ during the beginning of the braking process, due to the fact

---

[10]The conclusion for the case of in which we do not have persistent excitation is similar with a complicated analysis. We only present a simplified analysis here.
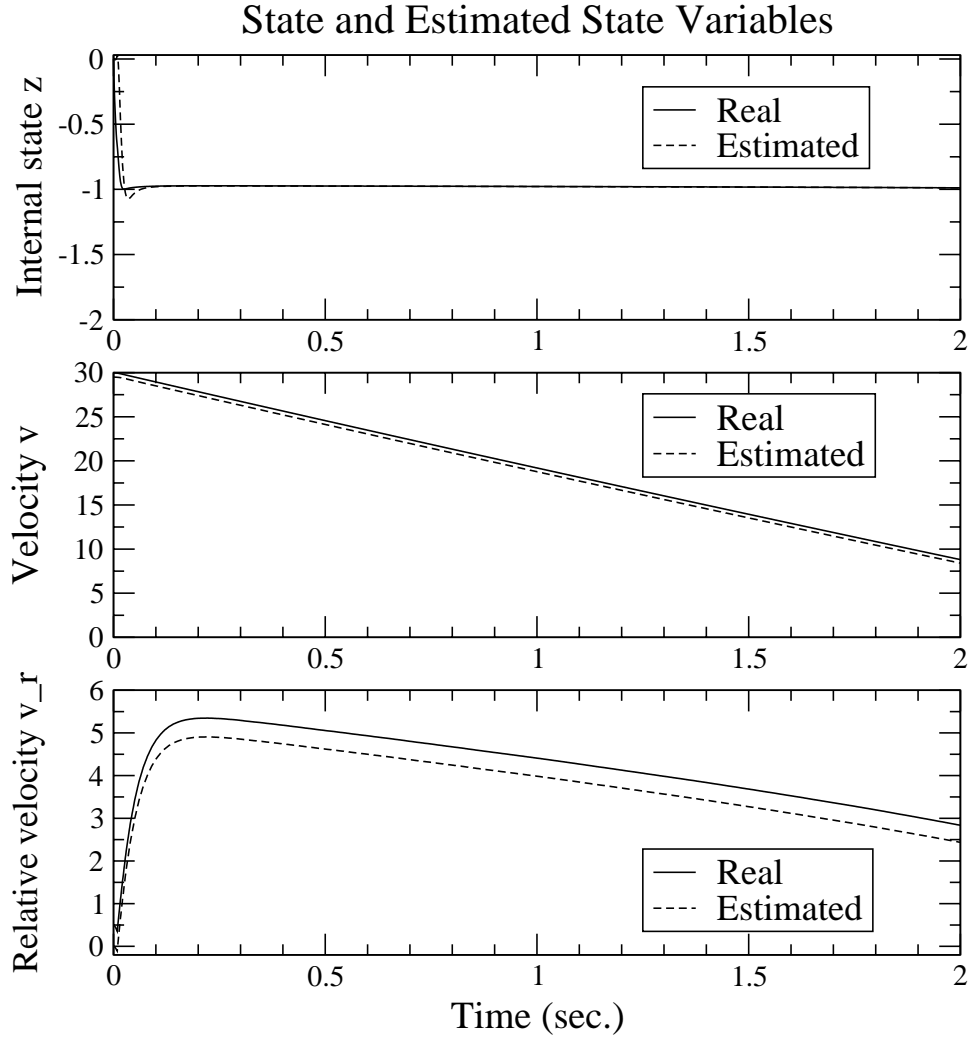
Figure 5.14: Estimated and real state variables.

that v_r is large. This explains why the estimated state $\hat{x}_1$ converges quickly to the real state x_1. In the case of the state estimates $\hat{x}_2$ and $\hat{x}_3$, from Eq. (5.49) we find that the eigenvalues of matrix $\bar{A}(x_3)$ associated with these two states are

$$ s_{2,3} = \frac{-(g\sigma_v + q\sigma_2) \pm \sqrt{(g\sigma_v)^2 + (q\sigma_2)^2 + 4g^2\sigma_v\sigma_2}}{2} . $$

Since σ_v and σ_2 are very small,

$$ -1 \ll s_{2,3} < 0, \qquad \forall t \geq 0 . $$

The rate of decay for $\tilde{x}_2$ and $\tilde{x}_3$ is small and the eigenvector associated with s_2 is around $w_2 \approx [0 \ 1 \ 1]^T$.

Fig. 5.16 shows a sketch of the trajectory of the approximate nonlinear system (5.49). For any initial condition $P_0 = (\tilde{x}_1(0), \tilde{x}_2(0), \tilde{x}_3(0)) \in \mathcal{R}^3$, the flow trajectory will quickly approach the $\tilde{x}_2 \times \tilde{x}_3$ plane because of the rapid convergence of $\tilde{x}_1$ (s_1 is large). Moreover, the trajectory will

85
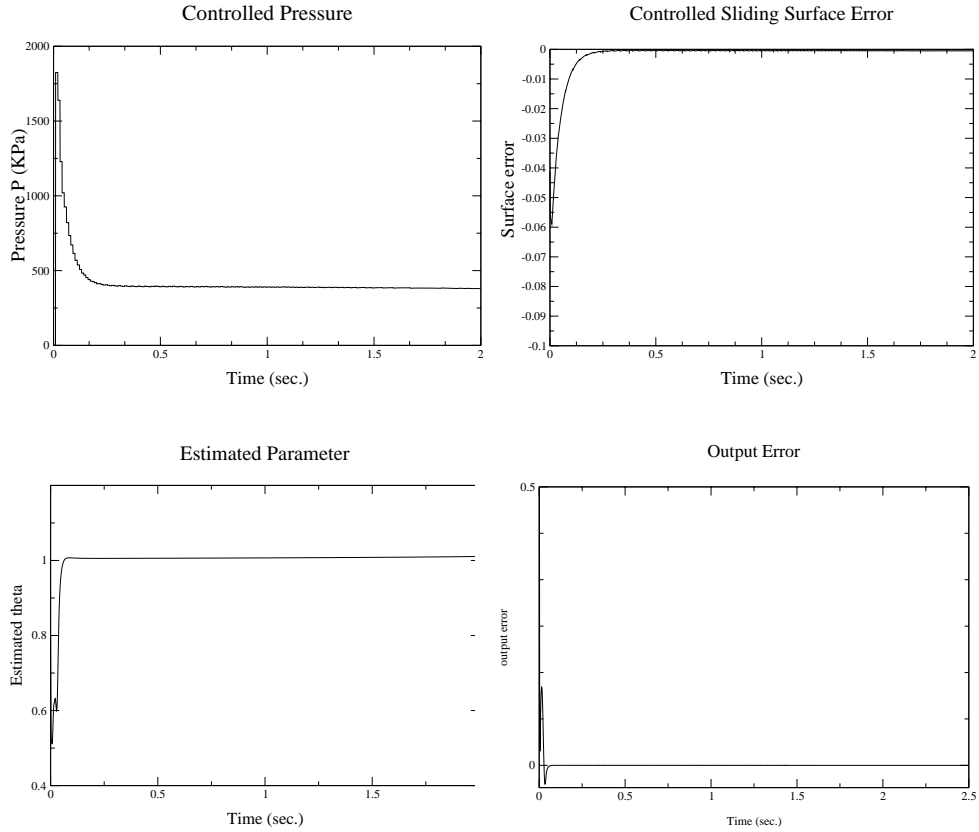
Figure 5.15: (a) Controlled braking pressure P; (b) sliding surface $\tilde{s}$; (c) Estimated friction parameter $\hat{\theta}$; (d) measurement error $\tilde{y}$ (rad/s).
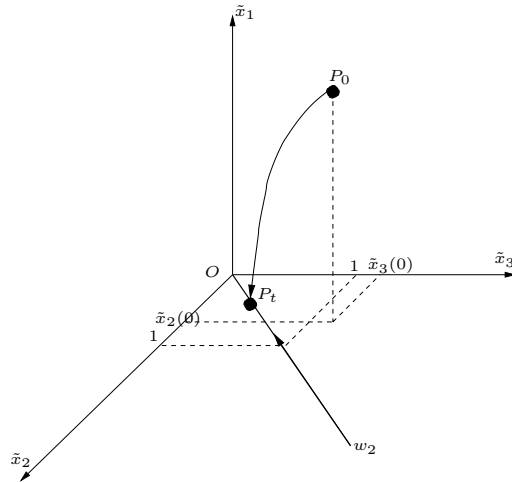
Figure 5.16: A schematic trajectory plot for nonlinear system $\dot{\tilde{\mathbf{x}}} = \bar{A}(x_3)\tilde{\mathbf{x}}$.

converge to w_2 on the $\tilde{x}_2 \times \tilde{x}_3$ plane if $\tilde{x}_2(0) > 0$ and $\tilde{x}_3(0) > 0$, as shown in Fig. 5.16. Thus, if we pick

$$\tilde{x}_2(0) \geq 0, \qquad \tilde{x}_3(0) \geq 0, \tag{5.50}$$

then
$$\max\{\tilde{x}_2(0),\, \tilde{x}_3(0)\} \geq \tilde{x}_2(t) \approx \tilde{x}_3(t) \geq 0, \quad \forall\, t \geq t_0\,,$$
where t_0 is fairly small and depends on the convergence rate and initial conditions of $\tilde{x}_1(t)$.

When the wheel angular velocity is the only measurement available to the control system and a state observer is designed, the angular velocity estimation error can be expressed as:

$$\tilde{\omega} = \omega - \hat{\omega} = \frac{1}{r}(x_2 - x_3) - \frac{1}{r}(\hat{x}_2 - \hat{x}_3) = \frac{1}{r}(\tilde{x}_2 - \tilde{x}_3) \tag{5.51}$$

It should be noticed that $\tilde{\omega} = 0$ does not imply that $\tilde{x}_2 = \tilde{x}_3 = 0$ but that $\tilde{x}_2 = \tilde{x}_3$. Vector w_2 in Fig. 5.16 belongs to the surface where $\tilde{\omega} = 0$. It is important to remark that this limitation obeys the relation between x_2 and x_3 and is not dependent on the dynamic friction model or observer structure that was used in this section.

Note that, by Theorem 5.1, we obtained $\hat{\lambda} \to \hat{\lambda}_{max}$ and $\lambda \to \lambda_{max}$, due to the fact $\hat{\mathbf{x}} \to \mathbf{x}$. However, since the states $\hat{x}_3$ and $\hat{x}_2$ converge slowly, there will be some error between λ and $\hat{\lambda}$. This error can be estimated as follows.

$$
\begin{aligned}
0 < \lambda(t) - \hat{\lambda}(t) \;\; &= \;\; \frac{x_3}{x_2} - \frac{\hat{x}_3}{\hat{x}_2} = \frac{x_2\tilde{x}_3 - x_3\tilde{x}_2}{x_2\hat{x}_2} \\
&\approx \;\; \frac{(x_2 - x_3)\tilde{x}_2}{x_2\hat{x}_2} = \left(1 - \frac{x_3}{x_2}\right)\frac{\tilde{x}_2}{\hat{x}_2} \qquad\qquad\qquad (5.52)\\
&\leq \;\; (1 - \lambda(t))\frac{\lambda(0)x_2(0)}{\hat{x}_2(t)}, \quad \forall\, t \geq t_0\,. \qquad\qquad (5.53)
\end{aligned}
$$

Note that in general $\lambda(0) \leq 3\%$ during normal driving conditions before braking. As a consequence, the slip estimate error is small. Similarly, it can be shown that $\lambda_{max} - \hat{\lambda}_{max}$ will also be small after the state $\tilde{x}_1 \to 0$. Therefore, the proposed control system will achieve a near maximum deceleration level, in spite of the fact that state estimation errors $\tilde{x}_2$ and $\tilde{x}_3$ converge slowly.

Remark 5.8 It should be noticed that with this controller design, we can always guarantee an underestimation of longitudinal slip $\lambda(t)$ as shown in Eq. (5.53). This is a very important property, which helps to preserve vehicle safety and stability on the highway, since the safe inter-vehicle spacing depends on the estimate of maximum acceleration and deceleration.

5.3 Adaptive Observer-based Emergency Braking Control with Underestimation of Friction Coefficient

In the previous section, we discussed the use of the LuGre dynamic friction model in the estimation of the tire/road friction coefficient and the design of an emergency braking controller. Using only the wheel angular velocity, we analytically and numerically showed that an observer-based adaptive emergency braking controller can achieve approximate maximum deceleration. However, we observed that the convergence rate of the estimated vehicle and relative velocities is slow. Moreover, in the previous chapter the variations of the tire and road conditions were modeled with a single parameter θ, which is not realistic. In this chapter, we investigate an alternative enhancement to estimate the tire/road friction and design an emergency braking controller under various tire and road conditions.

5.3.1 Motivation

The goal of this chapter is to extend the approach of the previous chapter. In the previous chapter we addressed the problem of the slow convergence of the estimated vehicle velocity and relative velocity due to the structure of the system. It was also assumed that the friction parameters (σ_i's, $i = 0, 1, 2$) required by the LuGre dynamic friction model are known. In this chapter this assumption is relaxed by the construction of a parameter adaptation law that, by using both the angular velocity measurement of the wheel and vehicle longitudinal acceleration information, also overcomes the slow convergence problem. Underestimation of the friction coefficient, a very desirable feature from the safety point of view, is guaranteed by the proper choice of the parameter adaptation gains and initial conditions of the estimated parameters.

5.3.2 System dynamics

In this chapter, we consider a vehicle system with the following assumptions:

Assumption 5.4
  1. *A lumped LuGre friction model is employed for tire/road friction. The model parameters σ_i are unknown.*
  2. *The normal forces acting on the tires are constant and evenly distributed, and the braking forces are equal for all tires.*
  3. *The friction internal state z and the vehicle velocity v are unknown. The wheel angular velocity ω and the vehicle acceleration $\dot{v}$ are measurable.*
  4. *The road is flat, i.e. the slope of the road is zero.*

A quarter vehicle model is used and a modified lumped LuGre friction model is considered as follows:

$$\dot{z} = v_r - \frac{\sigma_0 |v_r|}{h(v_r)} z \tag{5.54a}$$

$$J\dot{\omega} = rF_x - u_\tau \tag{5.54b}$$

$$m\dot{v} = -4F_x - F_{av}, \tag{5.54c}$$

where z is the friction internal state, $v_r = v - r\omega$ is the relative velocity, $h(v_r)$, μ_{st}, μ_c, v_s are the same model parameters as in the previous chapter and assumed known, u_τ is the traction/braking torque, F_x is the traction/braking force given by the tire/road contact, F_{av} the aerodynamic force, m the vehicle mass, and J the tire rotational inertia. Compared with the dynamics (5.23), we neglect the parameter θ used in the previous chapter. Instead, we consider a general approach with unknown parameters σ_i's [11].

The braking force F_x is given by

$$F_x = (\sigma_0 z + \sigma_1 \dot{z} + \sigma_2 v_r)F_z, \tag{5.55}$$

and similarly the aerodynamic force can be modeled as

$$F_{av} = C_{av} v^2.$$

---

[11]The parameter θ can be absorbed in σ_0.

88

Substituting above Equation into (5.54c) and considering $v_r = v - r\omega$ as the state variable, we can rewrite Eqs (5.54b) and (5.54c) as

$$\dot{v} = -c\,\mu - d\,v^2 \,, \tag{5.56a}$$

$$\dot{v}_r = -(a+c)\,\mu - dv^2 + e\,K_b P_b \tag{5.56b}$$

with $a = r^2 mg/4J$, $c = g$, $d = C_{av}/m$ and $e = r/J$. As in the previous chapter, the braking torque is approximated by $u_\tau = K_b P_b$, where K_b is an overall braking system gain and P_b the master cylinder pressure. We utilize the following assumptions for the compensator design:

Assumption 5.5

1. *The brake system gain K_b is known.*
2. *The velocity v and relative velocity v_r are uniformly continuous functions of time t.*

5.3.3 Compensator design

Velocity observer

Assuming that the wheel angular velocity ω and vehicle longitudinal acceleration $\dot{v}$ are known, it is possible to propose an observer for the vehicle velocity v

$$\dot{\hat{v}} = -c\mu - d\hat{v}^2 + L_3 \tilde{y}_2 \,, \tag{5.57}$$

where $\tilde{y}_2 := \dot{v} - \dot{\hat{v}} = -d\tilde{v}(v + \hat{v})$ with $\dot{\hat{v}} := -c\mu - d\hat{v}^2$, and $L_3 \in \mathbb{R}$ is the observer gain.

The velocity estimation error dynamics are

$$\dot{\tilde{v}} = -d\tilde{v}(v + \hat{v})(1 - L_3)\,. \tag{5.58}$$

Define the Lyapunov candidate function

$$W_1 = \frac{1}{2}\tilde{v}^2\,. \tag{5.59}$$

Its time derivative is

$$\dot{W}_1 = \tilde{v}\dot{\tilde{v}} = -d\tilde{v}^2(v + \hat{v})(1 - L_3) \leq 0\,.$$

Lemma 5.1 *Assume $L < 0$, then $\tilde{v}(0) < 0 \Rightarrow \tilde{v}(t) < 0$, $\forall t \geq 0$ or $\tilde{v}(0) > 0 \Rightarrow \tilde{v}(t) > 0$, $\forall t \geq 0$.*

Proof: For any given value of v and $\hat{v}$ the solution to Eq. (5.58) is of the form

$$\tilde{v}(t) = \tilde{v}(0)e^{-(1-L)\int_0^t d(v+\hat{v})d\tau} \tag{5.60}$$

This term will never change sign, therefore if $\tilde{v}(0) < 0 \Rightarrow \tilde{v}(t) < 0$, $\forall t \geq 0$ or if $\tilde{v}(0) > 0 \Rightarrow \tilde{v}(t) > 0$, $\forall t \geq 0$ ∎

From Lemma 5.1, if $L_3 < 0$, then $\tilde{v}(t)$ is the same sign as $\tilde{v}(0)$.

Remark 5.9 Lemma 5.1 implies $\dot{W}_1 < 0$ and asymptotic stability of $\tilde{v} = 0$ follows. Moreover, if we choose the observer gain $|L_3|$ large we can let the estimated velocity $\hat{v}$ converge to the true value v quickly.

Internal state observer and parameter estimation

First notice that, by substituting Eq. (5.54a) into Eq. (5.55) and we obtain

$$\mu = \sigma_0 z + \sigma_1 \left[v_r - \sigma_0 f(v_r)z\right] - \sigma_2 v_r = \sigma_0 z - \sigma_3 f(v_r)z + \sigma_4 v_r \,, \tag{5.61}$$

where $\sigma_3 = \sigma_0 \sigma_1$, $\sigma_4 = \sigma_1 - \sigma_2$ and $f(v_r) = v_r/h(v_r)$. This expression is linear in the parameters σ_0, σ_3 and σ_4, i.e.,

$$\mu = \begin{bmatrix} z & -f(v_r)z & v_r \end{bmatrix} \begin{bmatrix} \sigma_0 \\ \sigma_3 \\ \sigma_4 \end{bmatrix} = \mathbf{V}\mathbf{\Xi} \,, \tag{5.62}$$

where $\mathbf{V} := \begin{bmatrix} z & -f(v_r)z & v_r \end{bmatrix}$ and $\mathbf{\Xi} := [\sigma_0 \ \sigma_3 \ \sigma_4]^T$.

Consider the following observer for the internal state z

$$\dot{\hat{z}} = \hat{v}_r - \hat{\sigma}_0 f(\hat{v}_r)\hat{z} \tag{5.63}$$

and a gradient type parameter adaptation law

$$\dot{\hat{\mathbf{\Xi}}} = -\Gamma \hat{\mathbf{V}}^T \tilde{\mu} \,, \tag{5.64}$$

where $\Gamma = \mathrm{diag}(\gamma_0, \gamma_3, \gamma_4) > 0$ is a diagonal matrix of adaptation gains, $\hat{\mathbf{V}}$ is the regressor in Eq. (5.62) evaluated at the estimated quantities, i.e.

$$\hat{\mathbf{V}} = \begin{bmatrix} \hat{z} & -f(\hat{v}_r)\hat{z} & \hat{v}_r \end{bmatrix} \,,$$

and $\tilde{\mu}$ is defined by

$$\tilde{\mu} = \mathbf{V}\mathbf{\Xi} - \hat{\mathbf{V}}\hat{\mathbf{\Xi}} = \hat{\mathbf{V}}\tilde{\mathbf{\Xi}} + \tilde{\mathbf{V}}\mathbf{\Xi} \,, \tag{5.65}$$

with $\tilde{\mathbf{V}} = \mathbf{V} - \hat{\mathbf{V}}$. $\tilde{\mu} = \mu - \hat{\mu}$ is defined as the error of the friction coefficient. Note that the friction coefficient μ is calculated by the dynamics (5.54b) as

$$\mu = -\frac{J\dot{\omega} + eK_b P_b}{f} \,, \tag{5.66}$$

with $f = mgr/4$ and assumption that we can measure the angular acceleration and the braking pressure.

Developing Eq. (5.65)

$$\tilde{\mu} = \begin{bmatrix} \hat{z} & -f(\hat{v}_r)\hat{z} & \hat{v}_r \end{bmatrix} \begin{bmatrix} \tilde{\sigma}_0 \\ \tilde{\sigma}_3 \\ \tilde{\sigma}_4 \end{bmatrix} + \begin{bmatrix} \tilde{z} & -f(v_r)z + f(\hat{v}_r)\hat{z} & \tilde{v}_r \end{bmatrix} \begin{bmatrix} \sigma_0 \\ \sigma_3 \\ \sigma_4 \end{bmatrix}$$

$$= [\sigma_0 - \sigma_3 f(v_r)]\, \tilde{z} + \hat{z}\tilde{\sigma}_0 - f(\hat{v}_r)\hat{z}\tilde{\sigma}_3 + \hat{v}_r\tilde{\sigma}_4 + \sigma_4\tilde{v}_r - \sigma_3\hat{z}\left[f(v_r) - f(\hat{v}_r)\right] \,. \tag{5.67}$$

The term $f(v_r) - f(\hat{v}_r)$ can be expanded in a Taylor series about v_r. This yields

$$f(v_r) - f(\hat{v}_r) = \frac{df(v_r)}{dv_r}\tilde{v}_r = \frac{df(v_r)}{dv_r}\tilde{v}, \tag{5.68}$$

where the last expression was derived using the fact that $v_r = v - r\omega$ and $\hat{v}_r = \hat{v} - r\omega$, therefore $\tilde{v}_r = v_r - \hat{v}_r = \tilde{v}$. Substituting Eq. (5.68) in Eq. (5.67)

$$\tilde{\mu} = [\sigma_0 - \sigma_3 f(v_r)]\,\tilde{z} + \hat{z}\tilde{\sigma}_0 - f(\hat{v}_r)\hat{z}\tilde{\sigma}_3 + \hat{v}_r\tilde{\sigma}_4 + [\sigma_4 - \sigma_3\hat{z}f'(v_r)]\,\tilde{v} \tag{5.69}$$

with $f'(v_r) = df(v_r)/dv_r$.

The error dynamics of $\tilde{z}$ from Eqs. (5.54a) and (5.63) are given by

$$\dot{\tilde{z}} = [1 - \sigma_0 f'(v_r)\hat{z}]\,\tilde{v} - \sigma_0 f(v_r)\tilde{z} - f(\hat{v}_r)\hat{z}\tilde{\sigma}_0. \tag{5.70}$$

Controller design

Note that the internal friction state z and the vehicle longitudinal velocity v are assumed not to be measurable, and the model parameters σ_i, $i = 0, 1, 2$, are unknown. It is therefore difficult to obtain λ_{max} for the current conditions by Eq. (5.17) [12]. By constructing an observer and an adaptation law to estimate these variables, near maximum deceleration can be achieved around $\hat{\lambda}_{max}$. $\hat{\lambda}_{max}$ can be determined from the estimated velocity ($\hat{v}$) and parameters ($\hat{\sigma}_i$'s), i.e.

$$\hat{\lambda}_{max} = \arg\max_{\hat{v},\lambda,\hat{\sigma}_i} \{\hat{\mu}(\lambda, \hat{v}, \hat{\sigma}_i)\}. \tag{5.71}$$

if we can guarantee that $\hat{v} \to v$ and $\hat{\sigma}_i \to \sigma_i$, $i = 0, 3, 4$.

To continue with the controller design, it is necessary to set the value for the pressure of the master cylinder, P_b. For this purpose define

$$\tilde{s} = \hat{v}_r - \hat{\lambda}_{max}\hat{v} = \hat{v}(1 - \hat{\lambda}_{max}) - r\omega \tag{5.72}$$

as the desired relative velocity for the emergency braking maneuver. In this expression $\tilde{s} = \hat{v}_r - R\omega$ and $\hat{\lambda}_{max}$ is the estimated value of λ_{max} by Eq. (5.17) based on the current estimation of $\hat{\Xi}$ and $\hat{v}$. Taking the time derivative of Eq. (5.72)

$$\begin{aligned}\dot{\tilde{s}} &= \dot{\hat{v}}(1 - \hat{\lambda}_{max}) - r\dot{\omega} - \hat{v}\dot{\hat{\lambda}}_{max} \\ &= \dot{\hat{v}}(1 - \hat{\lambda}_{max}) - \frac{rf}{J}\mu + \frac{reK_bP_b}{J} - \hat{v}\frac{\partial\hat{\lambda}_{max}}{\partial\hat{v}}\dot{\hat{v}} - \hat{v}\frac{\partial\hat{\lambda}_{max}}{\partial\omega}\dot{\omega}.\end{aligned} \tag{5.73}$$

The partial derivatives of λ_{max} can be calculated numerically. Choosing

$$P_b = \frac{J}{reK_b}\left[-\dot{\hat{v}}(1 - \hat{\lambda}_{max}) + \frac{rf}{J}\mu + \hat{v}\frac{\partial\hat{\lambda}_{max}}{\partial\hat{v}}\dot{\hat{v}} + \hat{v}\frac{\partial\hat{\lambda}_{max}}{\partial\omega}\dot{\omega} - \zeta\bar{s}\right], \tag{5.74}$$

where $\zeta > 0$ a gain and substituting in Eq. (5.73) gives

$$\dot{\tilde{s}} = -\zeta\tilde{s}. \tag{5.75}$$

---

[12]In this case, we should set $\theta = 1$ in the Eq. (5.17) for estimation of λ_{max} since θ is not introduced in this chapter.

Define the following Lyapunov function candidate

$$W_4 = \frac{1}{2}\tilde{s}^2 \tag{5.76}$$

Taking the time derivative of Eq. (5.76) and using Eq. (5.75)

$$\dot{W}_4 = -\zeta\tilde{s}^2 \le 0. \tag{5.77}$$

The asymptotic stability of $\tilde{s} = 0$ follows.

Combined stability analysis

Consider, in addition to Eq. (5.59), the following set of Lyapunov function candidates

$$W_2 = \frac{1}{2}\tilde{z}^2 \tag{5.78}$$

$$W_3 = \frac{1}{2}\tilde{\Xi}^T\Gamma^{-1}\tilde{\Xi} \tag{5.79}$$

and define now the composite Lyapunov function candidate

$$W = W_1 + W_2 + W_3 = \sum_{i=1}^{3} W_i. \tag{5.80}$$

The time derivative of Eq. (5.80) can be written as

$$\dot{W} = \tilde{v}\dot{\tilde{v}} + \tilde{z}\dot{\tilde{z}} + \tilde{\Xi}^T\Gamma^{-1}\dot{\tilde{\Xi}}. \tag{5.81}$$

Using the observer error dynamics and parameter adaptation law in Eqs. (5.58), (5.70) and (5.64), Eq. (5.81) becomes

$$\dot{W} = -d(v+\hat{v})(1-L)\tilde{v}^2 + \tilde{z}\left[(1-\sigma_0 f'(v_r)\hat{z})\tilde{v} - \sigma_0 f(v_r)\tilde{z} - f(\hat{v}_r)\tilde{z}\tilde{\sigma}_0\right]$$
$$- (\tilde{\Xi}^T\hat{\mathbf{V}}^T\hat{\mathbf{V}}\tilde{\Xi} + \tilde{\Xi}^T\hat{\mathbf{V}}^T\tilde{\mathbf{V}}\Xi). \tag{5.82}$$

The term $\tilde{\mathbf{V}}$ can be expressed as

$$\tilde{\mathbf{V}} = [0 \quad -f'(v_r)\hat{z} \quad 1]\tilde{v} + [1 \quad -f(v_r) \quad 0]\tilde{z} = \mathbf{V}_1\tilde{v} + \mathbf{V}_2\tilde{z}, \tag{5.83}$$

where $\mathbf{V}_1 = [0 \quad -f'(v_r)\hat{z} \quad 1]$ and $\mathbf{V}_2 = [1 \quad -f(v_r) \quad 0]$. Using Eq. (5.83), Eq. (5.82) can be written as a quadratic form

$$\dot{W} = -\begin{bmatrix} \tilde{\Xi} & \tilde{z} & \tilde{v} \end{bmatrix}\begin{bmatrix} \hat{\mathbf{V}}^T\hat{\mathbf{V}} & \hat{\mathbf{V}}^T\mathbf{V}_2\Xi & \hat{\mathbf{V}}^T\mathbf{V}_1\Xi \\ \mathbf{V}_3 & \sigma_0 f(v_r) & -(1-\sigma_0 f'(v_r)\hat{z}) \\ \mathbf{0} & 0 & d(1-L_3)(v+\hat{v}) \end{bmatrix}\begin{bmatrix} \tilde{\Xi} \\ \tilde{z} \\ \tilde{v} \end{bmatrix} = -\mathbf{\Phi}^T\mathbf{M}\mathbf{\Phi}, \tag{5.84}$$

where $\boldsymbol{\Phi} = \begin{bmatrix} \tilde{\boldsymbol{\Xi}} & \tilde{z} & \tilde{v} \end{bmatrix}^T = \begin{bmatrix} \tilde{\sigma}_0 & \tilde{\sigma}_4 & \tilde{\sigma}_4 & \tilde{z} & \tilde{v} \end{bmatrix}^T$, $\mathbf{V}_3 = [f(\hat{v}_r)\hat{z} \ \ 0 \ \ 0]$ and

$$\mathbf{M} = \begin{bmatrix} \hat{z}^2 & -\hat{z}^2 f(\hat{v}_r) & \hat{z}\hat{v}_r & w_1\hat{z} & w_2\hat{z} \\ -\hat{z}^2 f(\hat{v}_r) & \hat{z}^2 f^2(\hat{v}_r) & -\hat{z} f(\hat{v}_r)\hat{v}_r & -w_1\hat{z} f(\hat{v}_r) & -w_2\hat{z} f(\hat{v}_r) \\ \hat{z}\hat{v}_r & -\hat{z} f(\hat{v}_r)\hat{v}_r & \hat{v}_r^2 & w_1\hat{v}_r & w_2\hat{v}_r \\ \hat{z} f(\hat{v}_r) & 0 & 0 & \sigma_0 f(v_r) & -w_3 \\ 0 & 0 & 0 & 0 & w_4 \end{bmatrix}$$

with $w_1 = \sigma_0 - \sigma_3 f(v_r)$, $w_2 = \sigma_4 - \sigma_3 f'(v_r)\hat{z}$, $w_3 = 1 - \sigma_0 f'(v_r)\hat{z}$ and $w_4 = d(1 - L_3)(v + \hat{v})$.

Note that

$$\mathbf{M} = \frac{\mathbf{M} + \mathbf{M}^T}{2} + \frac{\mathbf{M} - \mathbf{M}^T}{2} = \mathbf{M}_1 + \mathbf{M}_2 \,,$$

where $\mathbf{M}_1 = \mathbf{M}_1^T = \frac{\mathbf{M} + \mathbf{M}^T}{2}$ is a symmetric matrix and $\mathbf{M}_2 = -\mathbf{M}_2^T = \frac{\mathbf{M} - \mathbf{M}^T}{2}$ is a skew-symmetric matrix. Thus, Eq. (5.84) becomes

$$\dot{W} = -\boldsymbol{\Phi}^T \mathbf{M}_1 \boldsymbol{\Phi} - \boldsymbol{\Phi}^T \mathbf{M}_2 \boldsymbol{\Phi} = -\boldsymbol{\Phi}^T \mathbf{M}_1 \boldsymbol{\Phi} \,.$$

The last equality comes from the fact that $\boldsymbol{\Phi}^T \mathbf{M}_2 \boldsymbol{\Phi} = 0$. It can be directly shown that the symmetric matrix $\mathbf{M}_1$ is positive semi-definite:

$$\mathbf{M}_1 = \begin{bmatrix} \hat{z}^2 & -\hat{z}^2 f(\hat{v}_r) & \hat{z}\hat{v}_r & \frac{1}{2}\hat{z}(w_1 + f(\hat{v}_r)) & \frac{1}{2}\hat{z}w_2 \\ -\hat{z}^2 f(\hat{v}_r) & \hat{z}^2 f^2(\hat{v}_r) & -\hat{z} f(\hat{v}_r)\hat{v}_r & -\frac{1}{2}\hat{z}w_1 f(\hat{v}_r) & -\frac{1}{2}w_2\hat{z} f(\hat{v}_r) \\ \hat{z}\hat{v}_r & -\hat{z} f(\hat{v}_r)\hat{v}_r & \hat{v}_r^2 & \frac{1}{2}w_1\hat{v}_r & \frac{1}{2}w_2\hat{v}_r \\ \frac{1}{2}\hat{z}(w_1 + f(\hat{v}_r)) & -\frac{1}{2}\hat{z}w_1 f(\hat{v}_r) & \frac{1}{2}w_1\hat{v}_r & \sigma_0 f(v_r) & -\frac{1}{2}w_3 \\ \frac{1}{2}\hat{z}w_2 & -\frac{1}{2}w_2\hat{z} f(\hat{v}_r) & \frac{1}{2}w_2\hat{v}_r & -\frac{1}{2}w_3 & w_4 \end{bmatrix} \geq 0 \tag{5.85}$$

by the fact that

$$\det \mathbf{M}_1(1, 1) = \hat{z}^2 > 0, \qquad \det \mathbf{M}_1(1:j, 1:j) = 0, \quad \text{for } j = 2, 3, 4, 5.$$

From Eq. (5.85) we know that

$$\dot{W} = -\boldsymbol{\Phi}^T \mathbf{M}_1 \boldsymbol{\Phi} \leq 0 \,,$$

which corresponds to Eq. (5.84) being positive semi-definite. The stability of $\tilde{v} = 0$, $\tilde{z} = 0$ and $\tilde{\boldsymbol{\Xi}} = \mathbf{0}$ follows. Moreover, $\hat{v}$, $\hat{z}$ and $\tilde{\boldsymbol{\Xi}}$ are bounded. Using Barbalat's Lemma it is possible to show that $\lim_{t \to \infty} \tilde{v}(t) = 0$. Convergence of $\tilde{z} = 0$ and $\tilde{\boldsymbol{\Xi}} = \mathbf{0}$ cannot be guaranteed if there is no persistence of excitation. In this case the reachable equilibria satisfy

$$\sigma_0 \tilde{z}\left(\frac{w_1}{\sigma_0} - 1\right) - \hat{z} f(v_r)\tilde{\sigma}_3 + \hat{v}_r \tilde{\sigma}_4 = 0 \,, \tag{5.86}$$

$$\tilde{z} + \frac{\hat{z}}{\sigma_0}\tilde{\sigma}_0 = 0 \,. \tag{5.87}$$

The above equilibria are calculated through error dynamics of state variables $\tilde{\boldsymbol{\Xi}}$ and $\tilde{z}$ given by Eqs. (5.64), (5.68), and (5.69), assuming quick convergence of estimate of vehicle velocity, i.e. $\tilde{v} = 0$.

Remark 5.10 In the above combined stability analysis we did not include the controller Lyapunov candidate W_4 because the controlled target error $\tilde{s}$ given by (5.72) is decoupled from the observer and parameter adaptation errors $\tilde{\Xi}$, $\tilde{z}$, and $\tilde{v}$. Therefore, we analyze the stability of the controller separately from the observers and the parameter estimators.

5.3.4 Underestimation of the friction coefficient

A very desirable feature to be attained with the observer and adaptive scheme in Eqs. (5.58), (5.64) and (5.70) is the underestimation of the maximum coefficient of friction, μ_{max}. This underestimation provides conservative estimates for the inter-vehicle distance that will yield safe emergency braking maneuvers.

From Eq. (5.61) it is clear that

$$\tilde{\sigma}_0(t) \geq 0, \quad \tilde{\sigma}_3(t) \leq 0, \quad \text{and} \quad \tilde{\sigma}_4(t) \geq 0 \tag{5.88}$$

will produce this desired underestimation of μ_{max}, i.e. $\hat{\mu}_{max}(t) \leq \mu_{max}(t)$ provided that

Assumption 5.6
1. *The estimated state variables $\hat{v}$ and $\hat{z}$ converge to the true states quickly and*
2. *$z \geq 0$, $v_r \geq 0$ and $f(v_r) \geq 0$.*

Remark 5.11 To justify the first condition in Assumption 5.6, we recall the error dynamics of state variables $\tilde{v}$ and $\tilde{z}$ given by Eqs. (5.58) and (5.69), respectively. By choosing a large observer gain L_3 we can guarantee the quick convergence of $\hat{v}$ by Lemma 5.1. The quick convergence rate of estimated state $\hat{z}$ follows from Eq. (5.69), and facts that σ_0 is large, $\tilde{v} \to 0$ and $\hat{z}$, $\hat{\Xi}$ are bounded. The second condition in Assumption 5.6 follows directly from the definition of v_r, $f(v_r)$ and Property 5.1.

In this section we assume that

Assumption 5.7
1. *$\tilde{\sigma}_0(0) > 0$, $\tilde{\sigma}_3(0) < 0$ and $\tilde{\sigma}_4(0) > 0$.*
2. *$v(t) \geq v_{min}$, $\forall t \geq 0$*

Under these assumptions, the structure of the system composed by $\tilde{\sigma}_0$, $\tilde{\sigma}_3$ and $\tilde{\sigma}_4$ is

$$\begin{bmatrix} \dot{\tilde{\sigma}}_0 \\ \dot{\tilde{\sigma}}_3 \\ \dot{\tilde{\sigma}}_4 \end{bmatrix} = \begin{bmatrix} -\gamma_0 \hat{z}^2 & \gamma_0 f(v_r)\hat{z}^2 & -\gamma_0 \hat{z}v_r \\ \gamma_3 f(v_r)\hat{z}^2 & -\gamma_3 f^2(v_r)\hat{z}^2 & \gamma_3 f(v_r)\hat{z}v_r \\ -\gamma_4 \hat{z}v_r & \gamma_4 f(v_r)\hat{z}v_r & -\gamma_4 v_r^2 \end{bmatrix} \begin{bmatrix} \tilde{\sigma}_0 \\ \tilde{\sigma}_3 \\ \tilde{\sigma}_4 \end{bmatrix}. \tag{5.89}$$

For simplicity, consider the system in Eq. (5.89) as time invariant in order to find an approximate condition for underestimation of friction coefficient μ. The solution, with initial conditions $\tilde{\sigma}_0(0)$,

$\tilde{\sigma}_3(0)$ and $\tilde{\sigma}_4(0)$, is

$$\tilde{\sigma}_0(t) = \frac{1}{\beta} \left[(\gamma_0 \hat{z}^2 e^{-\beta t} + \gamma_3 \hat{z}^2 f^2(v_r) + \gamma_4 v_r^2) \tilde{\sigma}_0(0) + \right.$$
$$\left. (1 - e^{-\beta t}) \gamma_0 \hat{z}^2 f(v_r) \tilde{\sigma}_3(0) + (1 - e^{-\beta t}) \gamma_4 v_r^2 \tilde{\sigma}_4(0) \right] \tag{5.90a}$$

$$\tilde{\sigma}_3(t) = \frac{1}{\beta} \left[(1 - e^{-\beta t}) \gamma_3 \hat{z}^2 f(v_r) \tilde{\sigma}_0(0) + (\alpha \gamma_0 \hat{z}^2 + \gamma_4 v_r^2 + \gamma_3 \hat{z}^2 f^2(v_r) e^{-\beta t}) \tilde{\sigma}_3(0) - \right.$$
$$\left. \left((1 - e^{-\beta t}) \gamma_3 \gamma_4 v_r^2 / \gamma_0 \right) \tilde{\sigma}_4(0) \right] \tag{5.90b}$$

$$\tilde{\sigma}_4(t) = \frac{1}{\beta} \left[(1 - e^{-\beta t}) \gamma_0 \hat{z}^2 \tilde{\sigma}_0(0) - (1 - e^{-\beta t}) \gamma_0 \hat{z}^2 f(v_r) \tilde{\sigma}_3(0) + (\gamma_0 \hat{z}^2 + \right.$$
$$\left. \gamma_3 \hat{z}^2 f^2(v_r) + \gamma_4 v_r^2 e^{-\beta t}) \tilde{\sigma}_4(0) \right] , \tag{5.90c}$$

where $\beta = \gamma_0 \hat{z}^2 + \gamma_3 \hat{z}^2 f^2(v_r) + \gamma_4 v_r^2$.

Lemma 5.2 *Assume that Lemma 5.1 and Assumption 5.7 hold, then there exist gains γ_0, γ_3 and γ_4 such that if the following conditions are satisfied*

$$\left(\gamma_0 + \gamma_4 \frac{v_r^2}{\hat{z}^2} \right) |\tilde{\sigma}_3(0)| \geq \gamma_3 f(v_r) \tilde{\sigma}_0(0) \geq \gamma_0 |\tilde{\sigma}_3(0)| , \tag{5.91}$$

then $\tilde{\sigma}_0(t) \geq 0$, $\tilde{\sigma}_3(t) \leq 0$ and $\tilde{\sigma}_4(t) \geq 0$, $\forall t \geq 0$.

Proof: First assume that t is close to 0, then the evolution of $\tilde{\sigma}_0(t)$, $\tilde{\sigma}_3(t)$ and $\tilde{\sigma}_4(t)$ is dominated by $\tilde{\sigma}_0(0) > 0$, $\tilde{\sigma}_3(0) < 0$ and $\tilde{\sigma}_4(0) > 0$ because the term $(1 - e^{-\beta t})$ can be neglected. Now assume the worst possible case, which happens if $t \gg 0$. In this situation for $\tilde{\sigma}_0(t)$ to remain positive, according to Eq. (5.90a), it is necessary that

$$\left(\gamma_3 \hat{z}^2 f^2(v_r) + \gamma_4 v_r^2 \right) \tilde{\sigma}_0(0) + \gamma_4 v_r^2 \tilde{\sigma}_4(0) \geq \gamma_0 \hat{z}^2 f(v_r) |\tilde{\sigma}_3(0)| . \tag{5.92}$$

Ineq. (5.92) will hold if

$$\gamma_3 \hat{z}^2 f(v_r) \tilde{\sigma}_0(0) \geq \gamma_0 \hat{z}^2 f(v_r) |\tilde{\sigma}_3(0)| , \tag{5.93}$$

which is precisely the second inequality in Ineq. (5.91). Similarly, according to Eq. (5.90b), for $\tilde{\sigma}_3(t)$ to remain negative it is necessary that

$$\left(\gamma_0 \hat{z}^2 + \gamma_4 v_r^2 \right) |\tilde{\sigma}_3(0)| + \frac{\gamma_3 \gamma_4}{\gamma_0} v_r^2 \tilde{\sigma}_4(0) \geq \gamma_3 \hat{z}^2 f(v_r) \tilde{\sigma}_0(0) . \tag{5.94}$$

Ineq. (5.94) will hold in turn if

$$\left(\gamma_0 \hat{z}^2 + \gamma_4 v_r^2 \right) |\tilde{\sigma}_3(0)| \geq \gamma_3 \hat{z}^2 f(v_r) \tilde{\sigma}_0(0) , \tag{5.95}$$

which is the first inequality in Ineq. (5.91). According to Eq. (5.90c), $\tilde{\sigma}_4(0)$ will always remain positive. ∎

Finally, the main result of this chapter is stated in the following theorem:

Theorem 5.2 *Consider Assumption 5.7 and Lemmas 5.1 and 5.2, then under the observer and adaptation laws in Eqs. (5.57), (5.63) and (5.64) the equilibrium $\tilde{v} = 0$, $\tilde{z} = 0$ and $\tilde{\mathbf{\Xi}} = \mathbf{0}$ is stable. Moreover, the maximum coefficient of friction μ_{max} is underestimated and $\lim_{t\to\infty} \tilde{v}(t) = 0$, $\lim_{t\to\infty} \tilde{z}(t) = 0$ and $\lim_{t\to\infty} \tilde{\mathbf{\Xi}} = \mathbf{0}$.*

Proof: The choice of $\tilde{z}(0) < 0$, $\tilde{\sigma}_0(0) > 0$, $\tilde{\sigma}_3(0) < 0$ and $\tilde{\sigma}_4(0) > 0$ together with Lemma 5.2 implies that $\hat{\mathbf{V}}\tilde{\mathbf{\Xi}} \geq 0$ and therefore that that the product $\tilde{\mathbf{\Xi}}^T\hat{\mathbf{V}}^T\hat{\mathbf{V}}\tilde{\mathbf{\Xi}}$ does not vanish, except when $\tilde{\mathbf{\Xi}} = \mathbf{0}$.

Choose Lyapunov function candidate V as

$$V = h_1 W_1 + h_2 W_2 + h_3 W_3 = \sum_{i=1}^{3} h_i W_i$$

with h_1, h_2 and h_3 are positive numbers. The time derivative of V satisfies, similar as (5.84),

$$\dot{V} = -\begin{bmatrix} \tilde{\mathbf{\Xi}} & \tilde{z} & \tilde{v} \end{bmatrix} \begin{bmatrix} h_3\hat{\mathbf{V}}^T\hat{\mathbf{V}} & h_3\hat{\mathbf{V}}^T\mathbf{V}_2\mathbf{\Xi} & h_3\hat{\mathbf{V}}^T\mathbf{V}_1\mathbf{\Xi} \\ h_2\mathbf{V}_3 & h_2\sigma_0 f(v_r) & -h_2(1 - \sigma_0 f'(v_r)\hat{z}) \\ \mathbf{0} & 0 & h_1 d(1 - L_3)(v + \hat{v}) \end{bmatrix} \begin{bmatrix} \tilde{\mathbf{\Xi}} \\ \tilde{z} \\ \tilde{v} \end{bmatrix}. \tag{5.96}$$

Eq. (5.96) can be bounded by

$$\dot{V} \leq -\begin{bmatrix} \|\tilde{\mathbf{\Xi}}\| & |\tilde{z}| & |\tilde{v}| \end{bmatrix} \begin{bmatrix} h_3\|\hat{\mathbf{V}}^T\hat{\mathbf{V}}\| & h_3\|\hat{\mathbf{V}}^T\mathbf{V}_2\mathbf{\Xi}\| & h_3\|\hat{\mathbf{V}}^T\mathbf{V}_1\mathbf{\Xi}\| \\ h_2\|\mathbf{V}_3\| & h_2\sigma_0 f(v_r) & -h_2(1 - \sigma_0 f'(v_r)\hat{z}) \\ \mathbf{0} & 0 & h_1 d(1 - L_3)(v + \hat{v}) \end{bmatrix} \begin{bmatrix} \|\tilde{\mathbf{\Xi}}\| \\ |\tilde{z}| \\ |\tilde{v}| \end{bmatrix}$$

$$= -\frac{1}{2}\mathbf{\Psi}^T(\mathbf{HS} + \mathbf{S}^T\mathbf{H})\mathbf{\Psi}, \tag{5.97}$$

where $\mathbf{\Psi} = \begin{bmatrix} \|\tilde{\mathbf{\Xi}}\| & |\tilde{z}| & |\tilde{v}| \end{bmatrix}^T$, $\mathbf{H} = \text{diag}\{h_3,\ h_2,\ h_1\}$ and

$$\mathbf{S} = \begin{bmatrix} \|\hat{\mathbf{V}}^T\hat{\mathbf{V}}\| & \|\hat{\mathbf{V}}^T\mathbf{V}_2\mathbf{\Xi}\| & \|\hat{\mathbf{V}}^T\mathbf{V}_1\mathbf{\Xi}\| \\ \|\mathbf{V}_3\| & \sigma_0 f(v_r) & -(1 - \sigma_0 f'(v_r)\hat{z}) \\ \mathbf{0} & 0 & d(1 - L_3)(v + \hat{v}) \end{bmatrix}. \tag{5.98}$$

According to Khalil (1996) a necessary and sufficient condition for the existence of scalar h_1, h_2 and h_3 that will make Eq. (5.97) negative definite is that the principal minors of the matrix $\mathbf{S}$ are positive definite. The first two minors are proven directly to be positive, the third one, given by

$$d(1 - L_3)(v + \hat{v})\hat{z}^2 f^2(v_r)\sigma_3 \tag{5.99}$$

will be greater or equal to zero provided that conditions on Lemmas 5.1 and 5.2 are satisfied. This proves asymptotic stability and therefore that $\lim_{t\to\infty} \tilde{v}(t) = 0$, $\lim_{t\to\infty} \tilde{z}(t) = 0$ and $\lim_{t\to\infty} \tilde{\mathbf{\Xi}} = \mathbf{0}$.

The underestimation of μ_{max} follows directly from Eq. (5.61) and Lemma 5.2. ∎

96

5.3.5 Simulation results

In this section we will test the design of the previous section. In the simulation we use the parameters from the LeSabre cars used in the California PATH program: $m = 1701.0\ Kg$, $C_{av} = 0.3693\ N \cdot s^2/m^2$, $J = 2.603\ Kg \cdot m^2$, $r = 0.323m$ and the brake coefficient $K_b = 0.9$ as nominal values. Wheel angular velocity and vehicle longitudinal acceleration are used to design an observer-based emergency braking controller. Fig. 5.17 shows the convergence of the dynamic surface for emergency braking maneuver. Fig. 5.18 illustrates the estimated vehicle velocity and relative velocity. From Fig. 5.18, we found that the estimated vehicle relative velocity and vehicle velocity converge to their true values. The estimated internal friction state z is shown in Fig. 5.19. Fig. 5.20 shows the friction coefficient and braking pressure during the emergency braking maneuver. Fig. 5.21 illustrates the estimated friction parameters $\hat{\Xi}$. During the simulation we observed that all of these parameters converged to their true values.
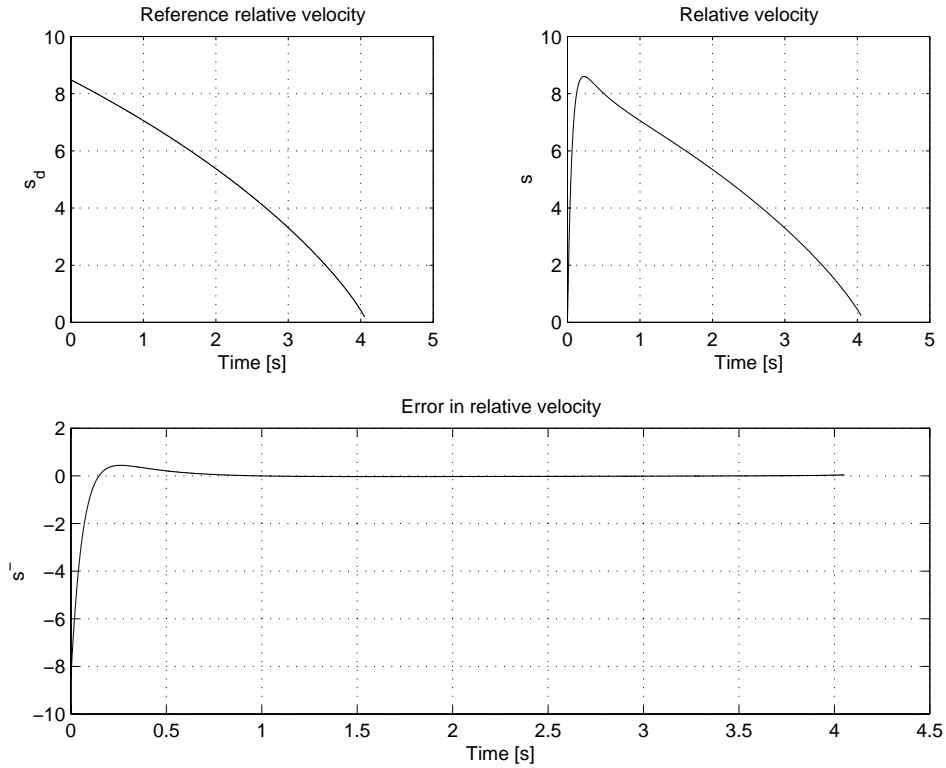

Figure 5.17: Dynamic surface $\tilde{s}$.

The estimated relative velocity and longitudinal vehicle velocity converge to their true values using the observer design in section 5.3.3. This design overcomes the drawback given in the previous chapter using vehicle longitudinal acceleration in addition to the wheel angular velocity.

5.4 Conclusions

In this chapter we discussed emergency braking control under unknown tire/road conditions and brake conditions, based on a dynamic friction model. Throughout the discussion, we used the LuGre
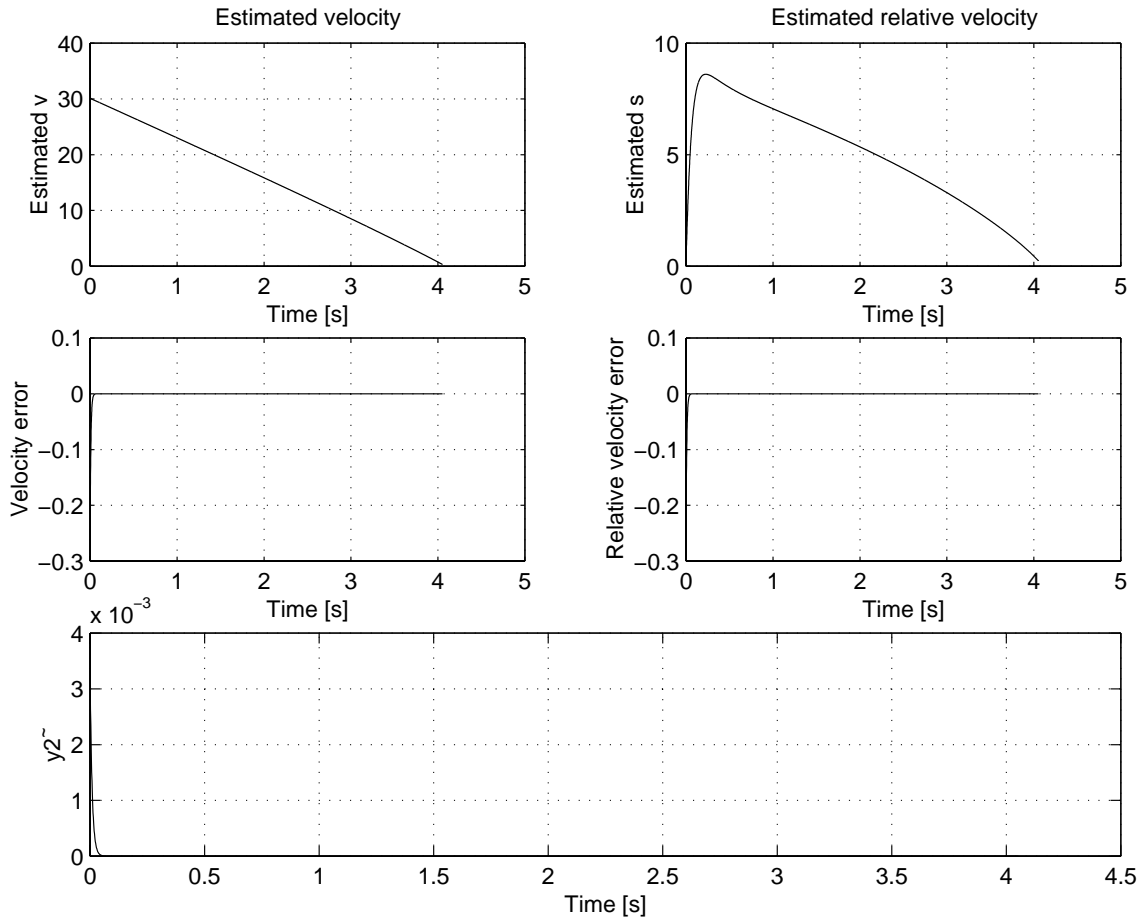
Figure 5.18: Estimated velocity ($\hat{v}$), relative velocity ($\hat{v}_r$) and output error ($\tilde{y}_2$).

dynamic friction model, which was applied to the tire/road interaction. We first explored designs for controlling brake pressure by assuming that the vehicle velocity and the internal state were measurable. We used the static maximum slip as an approximation for the maximum deceleration when the vehicle has fairly high longitudinal speed. The simulation results showed that the vehicle can be stopped as quickly as possible by application of this controller.

In the second part of this chapter, we relaxed the assumption of the availability of the friction internal state and the vehicle velocity and assumed only the angular velocity of the wheel is available. The braking pressure controller was determined based on the estimation of system state variables and the unknown friction parameter. The simulation results showed that the vehicle can be stopped quickly with near maximum deceleration by applying this controller. The asymptotic convergence of the estimated states and parameter estimates has been proven using the Lyapunov function approach and a LMI technique. Moreover, it was also shown that the friction properties can be estimated and near maximum deceleration achieved, in spite of the slow convergence rate of the vehicle velocity and wheel relative velocity error estimates. Fortunately, both automated highway systems (AHS) and manual traffic applications rely on various other measurements to guarantee safety; (e.g. radar sensors and human perception). Thus, the control system does not need an accurate estimate of the vehicle velocity. Simulation tests conducted so far suggest that the proposed control scheme, based
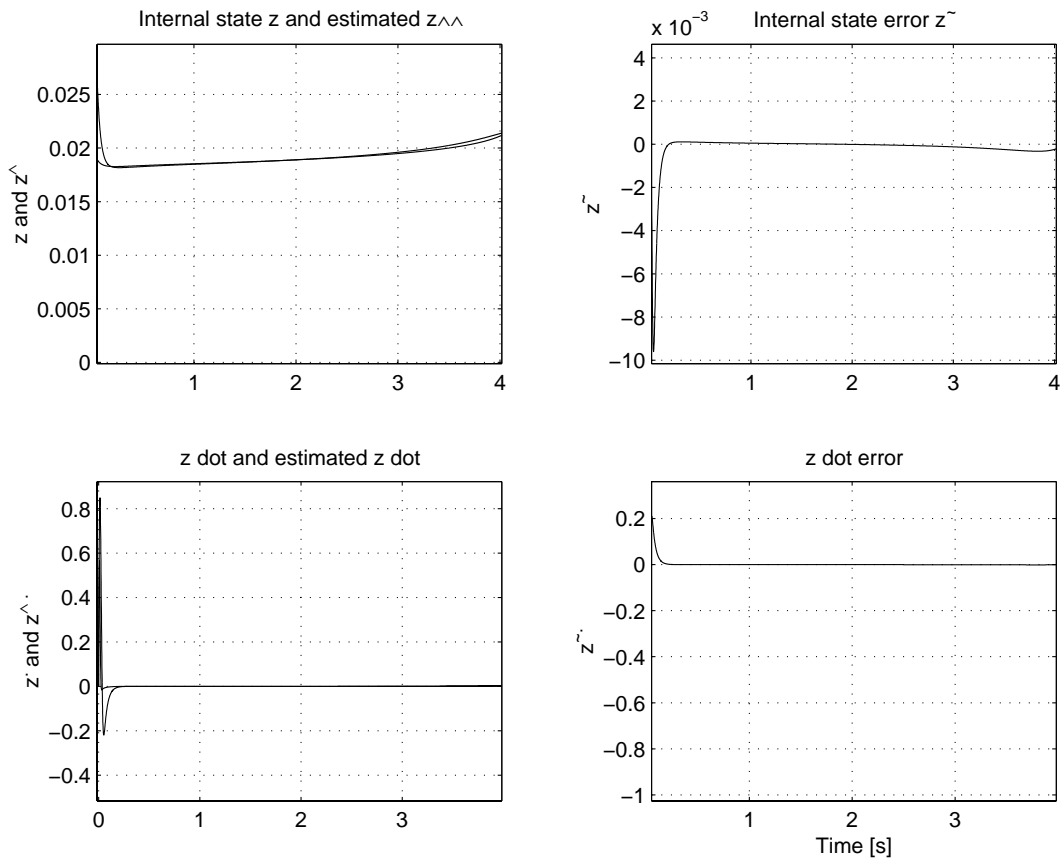
Figure 5.19: Estimated internal state $(\hat{z})$ and its derivative $(\dot{\hat{z}})$

on an observed dynamic friction model, achieves near maximum deceleration in a faster and more stable manner than previous static approaches.

In the last part of this chapter, we considered additional longitudinal acceleration measurement as well as the measurement of wheel angular velocity, in order to overcome the slow convergence rate problem. The braking pressure controller was determined based on the estimation of system state variables and the unknown friction parameter. The asymptotic convergence of the estimated states and parameter estimates has been proven under a proper selection of adaptation gains and initial estimation errors. Moreover, a property of underestimation of the maximum friction coefficient can also be achieved by a proper choice of the adaptation gains and initial conditions of the estimated parameters. The simulation results show that the vehicle can be stopped quickly with near maximum deceleration by applying this controller.
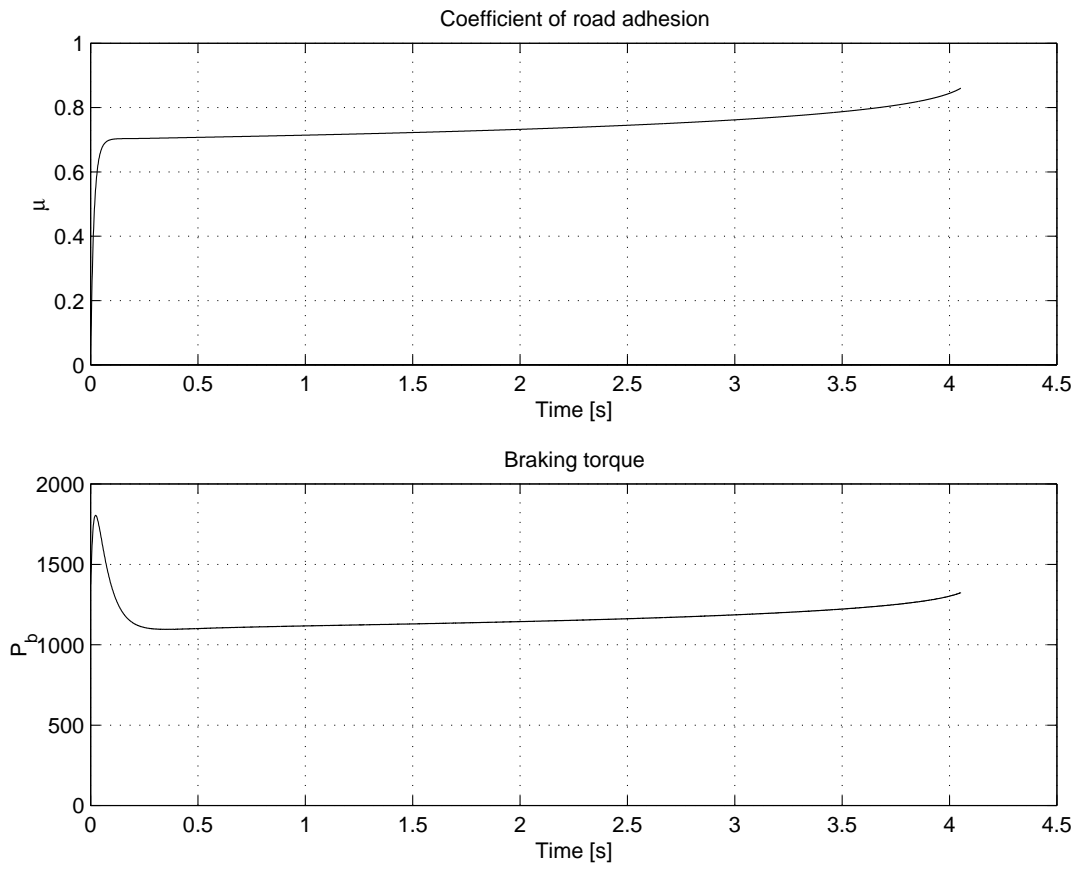
Figure 5.20: Friction coefficient μ and braking pressure $P_b(KPa)$
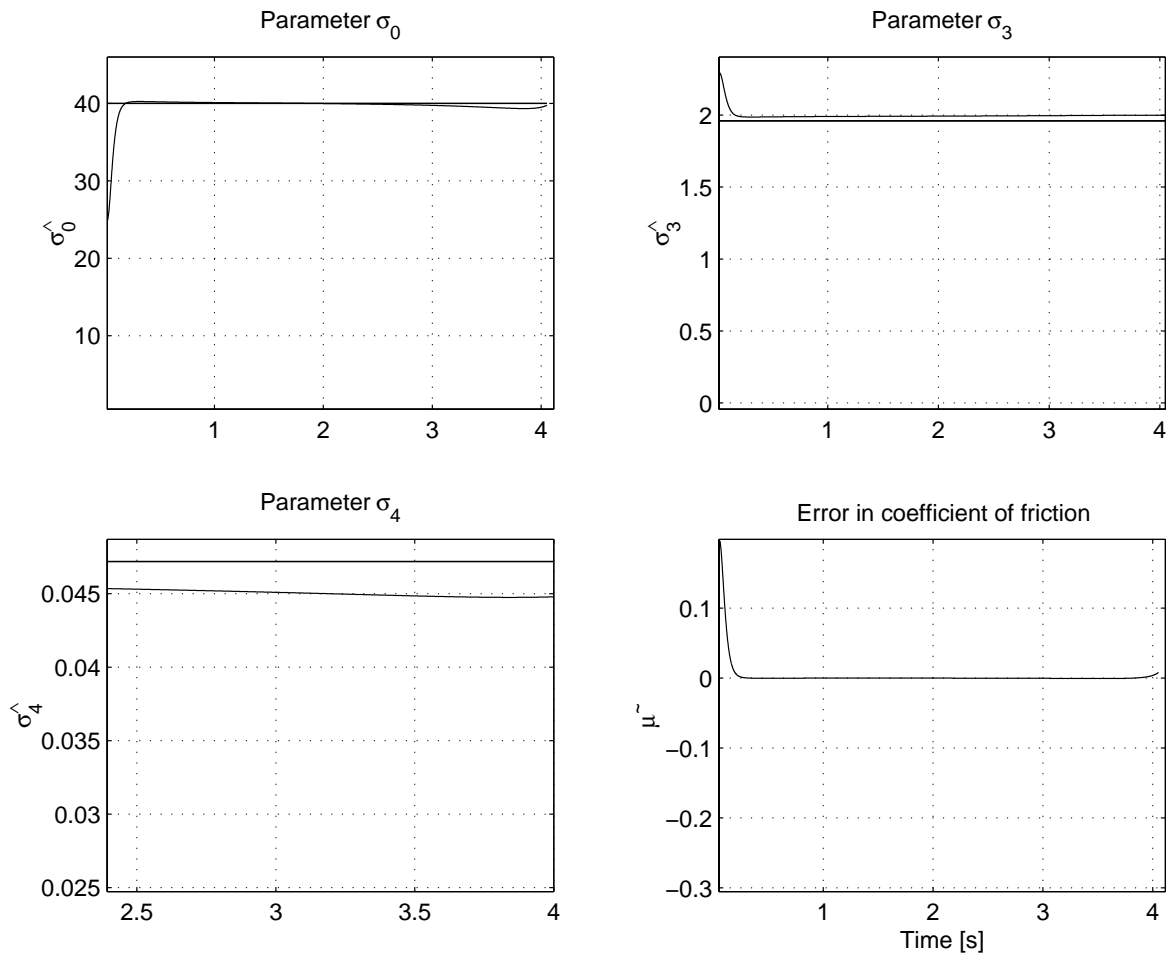
Figure 5.21: Estimated parameters

Bibliography

A., A.: 1983, Stabilization of a class of plants with possible loss of outputs or actuator failures, *IEEE Transactions on Automatic Control* **28**, 231–233.

Agogino, A., Goebel, K. and Alag, S.: 1997, Intelligent Sensor Validation and Sensor Fusion for Vehicle Guidance Using Probabilistic and Fuzzy Methods, *PATH Research Report UCB-ITS-PRR-97-31*, Institute of Transportation Studies, University of California at Berkeley.

Alvarez, L.: 1996, *Automated Highway Systems: Safe Platooning and Traffic Flow Control*, PhD dissertation, Department of Mechanical Engineering, University of California at Berkeley.

Armstrong-Hélouvry, B., Dupont, P. and Canudas de Wit, C.: 1994, A Survey of Models, Analysis Tools and Compensation Methods for the Control of Machines with Friction, *Automatica* **30**(7), 1083–1138.

Bakker, E., Nyborg, L. and Pacejka, H. B.: 1987, Tyre Modeling for Use in Vehicle Dynamics Studies, *SAE Transactions* (870421), 190–204.

Bakker, E., Pacejka, H. B. and Lidner, L.: 1989, A Tire Model with an Application in Vehicle Dynamics Studies, *SAE Transactions* (890087), 83–95.

Bareket, Z. and Fancher, P.: 1989, Representation of Truck Properties in Braking and Handling Studies: The Influence of Pavement and Tire Conditions on Frictional Characteristics, *Research Report UMTRI-89-33*, University of Michigan.

Basseville, M. and Nikiforov, I.: 1993, *Detection of Abrupt Changes*, Prentice Hall.

Beard, R. V.: 1971, *Failure accomodation in linear systems through self-reorganization*, PhD dissertation, Massachusetts Institute of Technology, Cambridge, MA.

Bliman, P.: 1992, Mathematical Study of the Dahl's Friction Model, *European Journal of Mechanics, A/Solids* **11**(6), 835–848.

Bliman, P., Bonald, T. and Sorine, M.: 1995, Hysteresis Operators and Tyre Friction Models: Application to Vehicle Dynamic Simulation, *Proceedings of ICIAM'95*, Hamburg, Germany.

Bliman, P. and Sorine, M.: 1991, Friction Modelling by Hysteresis Operators: Application to Dahl, Stricktion, and Stribeck Effects, *Proceedings of Conference on Models of Hysteresis*, Trento, Italy.

Bliman, P. and Sorine, M.: 1995, Easy-to-use Realistic Dry Friction Models for Automatic Control, *Proceedings of the 3rd European Control Conference*, Rome, Italy, pp. 3788–3794.

Bow, S.-T.: 1992, *Pattern Recognition and Image Preprocessing*, Marcel Dekker, Inc.

Brogan, W.: 1991, *Modern Control Theory*, Prentice Hall.

Burckhardt, M.: 1993, *Fahrwerktechnik: Radschlupf-Regelsysteme*, Vogel-Verlag, Würzburg, Germany.

Canudas de Wit, C. and Horowitz, R.: 1999, Observers for Tire/Road Contact Friction using only wheel angular velocity information, *The 38th IEEE Conference of Decision and Control*, Phoenix, AZ.

Canudas de Wit, C. and Lischinsky, P.: 1997, Adaptive Friction Compensation with Partially Known Dynamic Friction Model, *International Journal of Adaptive Control and Signal Processing* **11**(1), 65–85.

Canudas de Wit, C., Olsson, H., Åström, K. and Lischinsky, P.: 1995, A New Model for Control of Systems with Friction, *IEEE Transactions on Automatic Control* **40**(3), 419–425.

Canudas de Wit, C. and Tsiotras, P.: 1999, Dynamic Tire Friction Models for Vehicle Traction Control, *The 38th IEEE Conference of Decision and Control*, Phoenix, AZ.

Canudas de Wit, C., Tsiotras, P., Claeys, X., Yi, J. and Horowitz, R.: 2001, Tire/Road Friction Modeling, Estimation and Optimal Braking Control, *NACO Workshop on Advanced Automotive Control*, Lund, Sweden.

Carbaugh, J., Alvarez, L., Chen, P. Y. and Horowitz, R.: 1997, SmartPATH Regulation Layer Implementation: A User's Guide, *PATH Research Reports UCB-ITS-PRR-97-48*, Institute of Transportation Studies, University of California at Berkeley.

Chen, P. Y., Alvarez, L. and Horowitz, R.: 1997, Trajectory Design and Implementation of Longitudinal Maneuvers on Automated and Transition Lanes, *PATH Research Reports UCB-ITS-PRR-97-49*, Institute of Transportation Studies, University of California at Berkeley.

Cho, Y. M. and Rajamani, R.: 1997, A Systematic Approach to Adaptive Observer Synthesis for Nonlinear Systems, *IEEE Transactions on Automatic Control* **42**(4), 534–537.

Chung, R. K. D. W., Malladi, D., Chen, R., Speyer, J. L. and Mingori, D.: 1996, Fault Detection and Identification with Application to Advanced Vehicle Control Systems: Final Report, *PATH Research Report UCB-ITS-PRR-96-25*, Institute of Transportation Studies, University of California at Berkeley.

Chung, R. K. D. W., Malladi, D., Chen, R., Speyer, J. L. and Mingori, D.: 1997, Fault Detection and Identification with Application to Advanced Vehicle Control Systems, *PATH Research Report UCB-ITS-PRR-97-51*, Institute of Transportation Studies, University of California at Berkeley.

Claeys, X., Yi, J., Horowitz, R., Canudas de Wit, C. and Richard, L.: 2001a, A New 3D Tire/road Friction Model for Vehicle Simulation, *Proceedings of 2001 ASME International Mechanical Engineering Congress and Exposition*, Vol. II, New York, NY.

Clark, S.: 1981, *Mechanics of Pneumatic Tires*, Department of Transportation, Washington, DC. DOT HS-805 952.

Dahl, P.: 1976, Solid Friction Damping of Mechanical Vibrations, *AIAA Journal* **14**(12), 1675–1682.

Deur, J.: 2001, Modeling and Analysis of Longitudinal Tire Dynamics Based on the LuGre Friction Model, *The Proceedings of the IFAC Conference on Advances in Automotive Control*, Kalsruhe, Germany, pp. 101–106.

Deur, J., Asgan, J. and Hrovat, D.: 2001, A Dynamic Tire Friction Model for Combined Longitudinal and Lateral Motion, *Proceedings of 2001 ASME International Mechanical Engineering Congress and Exposition*, New York, NY.

Dixon, J.: 1991, *Tyres, suspension, and handling*, Cambridge England ; New York : Cambridge University Press, Cambridge Engineering Series.

Drakunov, S., Özgüner, Ü., Dix, P. and Ashrafi, B.: 1995, ABS Control Using Optimum Search via Sliding Modes, *IEEE Transactions on Control Systems Technology* **3**(1), 79–85.

E., E.: 1983, Simultaneous stabilization with fixed closed loop characteristc polynomial, *IEEE Transactions on Automatic Control* **28**, 103–104.

El Ghaoui, L., Nikoukhah, R. and Delebecque, F.: 1995, LMITOOL: a Package for LMI Optimization, *The $34th$ IEEE Conference of Decision and Control*, New Orleans, LA.

et al., B. V.: 1993, Simultaneous stabilization of three or more plants: conditions on real axis do not suffice, *SIAM Journal of Control and Optimization* **??**, ??

et al, G.: 1996, Study of design directions for vehicle lateral control, *Proc. of the 36th Conference on Decision and Control, San Diego*, pp. 1732–1737.

et al, P.: 1997, A general framework for automatic steering control: Sytem analysis, *Proc. of the American Control Conference*, pp. 1598–1602.

et al, S.: 2000, Fault tolerant lateral control of automated vehicles based on simultaneous stabilization, *Proc. of 1st IFAC Conference on Mechatronics*, pp. 899–904.

et al, S. S.: 1978, Steering controller design for automated guideway transit vehicles, *ASME Journal of Dynamic Systems, Measurements and Control* **100(1)**, 1–8.

Fancher, P. and Bareket, Z.: 1991, Including roadway and tread factors in a semi-empirical model of truck tyres, *Supplement to Vehicle System Dynamics: Tyre Model For Vehicle Analysis*, Vol. 21.

Fancher, P., Bernard, J., Clover, C. and Winkler, C.: 1997, Representing truck tire characteristics in simulations of braking and braking in turn maneuvers, *Supplement to Vehicle System Dynamics: Tyre Model For Vehicle Analysis*, Vol. 27.

Frank, P.: 1990, Fault diagnosis in dynamic systems using analytical and knowledge-based redundancy, *Automatica* **26**(3), 459–474.

Garg, V.: 1995, *Fault Detection in Nonlinear Systems*, PhD dissertation, Department of Mechanical Engineering, University of California at Berkeley.

Gen: 1997, *H-Platform Service Manual*. Part No. 3295.

Gerdes, J. C.: 1996, *Decoupled Design of Robust Controllers for Nonlinear Systems: As Motivated by and Applied to Coordinated Throttle and Brake Control for Automated Highways*, PhD dissertation, Department of Mechanical Engineering, University of California, Berkeley, CA.

Gerdes, J. C. and Hedrick, K.: 1995, Brake System Requirements for Platooning on an Automated Highway, *The American Control Conference*, Seattle, Washington, pp. 165–169.

Gertler, J.: 1988, Survey of model-based failure detection and isolation in complex plants, *IEEE Control Systems Magazine* pp. 3–11.

Gim, G. and Nikravesh, P.: 1990, An analytical model of pneumatic tyres for vehicle dynamic simulations. Part I: Pure slips, *International Journal of Vehicle Design* **11**(6), 589–618.

Godbole, D., Lygeros, J., Singh, E., Deshpande, A. and Lindsey, A.: 2000, Communication Protocols for a Fault-Tolerant Automated Highway System, *IEEE Transactions on Control Systems Technology* **8**(5), 787–800.

Gustafsson, F.: 1997, Slip-based Tire-Road Friction Estimation, *Automatica* **33**(6), 1087–1099.

Harned, J., Johnston, L. and Scharpf, G.: 1969, Measurement of Tire Brake Force Characteristics as Related to Wheel Slip (Antilock) Control System Design, *SAE Transactions* **78**(690214), 909–25.

Hirschorn, R. and Miller, G.: 1999, Control of Nonlinear Systems with Friction, *IEEE Transactions on Control Systems Technology* **7**(5), 588–595.

Horne, W. and Buhlmann, F.: 1983, A method for rating the skid resistance of micro/macrotexture characteristics of wet pavements, *Frictional Interaction of Tire and Pavement, American Society for Testing and Materials*.

Howell, A.: 2002, Nonlinear observer design via convex optimization. Submitted to ACC 2002 (copy attached to report).

Howell, A. and Hedrick, J.: 1999, Multiple fault diagnosis as applied to automated vehicle control, *Proc. of ASME IMECHE*, Vol. 67, DSC, pp. 615–622.

J., A.: 1985, *Uncertainty and control*, Lecture Notes in Control and Information Sciences , *Springer Verlag*, Berlin.

Jansen, S., Gootjes, L., Pauwelussen, J. and Schröder, C.: 2000, Full vehicle abs braking using the swift rigid ring tyre model, *1st Conference on Mechatronic Systems*, Darmstadt, Germany, pp. 115–120.

Khalil, H.: 1996, *Nonlinear Systems*, 2nd edn, Prentice Hall, NJ.

Kiencke, U.: 1993, Realtime Estimation of Adhesion Characteristic Between Tyres and Road, *Proceedings of the IFAC World Congress*, Vol. 1.

Kiencke, U. and Daiss, A.: 1994, Estimation of Tyre Friction for Enhaced ABS-Systems, *Proceedings of the AVEG'94*.

Lee, H. and Tomizuka, M.: 1995, Adaptive Traction Control, *PATH Research Report UCB-ITS-PRR-95-32*, Institute of Transportation Studies, University of California at Berkeley.

Lenke, L. and Graul, R.: 1986, Development of runway rubber removal specifications using friction measurement and surface texture for control, *The Tire Pavement Interface, ASTM STP 929, M.G. Pottinger ans T.J Yagger , Eds, American Society of Testing and Materials*, pp. 72–88.

Lippmann, S. and Oblizajek, K.: 1974, The distributions of stress between the tread and the road for freely rolling tires, *SAE Transactions* (740072).

Lygeros, J., Godbole, D. and Broucke, M.: 2000, A Fault Tolerant Control Architecture for Automated Highway Systems, *IEEE Transactions on Control Systems Technology* **8**(2), 205–219.

M., V. and N., V.: 1982, Algebraic design techniques for reliable stabilization, *IEEE Transactions on Automatic Control* **27**, 1085–1095.

Maciuca, D.: 1997, *Nonlinear Robust and Adaptive Control with Application to Brake Control for Automated Highway Systems*, PhD dissertation, Department of Mechanical Engineering, University of California, Berkeley, CA.

Mastinu, G. and Fainello, M.: 1992, Study of pneumatic tyre behavior on dry and rigid road by finite element method, *Vehicle System Dynamics* **21**.

Olsson, H.: 1996, *Control Systems with Friction*, PhD dissertation, Department of Automatic Control, Lund Institute of Technology, Lund, Sweden.

org., R. I.: n.d., Supervision,fault detection and diagnosis of technical systems, Notes from the Tutorial workshop of the 1997 American Control Conference.

P., H.: 1997, *Robustness and Performance in the Lateral Control of Vehicles in Automated Highway Systems*, PhD dissertation, University of California, Berkeley.

Pal, C., Hagiwara, I., Morishita, S. and Inoue, H.: 1994, Application of Neural Networks in Real Time Identification of Dynamic Structural Response and Prediction of Road Friction Coefficient μ from Steady State Automobile Response, *The International Symposium on Advanced Vehicle Control*, Japan, pp. 527–532.

Pasterkamp, W. and Pacejka, H.: 1997, The Tyre as a Sensor to Estimate Friction, *Vehicle System Dynamics Supplement* **27**, 409–422.

Patwardhan, S.: 1994, *Fault Detection and Tolerant Control for Lateral Guidance of Vehicles in Automated Highways*, PhD dissertation, Department of Mechanical Engineering, University of California, Berkeley, California.

R., S. and J., M.: 1982, Fractional representation, algebraic geometry and the simultaneous staibilization problem, *IEEE Transactions on Automatic Control* **27**, 895–903.

Rajamani, R., Hedrick, K. and Howell, A.: 1997, A Completed Fault Diagnostic System for Longitudinal Control for Automated Vehicles, *Proceedings of ASME Dynamic Systems and Control Division, ASME International Mechanical Engineering Congress and Exposition*, Dullas, TX.

Rajamani, R., Howell, A., Chen, C., Hedrick, J. and Tomizuka, M.: 2001, A Complete Fault Diagnostic System for the Longitudinal Control of Automated Vehicles, *IEEE Transactions on Control Systems Technology* **9**(4), 553–564.

Ray, L. R.: 1997, Nonlinear Tire Force Estimation and Road Friction Identification: Simulation and Experiments, *Automatica* **33**(10), 1819–1833.

Ross, T.: 1995, *Fuzzy logic with engineering applications*, McGraw-Hill.

Sakai, H.: 1982, Theoretical and experimental studies on the dynamic properties of tires, Part 4: Investigations of the influences of running conditions by calculation and experiment, *International Journal of Vehicle Design* **3**(3), 331–375.

Schuring, D. J.: 1976, Tire Parameter Determination, *DOT HS-802 089*, Calspan Corporation.

Slotine, J.-J. E. and Li, W.: 1991, *Applied Nonlinear Control*, Prentice-Hall, USA.

Sorine, M. and Szymanski, J.: 2000, A New All-Vehicle-Speed Dynamic Tire Model, *Proceedings of IFAC Symposium on Control in Transportation Systems*, Braunschweig, Germany.

Staff: 1998, Avcs vehicle-follower longitudinal control technologies: Final report, *Technical report*, California PATH. Research Agreement 65V313-001.

Swaroop, D.: 1994, *String Stability of Interconnected Systems: An Application to Platooning in Automated Highway Systems*, PhD dissertation, UC Berkeley.

Swaroop, D., Gerdes, J. and J.K., H.: 1996, Dynamic surface control of nonlinear systems, *35th IEEE Conference on Decision and Control*, IEEE, Kobe, Japan.

Tan, H. and Tomizuka, M.: 1990, An Adaptive Sliding Mode Vehicle Traction Controller Design, *The American Control Conference*, San Diego, California, pp. 1156–61.

Tanner, J.: 1996, Computational methods for friction contact with application to the space shuttle orbiter nose-gear tire-development of frictional contact algorithm, *Technical report*, NASA. TP-3574.

V., B.: 1991, A counterexample to a simultaneous stabilization condition for systems with identical unstable poles and zeros, *Systems and Control Letters* **17**, 339–341.

V, B. and M., G.: 1993, The simultaneous stabilizability question of three linear systems is rationally undecidable, *Journal of Math. in Control, Signals and Systems* **??**, ??

Varaiya, P.: 1993, Smart Cars on Smart Roads: Problems of Control, *IEEE Transactions on Automatic Control* **38**(2), 195–207.

Willsky, A. S.: 1976, A survey of design method for failure detection systems, *Automatica* **12**, 601–611.

Wong, J. Y.: 1993, *Theory of Ground Vehicles*, 2nd edn, John Wiley & Sons, New York, NY.

Yi, J., Alvarez, L., Horowitz, R. and Canudas de Wit, C.: 2000, Adaptive Emergency Braking Control in Automated Highway System Using Dynamic Tire/Road Friction Model, *The* 39*th IEEE Conference of Decision and Control*, Sydney, Australia, pp. 456–461.

Yi, J., Howell, A., Horowitz, R., Hedrick, K. and Alvarez, L.: 2001, Fault Detection and Handling for Longitudinal Control of Automated Highway Systems (AHS), *PATH Research Report UCB-ITS-PRR-2001-21*, Institute of Transportation Studies, University of California at Berkeley.

Yi, K., Hedrick, K. and Lee, S.-C.: 1999, Estimation of Tire-Road Friction Using Observer Based Identifiers, *Vehicle System Dynamics* **31**(2), 233–261.

Yi, K. and Jeong, T.: 1998, Observer Based Estimation of Tire-road Friction for Collision Warning Algorithm Adaptation, *JSME International Journal* **41**(1), 116–124.